Structure-Property Relationships in Aluminum-Copper alloys using Transmission X-Ray Microscopy (TXM) and Micromechanical Testing

by

Chandrashekara Shashank Kaira

A Dissertation Presented in Partial Fulfillment
of the Requirements for the Degree
Doctor of Philosophy

Approved October 2017 by the
Graduate Supervisory Committee:

Nikhilesh Chawla, Chair
Kiran Solanki
Yang Jiao
Vincent De Andrade

ARIZONA STATE UNIVERSITY

December 2017

ABSTRACT

Aluminum alloys are ubiquitously used in almost all structural applications due to their high strength-to-weight ratio. Their superior mechanical performance can be attributed to complex dispersions of nanoscale intermetallic particles that precipitate out from the alloy's solid solution and offer resistance to deformation. Although they have been extensively investigated in the last century, the traditional approaches employed in the past haven't rendered an authoritative microstructural understanding in such materials. The effect of the precipitates' inherent complex morphology and their three-dimensional (3D) spatial distribution on evolution and deformation behavior have often been precluded. In this study, for the first time, synchrotron-based hard X-ray nano-tomography has been implemented in Al-Cu alloys to measure growth kinetics of different nanoscale phases in 3D and reveal mechanistic insights behind some of the observed novel phase transformation reactions occurring at high temperatures. The experimental results were reconciled with coarsening models from the LSW theory to an unprecedented extent, thereby establishing a new paradigm for thermodynamic analysis of precipitate assemblies. By using a unique correlative approach, a non-destructive means of estimating precipitation-strengthening in such alloys has been introduced. Limitations of using existing mechanical strengthening models in such alloys have been discussed and a means to quantify individual contributions from different strengthening mechanisms has been established.

The current rapid pace of technological progress necessitates the demand for more resilient and high-performance alloys. To achieve this, a thorough understanding of the

relationships between material properties and its structure is indispensable. To establish this correlation and achieve desired properties from structural alloys, microstructural response to mechanical stimuli needs to be understood in three-dimensions (3D). To that effect, *in situ* tests were conducted at the synchrotron (Advanced Photon Source) using Transmission X-Ray Microscopy as well as in a scanning electron microscope (SEM) to study real-time damage evolution in such alloys. Findings of precipitate size-dependent transition in deformation behavior from these tests have inspired a novel resilient aluminum alloy design.

DEDICATION

To my parents and sister, for always believing in me and inspiring me to dream big.

ACKNOWLEDGMENTS

I'd like to primarily acknowledge and thank my advisor, Professor Nikhilesh Chawla, for continually guiding, supporting and motivating me throughout the course of my doctoral degree at Arizona State University. I'm very grateful to him for providing me with ample opportunities to explore and delve into various frontiers of materials science and for molding me into a successful researcher.

I'm very thankful to my committee members, Dr. Kiran Solanki, Dr. Jang Jiao, and Dr. Vincent De Andrade, for taking their time to evaluate my doctoral research. I'd also like to specially thank Dr. Vincent De Andrade and Dr. Francesco De Carlo from the Advanced Photon Source at Argonne National Laboratory for their support and for the use of X-ray Synchrotron facilities, without which this work would not have been possible. I'd also like to acknowledge financial support from the Army Research Office (ARO, Contract No. W911NF1410550, Dr. Michael Bakas and Dr. David Stepp, Program Managers) to conduct this research. Use of resources at Beamline 32-ID-C of the Advanced Photon Source, a U.S. Department of Energy (DOE) Office of Science User Facility operated for the DOE Office of Science by Argonne National Laboratory under Contract No. DE-AC02-06CH11357, is also acknowledged. I also gratefully acknowledge the use of facilities within the Center for 4D Materials Science and the Leroy Eyring Center for Solid State Science at Arizona State University. I'd like to also acknowledge all my colleagues in Professor Chawla's research group for their help and collaboration. A special thanks to Dr. Sudhanshu Shekhar Singh and Dr. Carl Mayer, for their guidance and for all the intellectual and fun conversations.

Most importantly, I would like to extend my deepest gratitude to my family and numerous friends for their unconditional love, faith and support.

TABLE OF CONTENTS

Page

CHAPTER Page

CHAPTER Page

LIST OF FIGURES

Figure Page

Figure Page

Figure Page

Figure Page

Figure Page

Figure Page

Figure Page

Figure Page

CHAPTER 1

INTRODUCTION

For the past 75 years, aluminum alloys have served as the material of choice in most aerospace (nearly 65% in commercial aircrafts), automotive and structural applications due to their lightweight and high strength (Cantor, Assender, and Grant 2001). Their significant abundance in the earth's crust and ease of extraction makes them economically quite attractive. The ability to tailor specific properties by alloying aluminum accordingly has contributed to its immense popularity. Although quite weak in its pure form, aluminum's strength can be increased multifold upon alloying with elements such as copper, magnesium, zinc, etc. It wasn't until the mid-20th century that the exact scientific mechanisms behind strengthening in these alloys were discovered. Their superior mechanical performance can be attributed to the complex distribution of second phase intermetallic particles that precipitate out from the alloy's solid solution. A fundamental understanding of structure-property relationships in these alloys is key to designing and tailoring microstructures for high performance, as such materials are subjected to extreme working conditions, due to which reliability and safety have become major concerns. To be able to establish this correlation and achieve desired properties from these structural alloys, it is essential to have a thorough understanding of their microstructure through accurate characterization.

Traditionally, several two-dimensional (2D) characterization techniques, such as optical microscopy, scanning electron microscopy (SEM), and transmission electron microscopy (TEM), have found widespread use in the physical and biological sciences. However, some of the drawbacks associated with these techniques are, but not limited to, cumbersome sample preparation, limited field of view, and their destructive nature. The common shortcoming with these techniques, though, is the 2D nature of characterization, which can misrepresent the actual size and morphology of the particles being investigated in the microstructure. These techniques have become inadequate, as they only provide limited information on complex three-dimensional problems, making it imperative to visualize and quantify the microstructure in three dimensions. Precipitates in aluminum alloys can exist in a variety of sizes and complex shapes, further highlighting the crucial need to understand their intricate three-dimensional (3D) spatial distribution. Although techniques like atom probe tomography (Miller and Kenik 2004) and electron tomography (Midgley and Dunin-Borkowski 2009) also allow 3D characterization with ultra-high spatial resolution, they offer a very limited field of view and statistically insufficient results.

Synchrotron-based X-ray computed tomography (CT) is an alternative powerful characterization tool that has a unique potential due to its nondestructive nature and in situ imaging capabilities (Hruby et al. 2014; Singh et al. 2014). In conventional X-ray tomography techniques, the spatial resolution is limited by the pixel size of the charge-coupled device (CCD), to around 1 μm (Yazzie et al. 2012). However, with the advancement in nanoscale lithography techniques, it has been possible to fabricate

diffractive optics (Fresnel zone plates) that are capable of manipulating and focusing X-rays [Transmission X-ray Microscopy (TXM)] (Chandrashekara S Kaira et al. 2016; Schroer 2006) and hence, allowing features on the nanoscale to be resolved, even in relatively dense materials. Although soft X-ray transmission microscopy has allowed investigation of several biological specimens at spatial resolutions better than 15 nm (Chao et al. 2005), its utility is limited by its short depth of penetration and hence, cannot be used for 3D characterization in metallic specimens. For this reason, hard X-rays are very effective due to their penetrating potential. But, achieving high spatial resolutions in the hard X-ray regime can be challenging due to a drop in the efficiency of zone plates and thus, high aspect ratio zone plates are required to maintain the diffraction efficiency and provide adequate signal (Gorelick et al. 2011). These challenges have been overcome by using the new in-house Transmission X-ray Microscope (TXM) installed at sector 32-ID-C of the Advanced Photon Source (APS). It is one of the highest resolution synchrotron-based hard X-ray microscopes that is capable of nanotomography and imaging at unprecedented spatial resolutions of 20 nm and 60 nm using high aspect ratio zone plates (De Andrade et al. 2016). The research work in this dissertation describes implementation of this technique in conjunction with several other complementary characterization techniques to probe 4D nanoscale microstructural evolution, reveal novel transformation mechanisms and validate fundamental thermodynamic models. Non-destructive means of estimating 3D crystallographic orientation of the different precipitate phases has been established. It has also been possible to experimentally estimate the Orowan stress using

this approach, which is quite crucial as it allows, for the first time, validation of the Orowan model as well as possibly, several other dislocation-particle interaction models.

Bulk alloys consist of a heterogeneous microstructure, implying that different regions of the material may have varying particle size, spacing, and even crystal structures. Most macro-mechanical tests give an "average" response from all the microstructural features present and hence, there is an increasing need to be able to isolate, quantify and understand the effect of each individual microstructural component at very small length scales. Micropillar compression is one of the best suited techniques to do this. Although nanoindentation has also been used frequently to probe the micromechanical behavior, the complex stress state involved makes it difficult to unambiguously interpret the results. This technique has been widely used to obtain the stress-strain response of a number of FCC (Greer, Oliver, and Nix 2005; Nix et al. 2007), BCC (A. S. Schneider et al. 2009; Uchic, Shade, and Dimiduk 2009), HCP materials (Byer et al. 2010) and has also revealed the presence of a size effect at smaller length-scales (Kunz, Pathak, and Greer 2011; Lee and Nix 2012). **C**ombining this miniaturized mechanical testing technique with 3D characterization will not only enable validation of various dislocation-precipitate interaction models, but would also allow us to obtain accurate structure-property relationships. Using appropriate 3D morphological parameters, a model has been proposed in this dissertation to accurately predict and validate the variation in experimentally measured yield stress. This approach also allows estimation of individual contributions from different strengthening mechanisms and reason out the transition in deformation behavior with aging. The latter part of the dissertation focuses on the use of *in situ*

techniques to better understand evolution of real-time deformation in 3D, its impact on mechanical properties and its influence in refining alloy design approaches. The novelty of this research lies in the use of a multi-scale and multi-modal approach to revisit and better understand some of the most fundamental scientific problems in precipitation-strengthened alloy systems.

CHAPTER 2

LITERATURE REVIEW

Extensive research has gone into understanding the structure and evolution behavior of different precipitates that are present in aluminum alloys, since the discovery of age hardening. It wasn't until 1935 that the precipitation phenomenon was experimentally verified using X-ray diffraction analyses (Hornbogen 2001). However, visual confirmation of the presence of these transition phases was only possible after the advent of transmission electron microscopy (Kelly and Nicholson 1963; Thomas and Whelan 1961). Since then, electron microscopy has seen significant advances and in the last decade, aberration-corrected electron microscopy has rendered it possible to probe the atomic structure of these precipitates in great detail (Bourgeois et al. 2011). These TEM analyses have provided several insights into the morphology, interfacial structure, stoichiometry and orientation relationships of these precipitates. However, the TEM specimen's foil geometry limits our field of view in the z-direction and hence, the distribution of precipitates on only a single plane can be visualized. These precipitates are known to exist in a variety of shapes in aluminum alloys and understanding their complex three-dimensional (3D) spatial distribution is key to predicting the alloy's mechanical properties accurately (Figure 1). Several models and theories exist that explain the interaction of dislocations with different kinds of precipitates (S. Y. Hu et al. 2006; Zhu and Starke 1999) but the underlying assumption in most of them, however, is the spherical nature of the particles. An experimentally ratified comprehensive model that accounts for the precipitate's complex

morphology is still lacking. Stereographic corrections have previously been employed to account for overlap and truncation of particles in TEM micrographs (J.F. Nie and Muddle 2008), but their limitations become very apparent with increasing complexity of particle morphology.

Imaging using X-rays on the other hand, has the potential to offer very high spatial resolutions due to their significantly small wavelengths and they also possess an extremely large depth of field (DOF) (Jacobsen et al. 2000; Maire and Withers 2014). But the spatial resolution in conventional X-ray microtomography is limited by that of the charge-coupled device (CCD) (Hruby et al. 2014; Yazzie et al. 2012). Recent advances in the past decade in nanolithography have led to fabrication of sophisticated diffractive optics (Gorelick et al. 2011; Vila-comamala et al. 2011) that are capable of focusing X-rays and hence, magnifying these radiographs (Di Fabrizio et al. 1999; Schroer 2006). This has led to a new generation of X-ray microscopes (XRMs) (Chao et al. 2005; Requena et al. 2009; Schroer 2006) which provide very high spatial and temporal resolutions and allow 3D analyses of large volumes of material at unprecedented length scales.

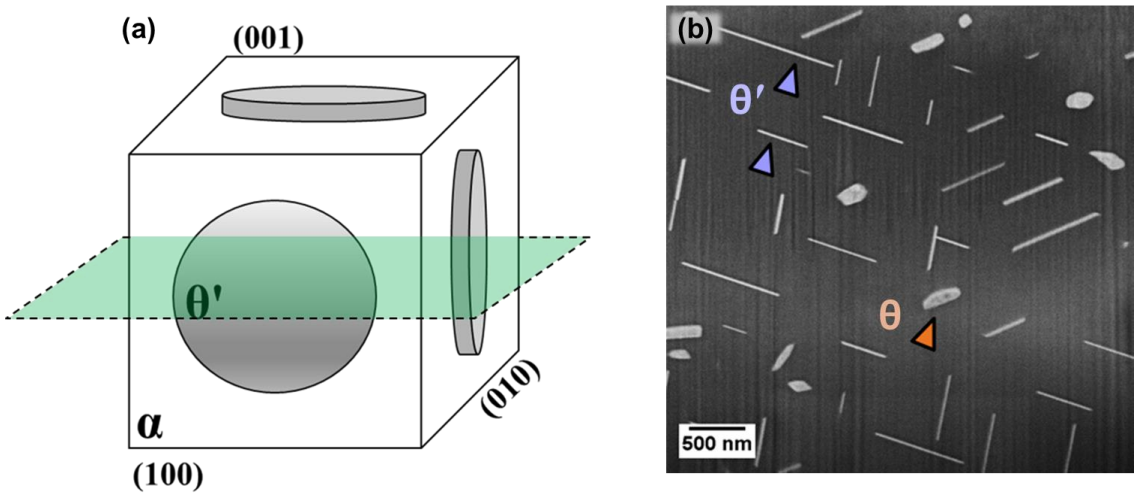

Figure 1: (a) Schematic representing crystallographic distribution of θ′ precipitates in α-Al matrix (b) SEM Image showing the precipitate distribution for an Al-4%Cu alloy (T=350 ^{o}C, t=45 min).

2.1. Precipitate Morphology in Aluminum-Copper alloys

The binary Al-Cu system is a very well-studied precipitation strengthening system and is also representative of the precipitation sequence occurring in the entire family of aluminum alloys. These alloys, upon quenching from the single-phase region of the phase diagram, form a supersaturated solid solution which eventually transitions through precipitation of various metastable intermediate second phase particles, depending on the alloy's composition and temperature, before ultimately forming the equilibrium phase (Hornbogen 2001). Monolayer discs of Cu atoms known as GP-I zones initially form on a specific family of planes of the α-Al matrix and they coarsen into GP-II zones (θ″) which are essentially 3 Al layers sandwiched between 2 monolayers of Cu atoms (Yoshida,

Cockayne, and Whelan 2006). This is the generally accepted definition for the structure of θ″. These then transition to the plate shaped θ′ phase (Al_2Cu) which possesses a body centered tetragonal crystal structure and whose broad faces are coherent with the α-Al matrix ($(001)_{\theta'} \parallel \{001\}_{Al}$) (Laird and Aaronson 1966) as shown in Figure 1. The lattice mismatch between the two phases are minimal along these planes. The θ′ phase subsequently transforms to the relatively more incoherent equilibrium θ phase (Al_2Cu). The crystal structure of the θ phase indicates that significant lattice incompatibility exists between θ and the α-Al matrix. The equilibrium morphology of the precipitates is a result of the interplay between anisotropy of interfacial energy and elastic energy (Vaithyanathan, Wolverton, and Chen 2004). These precipitates are the primary strength imparting components in these alloys and they do so by serving as obstacles to dislocation motion (Figure 2).

The transformation sequence in these alloys can be represented as follows:

Al_{SSS} → GP I Zones → GP II Zones (θ″) → θ′ → θ

A typical hardness profile accompanying the aging process is shown in Figure 2. Transition in deformation behavior from precipitate shearing to Orowan looping has conventionally been invoked to explain this trend. However, this aforementioned transition hasn't been precisely delineated yet and hence, has only been qualitatively understood, due to the inability to capture and visualize these nanoscale deformation processes in real-time.

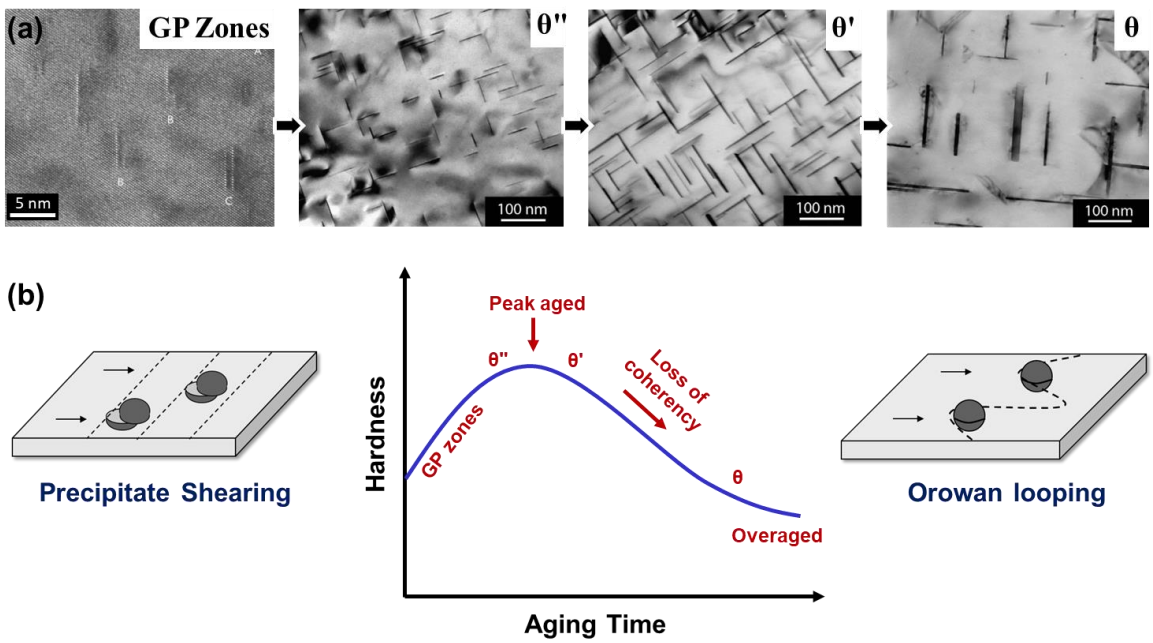

Figure 2: (a) TEM Images showing the different metastable and equilibrium precipitate phases in binary Al-Cu alloys. Reprinted from (Da Costa Teixeira et al. 2008; Karlík et al. 2004) (b) Typical hardness profile trend in such alloys, along with schematics showing the transition in deformation behavior.

2.2. Microstructural Evolution and Growth Kinetics

Several authors have studied the transformation of precipitate phases as well as their coarsening behavior in Al-Cu alloys using transmission electron microscopy. These aspects become increasingly important for high-temperature applications of these alloys. The irregular morphology of the precipitates has also attracted significant attention among researchers to understand the diffusion process(es) controlling the coarsening of individual precipitate phases. It is also a commonly accepted fact that the θ′ phase has broad coherent

faces and semi-coherent rims. Most of these studies have also found evidence of growth ledges on the broad faces of θ′ (Figure 3(b)). These ledges are primarily formed as a result of precipitate impingements and intruder dislocations interacting with their habit planes (Aaronson and Laird 1968; Merle and Merlin 1981). Contrary to popular belief that θ is completely incoherent, Kang and Laird (Kang and Laird 1974) were able to prove that semi-coherent planar interfaces do, in fact, exist in θ precipitates. The structure of these precipitate phases plays an important role in determining their equilibrium morphology as well as their growth kinetics.

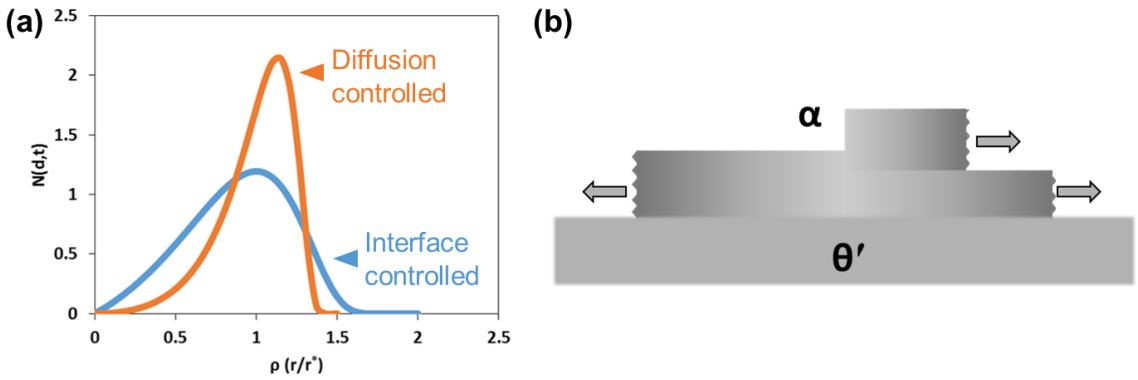

Figure 3: (a) Normalized precipitate size-distribution (PSD) curves from the LSW theory. (b) Schematic showing ledge migration mechanism at a θ′-α interface.

Coarsening has been widely observed in a variety of particle-dispersed systems, where the system strives to attain thermodynamic stability by minimizing the total surface energy of the ensemble. The LSW theory, put forth by Lifshitz and Slyozov (Lifshitz and Slyozov 1961) and Wagner (Wagner 1961), has been able to explain the diffusion-

controlled Ostwald ripening process in great mathematical detail. It predicts the kinetics of the coarsening process (where mean radius of the particles obey a cubic growth law) and the scaled precipitate size distributions (PSDs) to be time invariant (Figure 3(a)). However, application of this theory on metallic systems has been largely debated since its inception and hence, several modifications were put forth that were able to better address the misfit between experiments and theory. It must also be pointed out that most of these studies focused on modifying the LSW theory to account for the apparent deviation, while little attention has been paid to the experimental techniques used to validate the theory. It can be stereographically quite challenging and sometimes nearly impossible to extract accurate particle dimensions from 2D Images, especially with particles having complex morphologies. This can give rise to inaccurate size-distribution curves, which are crucial in discerning the rate-controlling diffusion mechanism during coarsening.

Most studies on Al-Cu alloys have found the experimental size-distribution curves to be broader when compared to their theoretical counterparts and various factors such as overlap of the particle's diffusion fields, coalescence, misfit strains etc. have been attributed to this finding (Boyd and Nicholson 1971; Merle and Fouquet 1981; Voorhees and Glicksman 1984). Boyd and Nicholson (Boyd and Nicholson 1971) studied the coarsening behavior of θ′ and θ″ precipitates in Al-4%Cu alloys. Although, reasonably good agreement with the LSW theory was seen in case of the θ″ precipitates, significant deviation was observed for the θ′ phase and this was attributed to short-circuit diffusion paths created due to particle coalescence. This was also cited as a reason for their observations of anomalously high values of interfacial energy.

Aaronson's estimate of interfacial energy values and equilibrium aspect ratio of θ′ plates (~12) was based on theoretical calculations (Aaronson and Laird 1968) and it was corroborated by experimental measurements. However, it must be pointed out that these measurements using the TEM are associated with an element of uncertainty due to their 2D nature. Vaithyanathan et al. (Vaithyanathan, Wolverton, and Chen 2004) have been able to use first-principles calculations to estimate the interfacial energy of θ′ more accurately as well as compute its equilibrium aspect ratio (~3) by accounting for interfacial energy anisotropy. This value varies significantly from Aaronson's estimate which has been widely implemented in literature.

As a result of its coherent interface, the broad faces of θ′ thicken interfacially by the lateral motion of growth ledges, while the semi-coherent rims of θ′ lengthen at rates higher than that of volume diffusion. Several researchers made this observation and noted the lengthening kinetics to be an order of magnitude (or more) greater than thickening (Aaronson and Laird 1968; Voorhees and Glicksman 1984). Aaronson and Laird deduced that the edges on these ledges have a disordered structure and that their lateral migration is diffusion-controlled, while the thickening of θ′ is interface controlled (Aaronson and Laird 1968). They also noted that lengthening occurs quicker than that allowed by volume diffusion and this was attributed to pipe diffusion of copper via misfit dislocations that surround the θ′ plates.

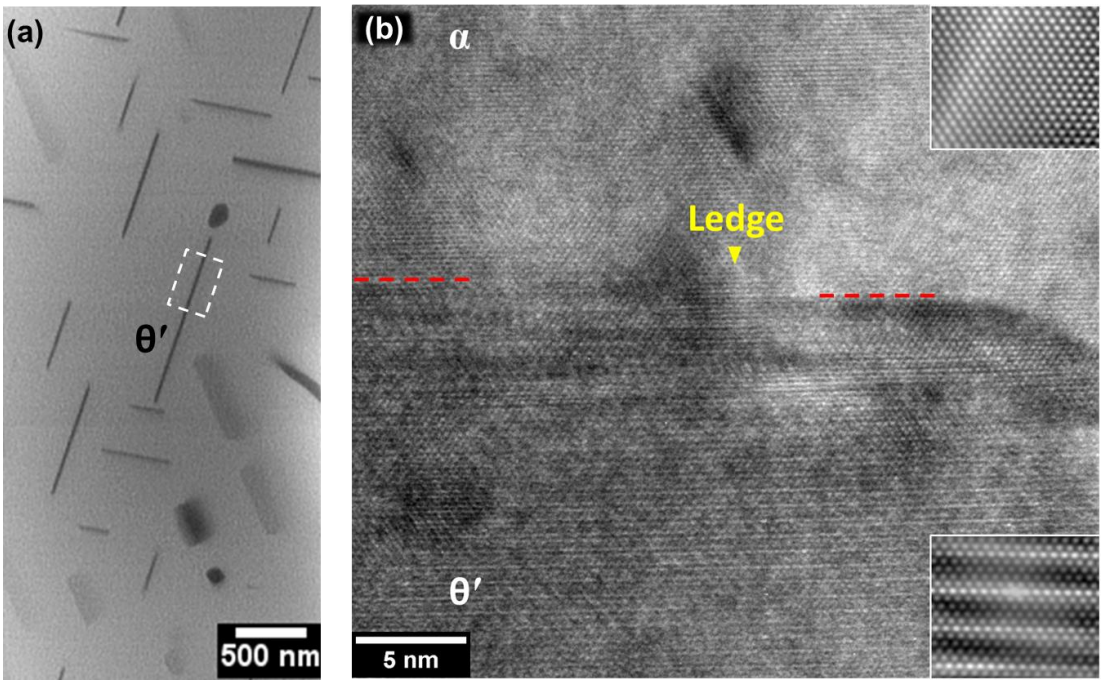

Figure 4: (a) SEM Image showing the precipitate distribution for an Al-4%Cu alloy (T=350 ^{o}C, t=45 min). (b) Ledge at θ′-α interface as seen from HRTEM Image. Insets show fourier-filtered images of the lattice in each phase.

Sankaran and Laird were able to corroborate the fact that lengthening of the θ′ phase occurred much more rapidly than that warranted by volume diffusion (Sankaran and Laird 1974). Their reasoning for the mechanism behind this, however, was the accelerated diffusion caused by the presence of a compressive strain field around the precipitates. As these precipitates (θ′) lose coherency upon aging, relaxation of this strain field causes the lengthening to occur at volume diffusion controlled rates.

Chen and Doherty disputed some of these results and showed that the thickening kinetics need not necessarily be interface controlled due to the presence of ledges (Y. H.

Chen and Doherty 1977). They observed similar growth exponents for both lengthening as well as thickening and reasoned the lower thickening rates with the lack of sufficient ledges. One of the main reasons for this lack of agreement on the controlling diffusion mechanism can be attributed to the difficulties involved in making accurate measurements using transmission electron microscopy. Merle and Fouquet's study on Al-Cu alloys (Merle and Fouquet 1981) revealed the presence of two different processes: size and shape evolution, occurring simultaneously during coarsening of the θ′ phase. They also observed the growth law exponent ($\sim t^{1/5}$) for the mean size of the precipitates to be distinctly different when compared to other theories. Similar to the trend in Boyd and Nicholson's study (Boyd and Nicholson 1971), their scaled PSDs too were significantly broader than those predicted by the LSW theory.

Laird and Aaronson extensively investigated the mechanism of formation of θ and dissolution of θ′ precipitates in an Al-4%Cu alloy (Laird and Aaronson 1966). Pre-aged specimens were further aged on the electron microscope to study the transformation reactions. Their findings can be concisely represented by three reactions which occur simultaneously (shown in Figure 5):

1. Transformation of θ′ completely into θ in two distinguishable ways.

2. Crystallographically distinct θ nucleating at θ′-α boundary and advancing into α.

3. θ′ dissolving in the vicinity of growing θ by countercurrent diffusion of Al and Cu through the α matrix.

They also estimated interdiffusion co-efficients by measuring the kinetics of growth and dissolution of θ and θ′, respectively. These were seen to be significantly higher than conventional diffusion measurements (Mantina et al. 2009), suggesting the enormous influence of surface diffusion on these samples. Snippets of TEM Micrographs from their study captured at different times, depicting a transformation reaction have been shown in Figure 5. It must be noted that the 2D nature of these foils can mask the true morphology of the precipitates involved in the reaction, as a result of which, the mechanism of the transformation reaction can be easily misinterpreted.

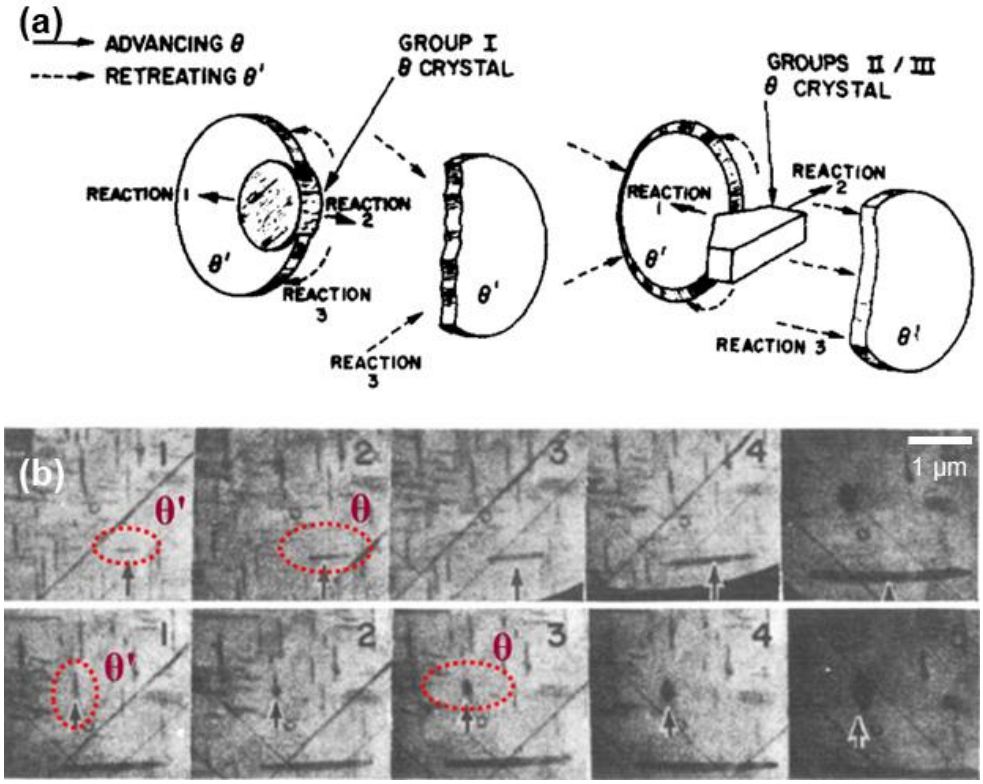

Figure 5: (a) Schematic representing different transformation reactions (θ′ to θ)

(b) Snippets of TEM micrographs showing stills from two transformation reactions.

Reprinted from (Laird and Aaronson 1966).

2.3. Effect of Precipitate Morphology on Mechanical Properties

Nie and Muddle noted the lack of an appropriate version of the Orowan equation (Jian Feng Nie, Muddle, and Polmear 1996; Orowan 1948b) for complex particle morphologies. They were able to account for the plate and rod-like morphology of precipitates in aluminum alloys and eventually, come up with appropriate versions of the Orowan equation for the same. Some of their other work (J. F. Nie and Muddle 2001; J.F. Nie and Muddle 2008) also involved the development of precipitation strengthening models to estimate the increment in CRSS (critical resolved shear stress) from shearable as well as shear resistant plate and rod-shaped precipitates and experimental verification of the same. This has been shown in Figure 6, where f is the volume fraction of the strengthening phase, b is the magnitude of the burgers vector of these dislocations (b= 0.286 nm), Γ is the dislocation line tension in the matrix phase, d_t is the mean diameter, t_t is the mean thickness, γ is the precipitate-matrix interfacial energy, G is the shear modulus of the aluminum matrix (25 GPa), v is Poisson's ratio (v=1/3), r_o is the outer cut-off radius for matrix dislocations (r_o=b). It must, however, be noted that these models are ideal and simplified representations of the microstructure and do not account for any kind of statistical deviations that show a marked presence in real microstructures, as seen in the research work of this dissertation. It is necessary to be able to capture these statistical variations in particle distributions to obtain a thorough structural understanding of these alloys.

The ability of coarse precipitates to dampen cyclic softening on application of cyclic loads (Calabrese and Laird 1974) as a result of dislocations shuttling between them, has drawn attention to this class of microstructures on improving fatigue resistance. By

measuring asterism in Laue patterns and observation of strain-contrast in the lattice using transmission electron microscopy, Russel and Ashby concluded on the presence of large gradients in shear strain in the vicinity of such coarse θ′ precipitates and also developed appropriate expressions to quantify the same (Russell and Ashby 1970). They were able to relate the local shear strain (γ) at the particle-matrix interface to the observed increment in flow stress in the alloy.

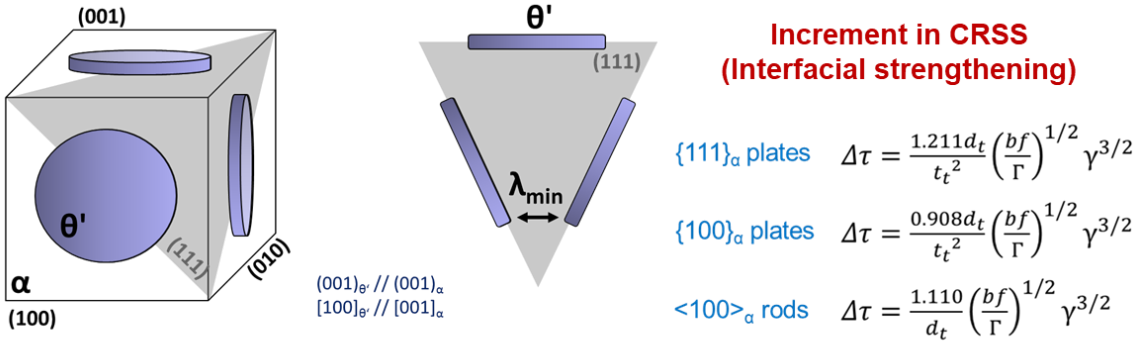

Figure 6: Schematic showing crystallographic distribution of θ′, along with equations quantifying the increment in CRSS for different precipitate distributions.

Adapted from (J. F. Nie and Muddle 1998).

This critical review of published literature on aluminum alloys highlights the shortcomings present in our current understanding of precipitation-strengthened alloys. To that effect, the research work in this dissertation aims to fulfill the following objectives:

1. Characterize and quantify the size, distribution, morphology and orientation of nanoscale θ′ and θ precipitates in three-dimensions non-destructively using Transmission X-Ray Microscopy.
2. Deduce the mechanisms behind the evolution and coarsening behavior of these nanoscale precipitates at high temperatures as a function of aging time using 4D nano-computed tomography.
3. Correlate the local micro-mechanical behavior of Al-Cu alloys with their non-destructively characterized 3D microstructure, using miniaturized mechanical testing techniques followed by transmission electron microscopy analysis.
4. Design and implement a compact nanoindentation system to perform *in situ* 4D nanoscale mechanical testing and understand the initiation and evolution of damage in 3D.
5. Establish a standard routine for accurate and quantitative automated segmentation of Nano-CT data using deep learning to facilitate rapid analysis of large volumes of material.

CHAPTER 3

PROBING NOVEL MICROSTRUCTURAL EVOLUTION MECHANISMS IN ALUMINUM ALLOYS USING FOUR-DIMENSIONAL NANOSCALE CHARACTERIZATION

3.1 Introduction

Since the discovery of the age hardening phenomena by Guinier (Guinier 1938) and Preston (Preston 1940) almost a century ago, it has been well-known that the ultra-high strength of aluminum alloys arises from the complex distribution of nanoscale second phase precipitates in the aluminum matrix that hinder dislocation motion. When the single-phase solid solution is rapidly quenched, these alloys form a supersaturated solid solution of Cu in Al. On subsequent aging, precipitation of various metastable intermediate second phase particles occurs, depending on the alloy's composition and temperature. GP-I zones, which are essentially monolayer discs of Cu atoms, are the first of these metastable phases, that further coarsen into GP-II zones (θ″): 3 Al layers sandwiched between 2 monolayers of Cu atoms (Yoshida, Cockayne, and Whelan 2006). These transition to the plate shaped θ′ phase (Al_2Cu) which possesses a tetragonal crystal structure and whose broad faces are coherent with the α matrix ($(001)_{\theta'} \parallel \{001\}_{Al}$) (Laird and Aaronson 1966). The θ′ phase transforms to the relatively more incoherent equilibrium θ phase (Al_2Cu with a different lattice structure). The equilibrium morphology of the precipitates is a result of the interplay

between the anisotropy of interfacial energy and elastic energy (Vaithyanathan, Wolverton, and Chen 2004).

Precipitate evolution during aging involves complex transitions in the crystallographic structure and interfacial relationships of the particles with the aluminum matrix. Understanding these processes is critical to modeling the alloy's mechanical as well as thermodynamic response. Early seminal work in trying to understand microstructural evolution and coarsening of the precipitates has been conducted over the last few decades using transmission electron microscopy (TEM). Although a very useful tool, it is limited by the fact that the specimen is ultra-thin, giving essentially two-dimensional information on a complex three-dimensional problem. Intricate details of 3D spatial distribution, structural complexities and mutual interaction, unfortunately, cannot be captured using electron microscopy. For instance, there is still much debate about the mechanisms causing precipitate evolution, ranging from the role of interfacial ledges (Sankaran and Laird 1974) to the nucleation sites of these second phase particles (Laird and Aaronson 1966). High temperature evolution studies (Kang and Laird 1975; Laird and Aaronson 1966; Thomas and Whelan 1961) carried out in the TEM not only pose severe stereographic challenges in understanding microstructural changes but also potentially mask the bulk behavior of the alloy due to the high surface-to-volume ratio of the specimen causing enhanced surface diffusion, which also significantly overestimates the measured diffusion coefficients from these techniques (Kang and Laird 1975; Laird and Aaronson 1966).

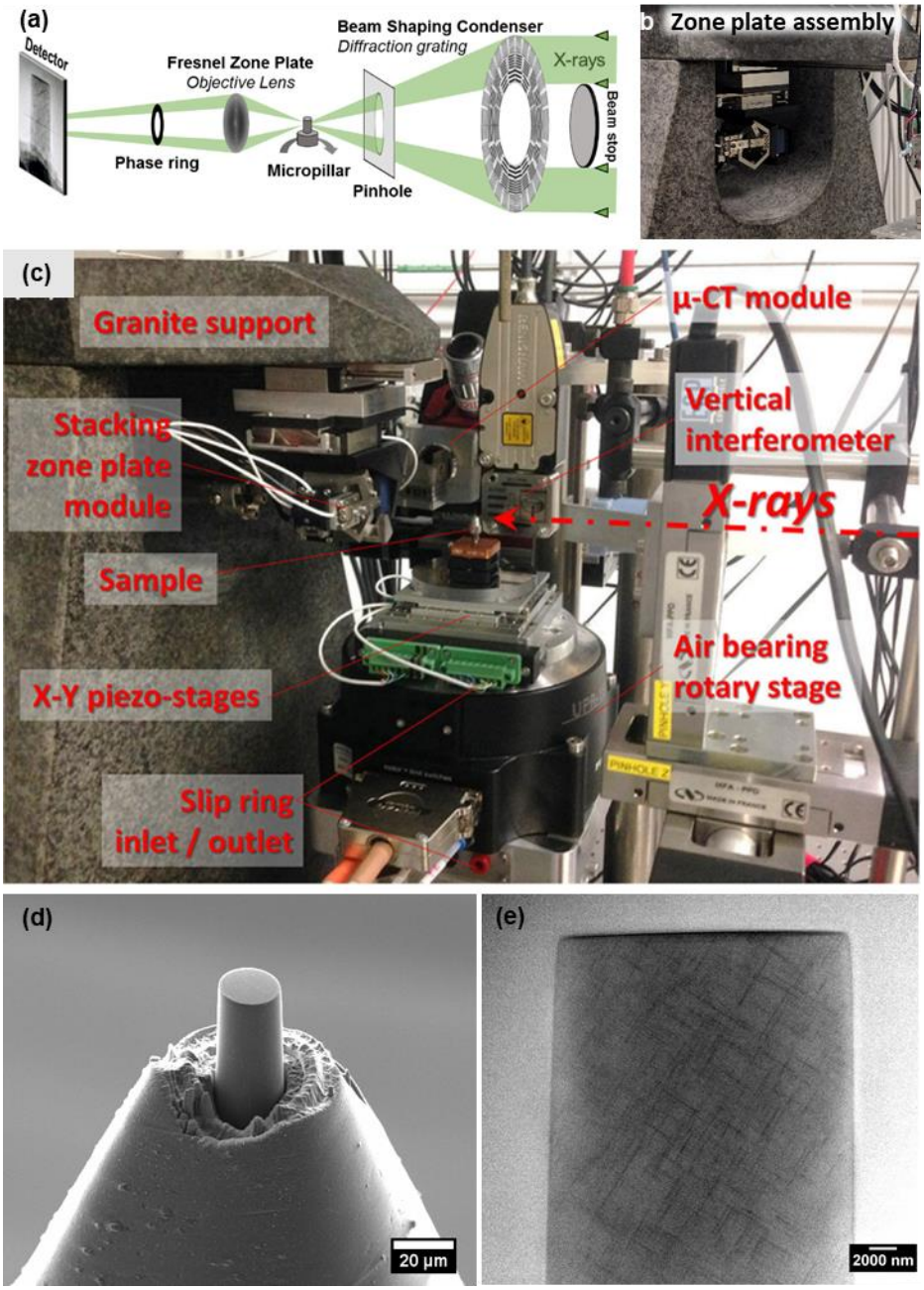

Figure 7: (a) Schematic of the TXM setup showing its principle of operation. (b), (c) TXM Instrument setup at Sector 32-ID-C (APS). (d) SEM micrograph showing a micropillar (20 × 40 μm) fabricated at the tip of Al-4wt%Cu wire. (e) 2D TXM absorption radiograph of the micropillar showing contrast from the precipitate phases.

Since the discovery of X-rays, their non-destructive nature of characterization has been leveraged extensively for several decades now, to probe the behavior of materials *in situ* as a function of time. Advent of X-ray computed tomography (3D Characterization) paved way for the dawn of "4D Characterization" (time being the fourth dimension), a technique that has truly revolutionized *in situ* studies in materials science by allowing three-dimensional visualization of changes in the internal structure of a material under external stimuli. This encompassed investigation of numerous fundamental phenomena such as dendritic solidification (Limodin et al. 2009), initiation and propagation of failure at high temperatures (Bale et al. 2012), changes in 3D crystallographic orientation (using X-ray diffraction contrast tomography) (King et al. 2010), etc. However, all these applications are restricted to analysis of features on the micrometer-scale due to limitations in spatial resolution (owing to sensor size on the CCD). Imaging using X-rays, however, does have the potential to offer very high spatial resolutions due to their significantly small wavelengths. Fortunately, breakthroughs in nanofabrication techniques have enabled the use of hard X-ray microscopy in probing the structure of materials in the nanoscale-regime (Chandrashekara S Kaira et al. 2016). Fabrication of sophisticated diffractive optics that form magnified high-resolution radiographs has led to a new generation of full-field X-ray microscopes which allow 3D analyses of large volumes of material at unprecedented length scales. X-ray imaging on metallic systems, to probe their microstructure, requires higher X-ray energies which typically results in a drastic drop in efficiency with the use of Fresnel Zone plate (FZP) optics (Gorelick et al. 2011). The low flux of X-rays associated with lab-scale X-ray microscopes renders them ineffective for such applications. However, the new

in-house Transmission X-ray Microscope (TXM) installed at sector 32-ID-C of the Advanced Photon Source (APS) (Figures 7 & 8) is one such synchrotron-based X-ray microscope that is pushing the global frontiers of hard X-ray nanotomography by using high aspect ratio zone plates and is capable of imaging at energies up to 15 keV, with spatial resolutions of 20 nm and 60 nm (De Andrade et al. 2016). This study presents unprecedented mechanistic insights that were made using this technique in understanding 3D nanoscale microstructural evolution in Al-Cu alloys, by unearthing new transformation sequences and validating Ostwald ripening models from several decades ago using systematic quantitative analyses of large precipitate ensembles.

Furthermore, understanding deformation behavior in precipitation-strengthened alloys is quite non-trivial. Several models and theories have attempted to explain the interaction of dislocations with different kinds of precipitates (S. Y. Hu et al. 2006; Zhu and Starke 1999). However, these haven't been experimentally verified, and also make several underlying assumptions about the morphology of the precipitates. A comprehensive model that accounts for 3D dislocation storage and interactions with multimodal distributions of varying precipitate sizes is still lacking. Our experiments demonstrate the ability to virtually probe the 3D microstructure and non-destructively quantify parameters such as the critical precipitate shearing stress, Orowan looping stress, and inter-precipitate dislocation cell size, which is a colossal step in this direction and can have seminal implications in predicting the mechanical response of these and other high performance materials.

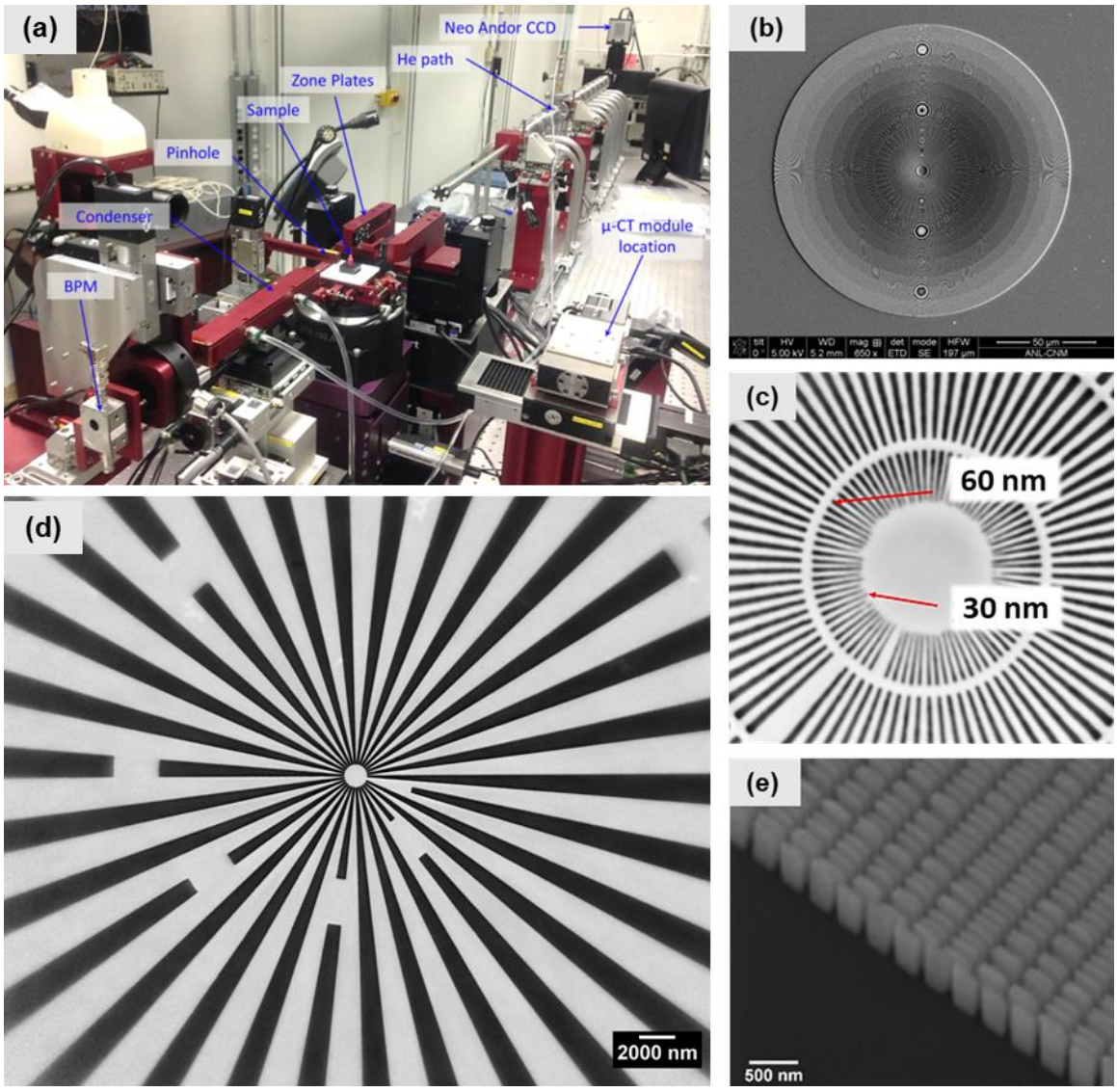

Figure 8: (a) Extended view of TXM Instrument setup at Sector 32-ID-C (APS). (b) SEM image showing a 20 nm Fresnel Zone plate (FZP) objective lens. (c) Absorption radiograph of a Siemens star showing sub-20 nm spatial resolution. (d) Absorption radiograph of 100 nm Siemens star imaged using 60 nm FZP objective lens. (e) SEM image of 60 nm FZP fabricated using a Diamond mold & Au zones.

3.2 Materials and Experimental Procedure

Al-4wt.%Cu wires (99.999% purity) having a 0.5 mm diameter (Princeton Scientific Corp., Easton, PA, USA) were mechanically sharpened to fine tips. These wires were solution treated at 535 ^{o}C for sufficiently long times to obtain large grain sizes, followed by immediate quenching into ice water and subsequently aged at 350 ^{o}C and 400 ^{o}C, respectively. The reason for the choice of relatively high aging temperatures was two-fold: time-sensitivity for performing experiments at the synchrotron and ability to spatially resolve all the precipitates present in the given volume. The instrument's limited depth of field necessitated fabrication of micropillars, having a 30 μm diameter and 50 μm in height, at the fine tips of sharpened wires using a dual-beam focused ion beam (FIB) with a scanning electron microscope (Nova 200 NanoLab FEGSEM/FIB, FEI Co, Oregon) (Figure 10(a)). A Ga+ ion beam, at an accelerating voltage of 30 keV, was used at a range of currents, starting with 20 nA to mill out a coarse pattern, followed by final polishing at 5 nA and 1 nA, respectively, to minimize taper.

Absorption full-field hard X-ray nano-computed tomography was performed using the new Transmission X-ray Microscope (TXM) of the Advanced Photon Source (APS) at sector 32-ID-C. Imaging was performed using a monochromatic beam at 9.1 keV, just above the Cu K-edge to maximize contrast between the Al_2Cu and Al phases (Figure 9). A Beam Shaping Condenser (BSC) (Vogt et al. 2006) which provides Koehler-like homogeneous sample illumination was used as a condenser to focus X-rays onto the sample.

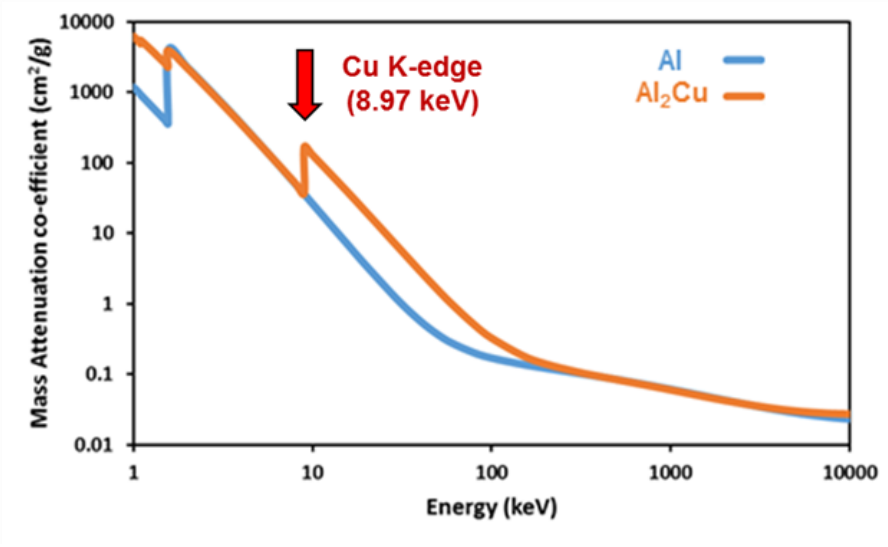

Figure 9: Mass attenuation co-efficient plot as a function of X-ray Energy showing the Cu absorption K-edge and the onset of difference in attenuation between the Al_2Cu and Al phases.

The condenser divergence matches the numerical aperture of a 180 µm large Fresnel zone plate with 60 nm outer most zone width, which was used as a microscope objective lens to magnify radiographs of the sample placed on a high accuracy air-bearing rotary stage and a magnification of ~39 was obtained. The X-ray detection system included an assembly of a LuAG scintillator, a 10X microscope objective, a 45^o mirror and a low-noise fast CCD cooled at -40 ^{o}C. A more detailed description of the stage design can be found elsewhere (De Andrade et al. 2016). A schematic of the setup, depicting the assembly of optics used in these experiments and showing the TXM's principle of operation, is shown in Figure 7(a). A voxel width of 16.6 nm was obtained in this geometry and the field of view was about 35 x 42 µm^2 while the illumination coming from the beam-shaping condenser (BSC)

was about 50 µm in diameter. Each scan comprised of 2D projections taken at 0.25^{o} angular increments from 0^{o} to 180^{o} with an exposure time of 2 s per projection. Tomograms were obtained at all aging conditions and for the first time, it has been possible to track 3D microstructural changes in bulk at this length scale. The amplitude of mechanical vibrations was reduced to about 4 nm (RMS) using an ultra-stable stage design and it was possible to extract the best spatial resolution from the X-ray optics and resolve precipitates that were as little as 60 nm in thickness.

Post scanning, the tips of the samples were cross-sectioned using the FIB at an accelerating voltage of 30 keV and using a current of 1 nA. EBSD was performed on these flat sections, using a step size of 0.5 µm to identify the grain orientation. The acquired data was analyzed using TSL® OIM data collection and analysis software. Tomopy, an open source Python based toolbox used to analyze synchrotron tomography data (De Carlo et al. 2014; D Gürsoy et al. 2014), was used to perform 3D reconstructions (D M Pelt et al. 2016; Daniel M. Pelt and Batenburg 2015). The stack of tomograms was post-processed using a combination of Mean 3D, Bandpass and Non-local means denoise filters in ImageJ (C. A. Schneider, Rasband, and Eliceiri 2012) as shown in Figure 12. Use of 3D filters was seen to improve the quality of the image stacks owing to the three-dimensional nature of the data. The Bandpass filter was used to normalize the background and enhance contrast. The Non-local means filter (Buades, Coll, and Morel 2005) which is an edge-preserving filter, improved the quality of individual features present in images (noise reduction) and enhanced their contrast, without distorting their edges. This allowed for smoother segmentation of precipitates, performed in 3D using the magic wand tool in Avizo® Fire.

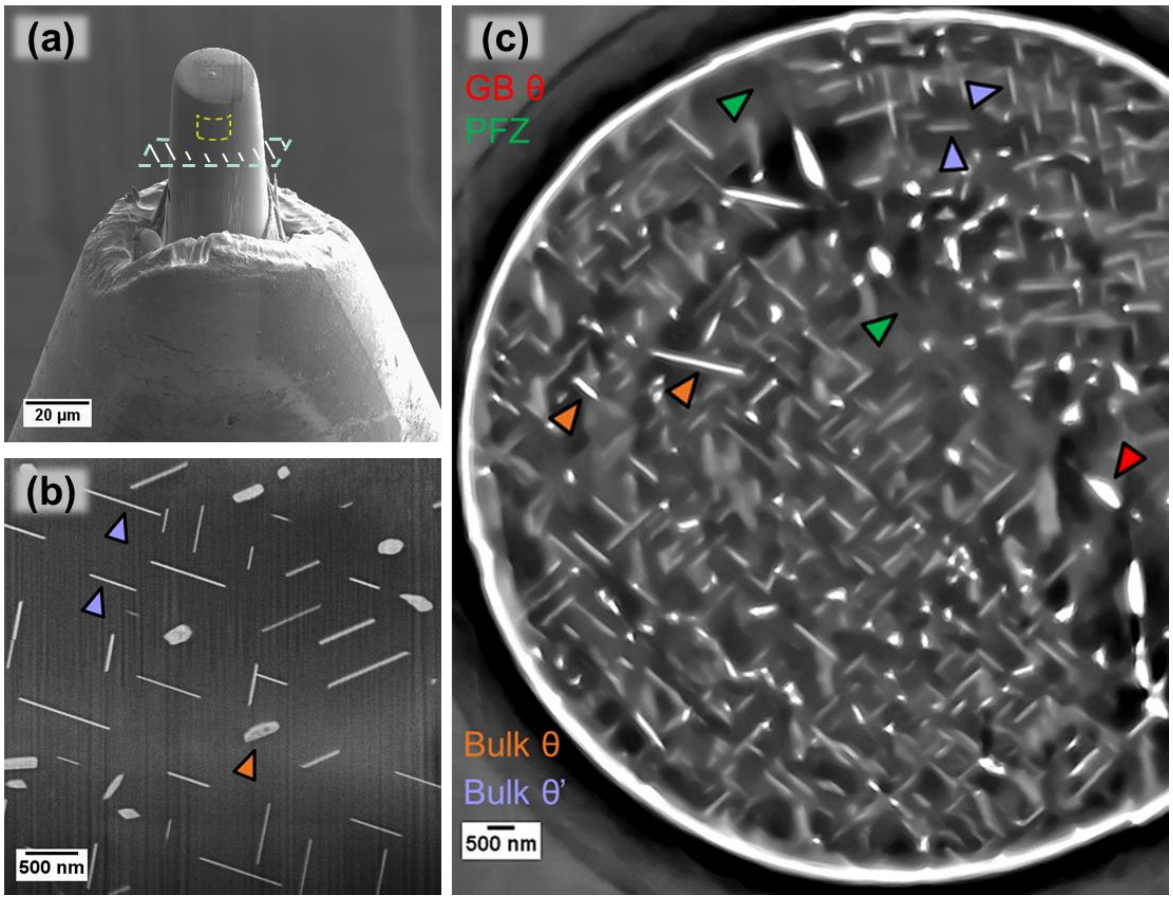

Figure 10: (a) SEM micrograph showing a micropillar (30 × 50 µm) fabricated at the tip of Al-4wt%Cu wire. (b) SEM micrograph showing a magnified view of the micropillar's surface where different precipitate phases are clearly visible. (c) 2D TXM slice from a reconstructed dataset (T = 350 °C, t = 45 min) showing a cross-sectional plane of view from within the micropillar. The grain boundary, different phases (θ′ and θ) as well as the precipitate free zone (PFZ) have been highlighted.

Subsequent 3D quantification as well as 3D visualization was also carried out in Avizo® Fire. The relatively diffuse nature of the interface between phases in TXM images (as compared to SEM images) in evident from Figure 11. However, such SEM Images can aid in more accurate and quantitative segmentation/binarization of features from 3D TXM datasets.

The tip of the scanned sample (aged at 400 ^{o}C) was cross-sectioned normal to the rotation axis using a focused ion beam (FIB). EBSD data acquired from the flat section was used to determine the crystallographic orientation of the α-Al matrix. The grain sizes of the samples under study were quite large (~400 μm) and hence, data gathered from both the techniques were used to complement each other as they corresponded to a single grain. Miller indices of the plane normal to the scanning axis were utilized to transform the local coordinate axes of the sample in 3D to correspond to the crystallographic axes of the Al matrix. The 3D orientation data of the precipitates obtained from Nano-CT, was transformed to crystallographic Euclidean coordinate space, before being exported into MTEX, a texture analysis toolbox in MATLAB, to construct pole figure maps (Hielscher and Nolze 2016). Scripts in MATLAB were written to compute the mean planar particle diameter (D_p) and the planar inter-particle spacing (λ) by 2D finite body tessellation using Euclidean distance maps.

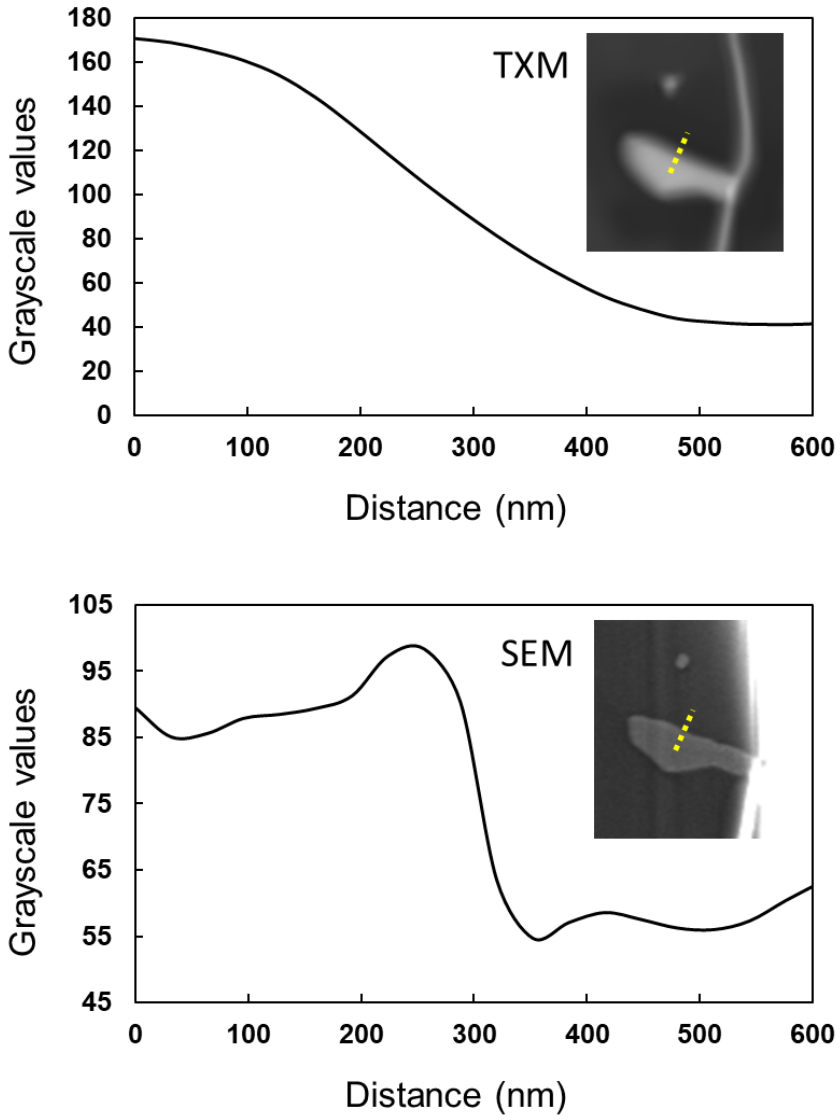

Figure 11: Comparison of Grayscale intensity line profiles across the interface of a selected feature from corresponding TXM and SEM Images.

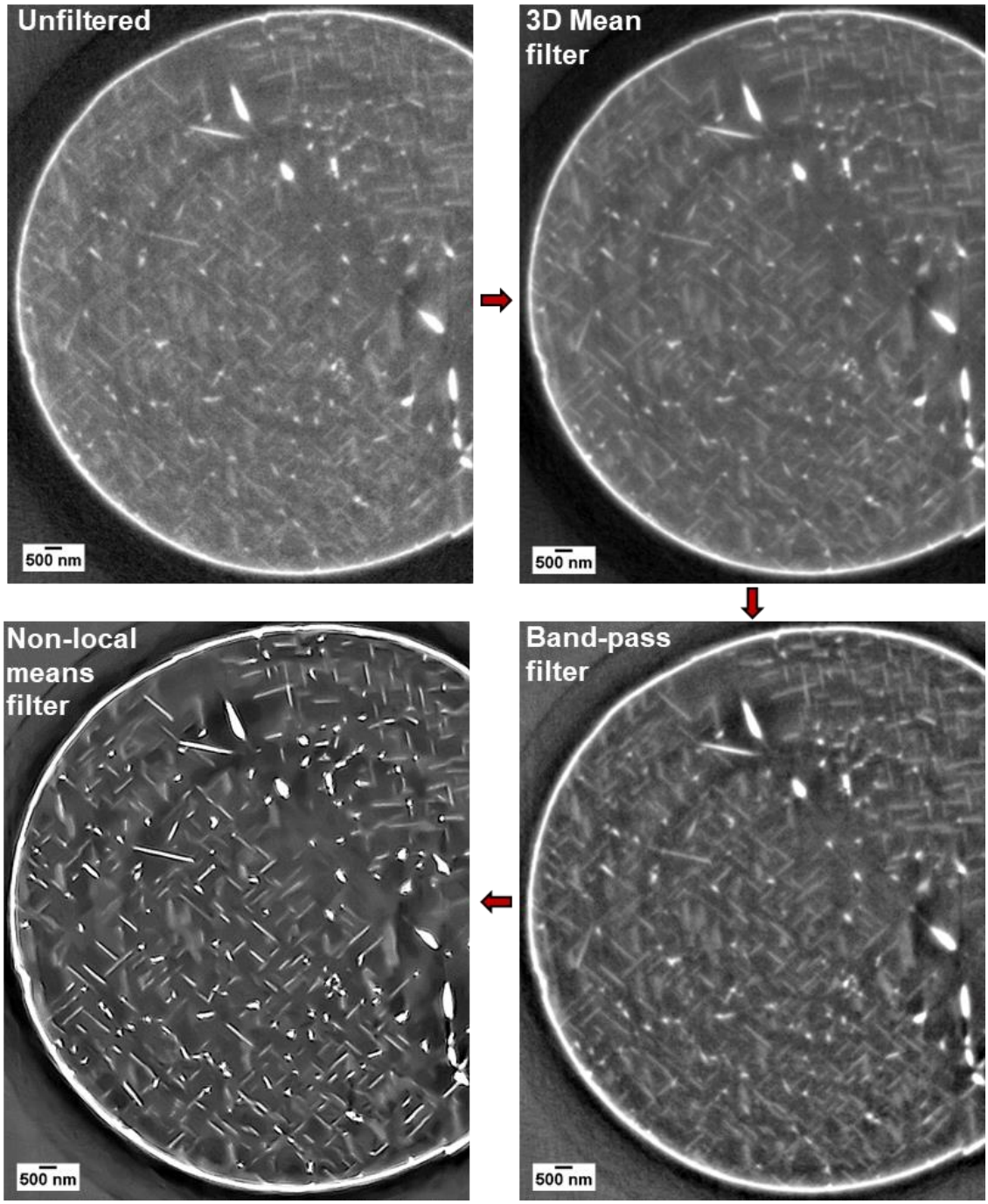

Figure 12: Application of Image processing filters on a 2D TXM slice acquired from the 3D reconstruction.

3.3 Results and Discussion

3.3.1 4D Microstructural characterization at 350 ºC

A range of precipitate sizes and shapes were observed in the Al-Cu alloy aged at 350 ^{o}C. A 2D slice from the reconstructed 3D dataset showing the different phases present is shown in Figure 10(c). A stark difference in the absorbance as well as morphology of the two phases aided in discerning them from each other. It was apparent from the 3D visualizations that the θ′ precipitates primarily exist as orthogonally oriented plates, while the θ precipitates in the grain interior are more needle/lath-like and randomly oriented. Grain boundaries, however, promote early heterogeneous nucleation of θ precipitates due to their higher energy, resulting in a much coarser θ phase. Their shape is a function of the grain boundary's character and misorientation. Figure 14 shows a four-dimensional (4D) rendering of the microstructure for different aging times from a region sampled near a grain boundary in the scanned micropillar. The volume fraction of θ′ was seen to reduce and that of θ increased. The 3D tomography data allowed visualization of these bulk transformation reactions, as shown in Figure 15. Laird and Aaronson were able to observe some of the transformation sequences occurring in an Al-Cu alloy using a hot-stage specimen holder in a TEM (Laird and Aaronson 1966). One of the most commonly observed reactions in their study was the dissolution of θ′ and the growth of θ without actual contact but by countercurrent diffusion of aluminum and copper through the α matrix. However, this study has been able to show, for the first time, otherwise, as discussed below. Although diffusion through the matrix does play a role in dissolution and growth of precipitates, θ is generally

seen to nucleate and grow from θ′- θ′ or θ′- θ intersections and this can be easily missed when viewed in 2D due to the precipitate's complex morphology.

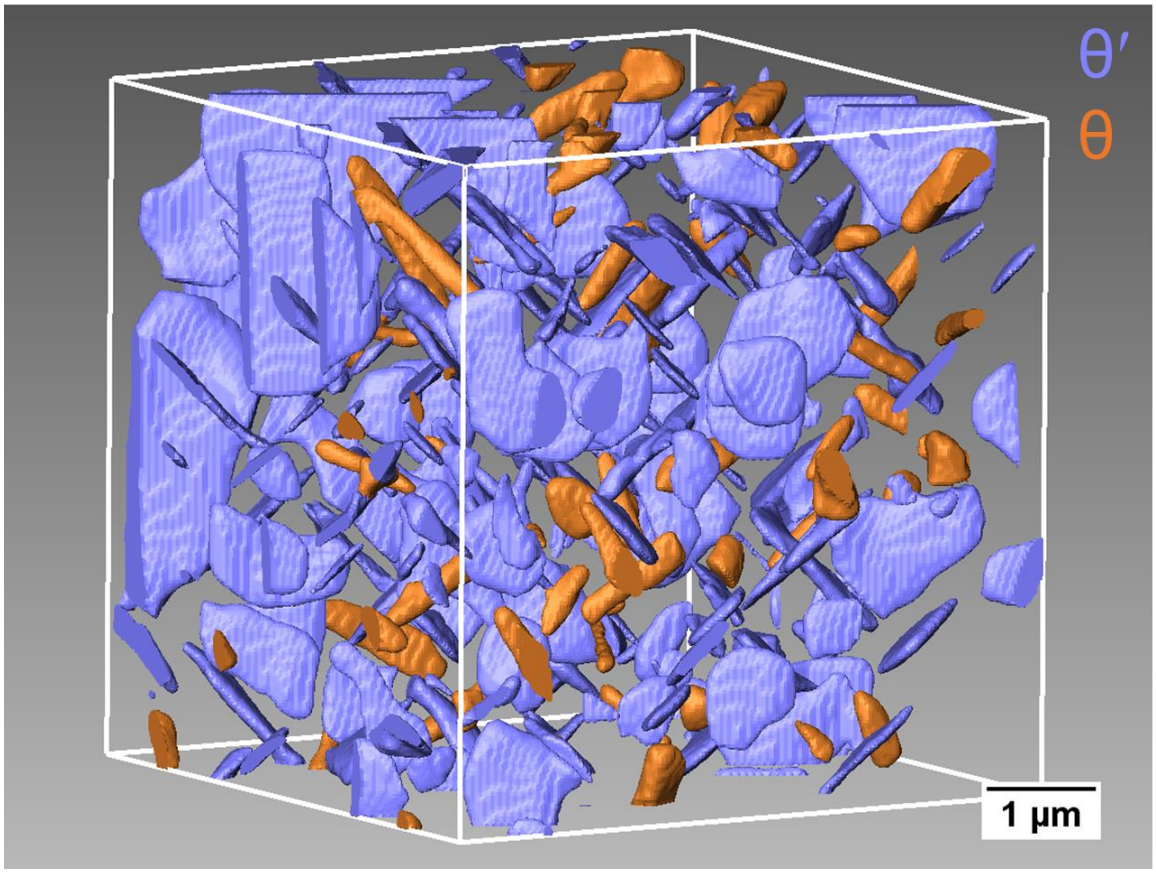

Figure 13: Nanoscale 3D rendering of the microstructure of an Al-4%Cu alloy (T = 350 °C, t = 45 min) has been depicted.

The nucleation of θ was most commonly seen to occur at θ′- θ′ intersections (Figure 15(a)) and its growth occurred at the expense of these θ′ plates, eventually causing them to split up and shrink. This can have an important impact on the alloy's mechanical properties due to a transition in the interfacial structure of precipitates (θ′ to θ) & their number density.

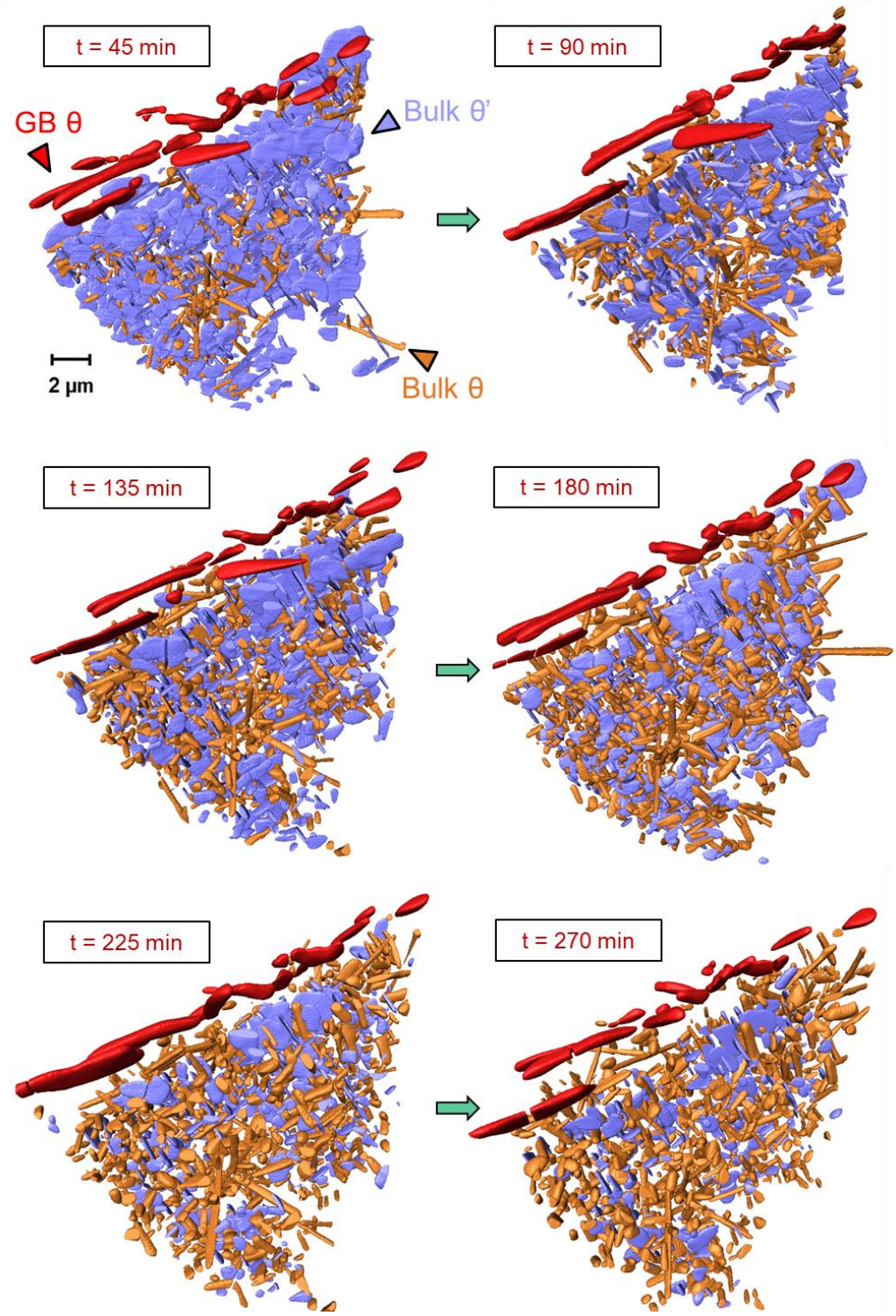

Figure 14: Nanoscale 3D rendering of microstructural evolution (of θ′ and θ) with aging time (T = 350 °C) has been depicted.

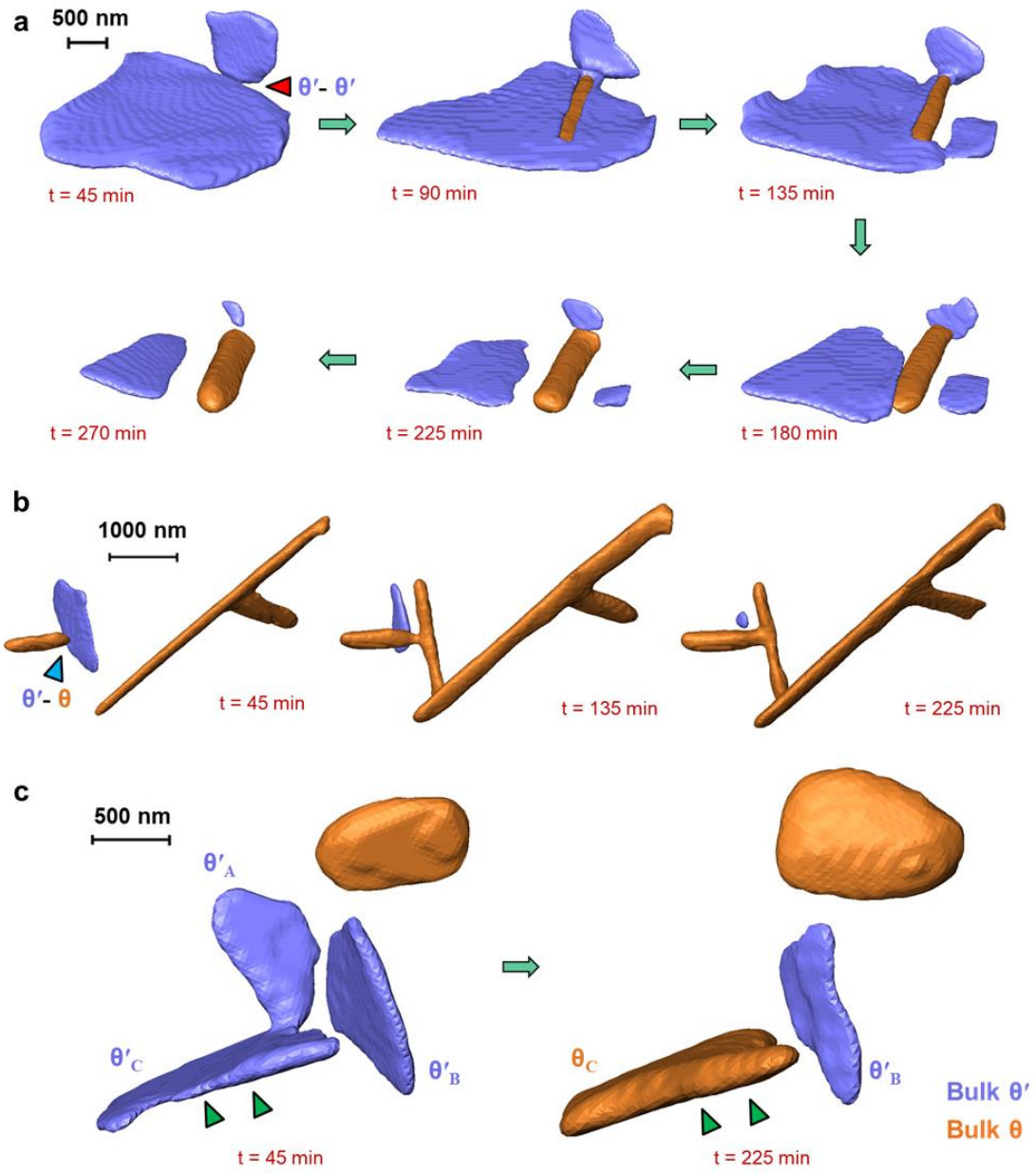

Figure 15: 4D microstructural transformation reactions (θ′ to θ) occurring during aging at 350 °C: (a) Nucleation and growth of θ from θ′-θ′ intersection. (b) Nucleation and growth of θ from θ′-θ intersection. (c) Varying transformation of different θ′ precipitates.

Less commonly, θ was also seen to nucleate from θ′- θ intersections (Reaction 2, Figure 15(b)) and a smaller proportion of θ′ plates directly transformed into morphologically similar θ plates (Reaction 3, Figure 15(c)).

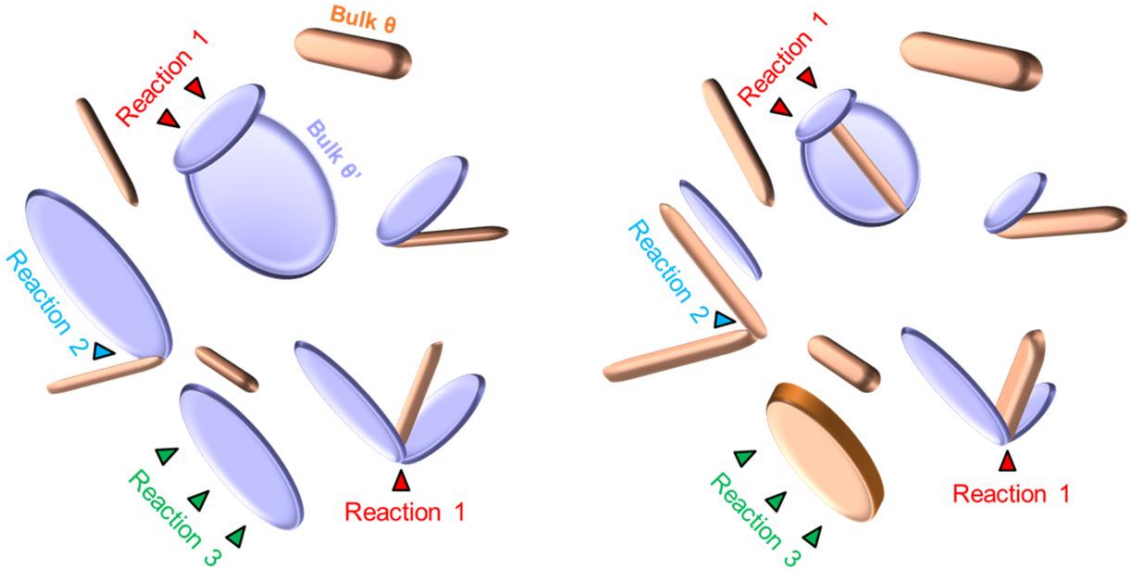

Figure 16: Schematic representing different 3D transformation reactions (θ′ to θ).

Another important observation is the dissimilarity in dissolution/growth rates of individual precipitates. This highlights the heterogeneity in diffusional interactions, which is a direct result of the local spatial distribution of precipitates. This has been exemplified in Figure 15(c) where the precipitates θ'_A and θ'_B dissolve at different rates, while θ'_C transforms into a morphologically similar θ phase.

The unique ability to measure and track an individual precipitate's dimensions in 3D as a function of temperature and time (Figure 17(a)) also allowed us to estimate the bulk

diffusion coefficient (D_{bulk}) of Cu in Al, by employing the Zener-Hillert expression (Hillert 1957; Zener 1946),

$$\frac{vR_{tip}}{D_{bulk}} = \frac{(X_{bulk} - X_{eq}^{\alpha/\theta})}{2(X_{\theta} - X_{eq}^{\alpha/\theta})}\left(1 - \frac{R_c}{R_{tip}}\right) \quad (1)$$

where R_{tip} is tip radius of the θ needle (~half of its width), v is its growth velocity, R_c is the critical radius of curvature (which can be assumed to be $0.5R_{tip}$ (Hillert 1957; Zener 1946)), X_{bulk} is the bulk Cu concentration in the alloy, $X_{eq}^{\alpha/\theta}$ is the equilibrium concentration of Cu at the α/θ interface and X_{θ} is the concentration of Cu in θ phase. D_{bulk} was found to be on the order of 10^{-16} m^2/s, which is, again, in excellent agreement with values computed using other techniques (Mantina et al. 2009). It must also be noted that lengthening rates measured in the TEM yielded extremely high diffusivity values (Kang and Laird 1975; Laird and Aaronson 1966) on the order of 10^{-14} m^2/s, where an obvious influence of surface diffusion is apparent.

As aging progressed, the average aspect ratio of the θ′ precipitates computed in 3D was found to stabilize from a value of about 3.5 to ~3 (Figure 18). This is in excellent agreement with the equilibrium aspect ratio computed in Vaithyanathan et al.'s study (Vaithyanathan, Wolverton, and Chen 2004) using first-principles calculations by accounting for interfacial energy anisotropy. As precipitate thicknesses in the present study are relatively large, it must be noted that misfit strains are minimal (Vaithyanathan, Wolverton, and Chen 2004) and hence, the effect of elastic energy anisotropy on the aspect ratio can be safely ignored.

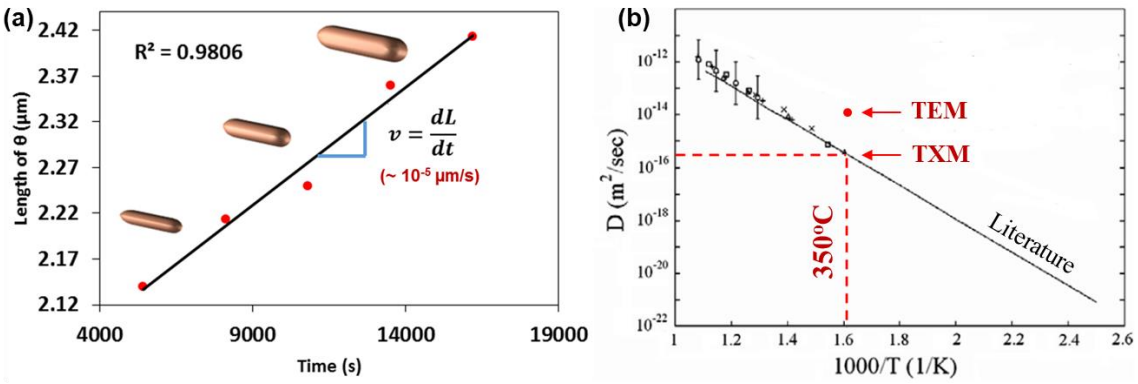

Figure 17: (a) Variation in length of θ as a function of aging time (at T = 350 °C). (b) Comparison of diffusivity values obtained from the current TXM study with those obtained using conventional techniques as well as TEM (Laird and Aaronson 1966). Reprinted from (Mantina et al. 2009).

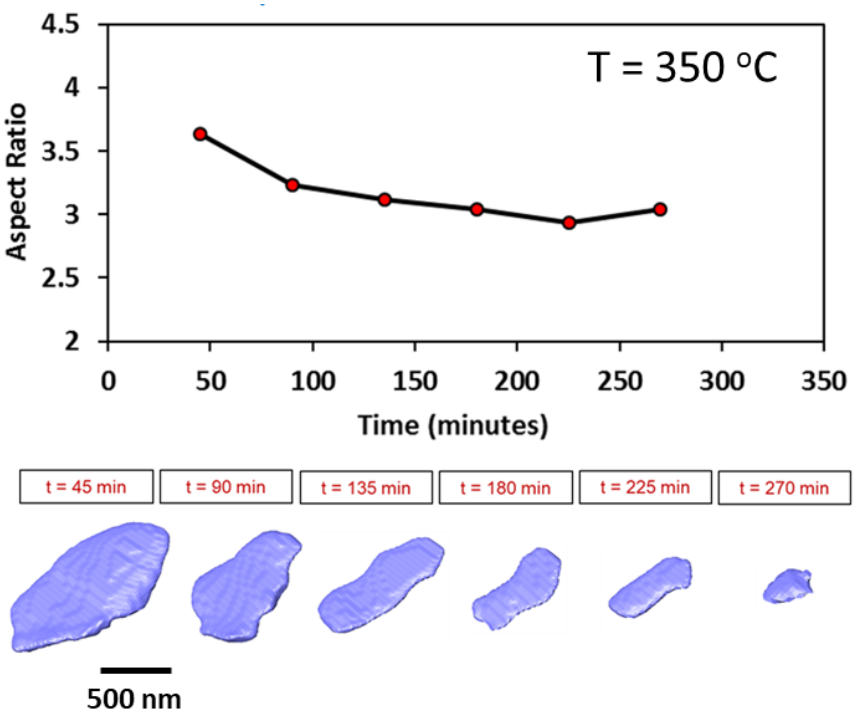

Figure 18: Average aspect ratio variation in θ′ precipitates, with aging time.

3.3.2 4D Microstructural characterization at 400 ^{o}C

Coarsening has been widely observed in a variety of particle-dispersed systems, where the system strives to attain thermodynamic stability by minimizing the total surface energy of the ensemble. The LSW theory, put forth by Lifshitz and Slyozov (Lifshitz and Slyozov 1961) and Wagner (Wagner 1961), has been able to explain the diffusion-controlled Ostwald ripening process in great detail. It predicts the kinetics of the coarsening process (where mean radius of the particles obey a cubic growth law) and the scaled precipitate size distributions (PSDs) to be time invariant. This is a result of the average diffusional interactions between different particle size classes and the mean field (Baldan 2002). The shape of these curves allude to the kind of diffusion processes controlling coarsening. However, application of this theory on metallic systems has been largely debated since its inception and hence, several modifications (Ardell 1972; Davies, Nash, and Stevens 1980; Enomoto, Tokuyama, and Kawasaki 1986) were put forth that were able to better address the misfit between experiments and theory. It must also be noted that most of these studies focused on modifying the LSW theory to account for the apparent deviation obtained from 2D techniques. In other words, little attention has been paid to the experimental techniques used to validate the theory. It can be stereographically quite challenging and sometimes nearly impossible to extract accurate particle dimensions from 2D images (for instance, using transmission electron microscopy), due to complex particle morphologies. This can give rise to inaccurate size-distribution curves, which are crucial in discerning the rate-controlling diffusion mechanism during coarsening. This has been exemplified in Boyd and Nicholson's study on understanding coarsening behavior in Al-Cu alloys using TEM

measurements (Boyd and Nicholson 1971). Disagreements in coarsening behavior of θ′ phase with the LSW model was attributed to the presence of short-circuit diffusion paths. It is quite possible that a certain degree of experimental uncertainty in measurements was responsible for the observed disagreements, which has not been addressed. Most studies on Al-Cu alloys have found the experimental size-distribution curves to be broader when compared to their theoretical counterparts and various factors such as overlap of the particle's diffusion fields, coalescence, misfit strains, etc. have been attributed to this finding (Boyd and Nicholson 1971; Merle and Fouquet 1981; Voorhees and Glicksman 1984). There has also been an evident lack of common ground in the observed lengthening and thickening rates of these precipitates (Aaronson 1977), which also subsequently causes uncertainty in discerning the rate-controlling diffusion mechanism.

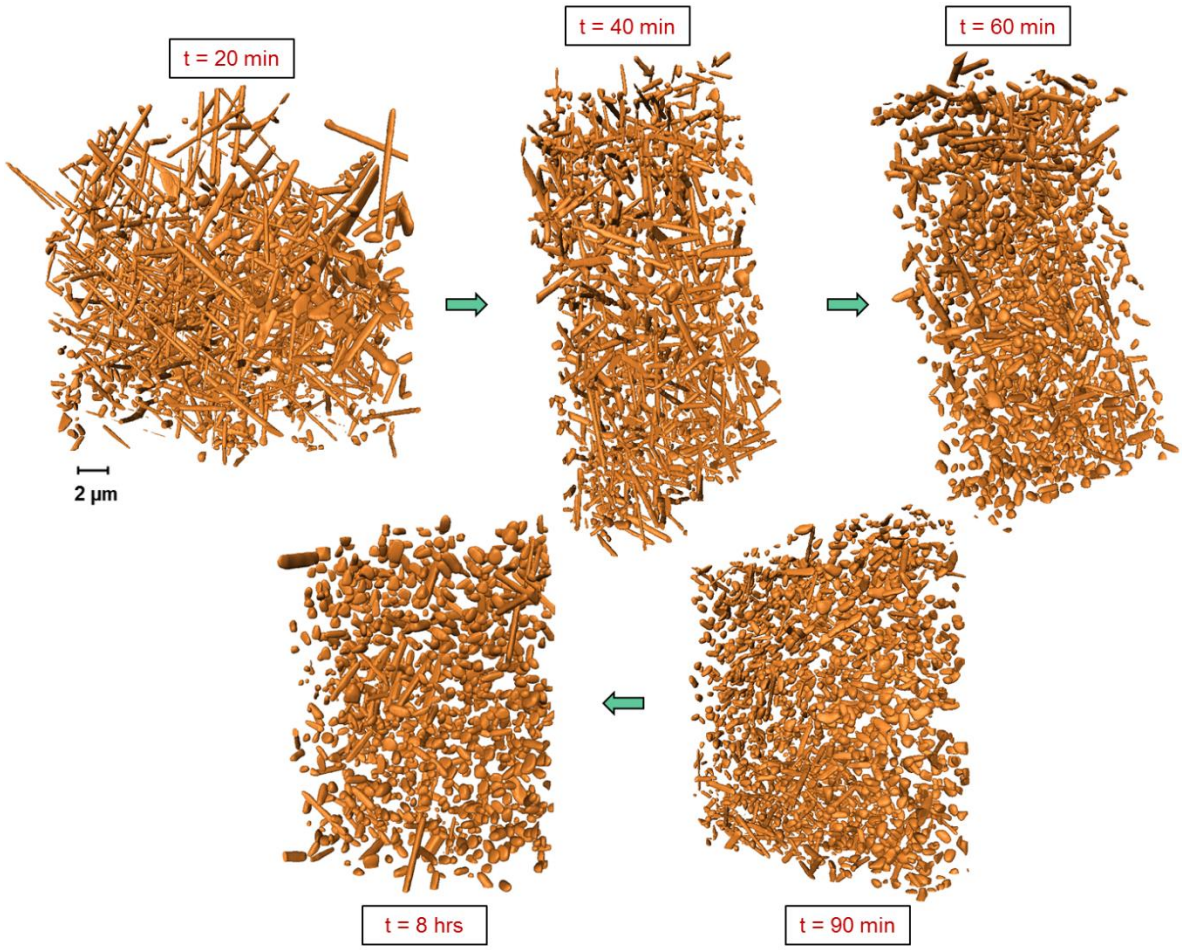

Figure 19: 4D microstructural evolution (of θ) with aging time (T = 400 °C) has been depicted.

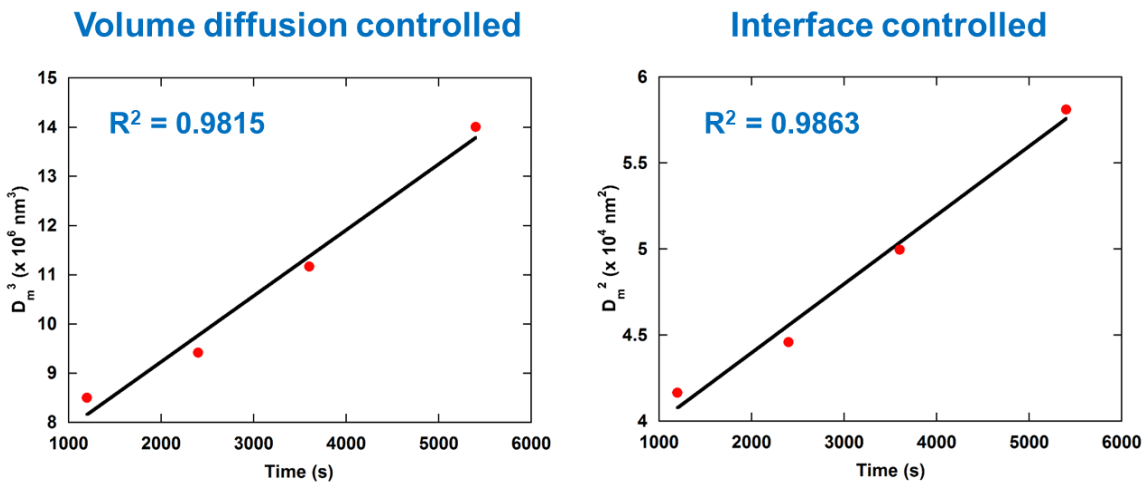

Figure 20: Graphs depicting good agreement for both the power laws D_m^2 vs. t and D_m^3 vs. t, where D_m and t are the Sauter Mean Diameter (for the entire assembly of precipitates) and time, respectively.

With the transmission X-ray microscope, it has been possible to sample statistically large volumes and quantify 3D orientation, 3D volume, 3D surface area, maximum and minimum Feret diameter of all individual particles. The Al-4wt.%Cu alloy was aged at 400 ^oC to closely monitor the coarsening of the θ phase alone (Figure 19). The Sauter Mean Diameter was calculated for the entire assembly of precipitates and its mean value was seen to be in good agreement with both the power laws D_m^2 vs. t and D_m^3 vs. t, where D_m and t are mean diameter and time, respectively (Figure 20). The PSDs obtained using the Sauter Mean Diameter were initially broad and seem to transition to better conformity with the theoretically predicted PSD for volume-diffusion by the LSW theory. The growth exponent as well as the scaled PSDs hint toward the possibility of both volume-diffusion as well as interface-controlled diffusive processes being operative. This hypothesis was validated by

constructing separate scaled PSD curves for both 3D length and thickness of the precipitates, respectively (as shown in Figure 21). From these curves, it can be concluded that the thickening of the θ phase is initially driven by interface-controlled growth. This is also corroborated by Kang and Laird's observation (Kang and Laird 1974) of planar interfaces of the θ phase being semi-coherent. The thickening later switches to volume diffusion controlled growth as the precipitates morphologically transform and their interfaces lose coherency, as evident from the scaled PSDs. The length of these precipitates on the other hand, is continually reduced by interface-driven diffusion, suggesting the diffusion of solute from the extremities along the periphery (driven by a difference in local radius of curvature). The coarsening of the θ phase is seen to occur primarily as an evolution of its shape to an equilibrium morphology (Figure 22). Although several theories predict broadening in the PSD curves as a result of volume fraction, it is likely that its role has been overstated as exemplified by our 3D measurements.

During the early stages of coarsening (at T=400 ^{o}C), there is an evident mismatch between the experimental and theoretical scaled PSD curves for the 3D length of the θ precipitates (Figure 21). This can be explained by considering their morphology and the driving force for interfacial diffusion in these precipitates. Reduction in length of the θ phase can be attributed to diffusion of solute flux along the interface, from the edge of the precipitate to its broad face due to difference in concentration (which occurs as a result of difference in their radius of curvature).

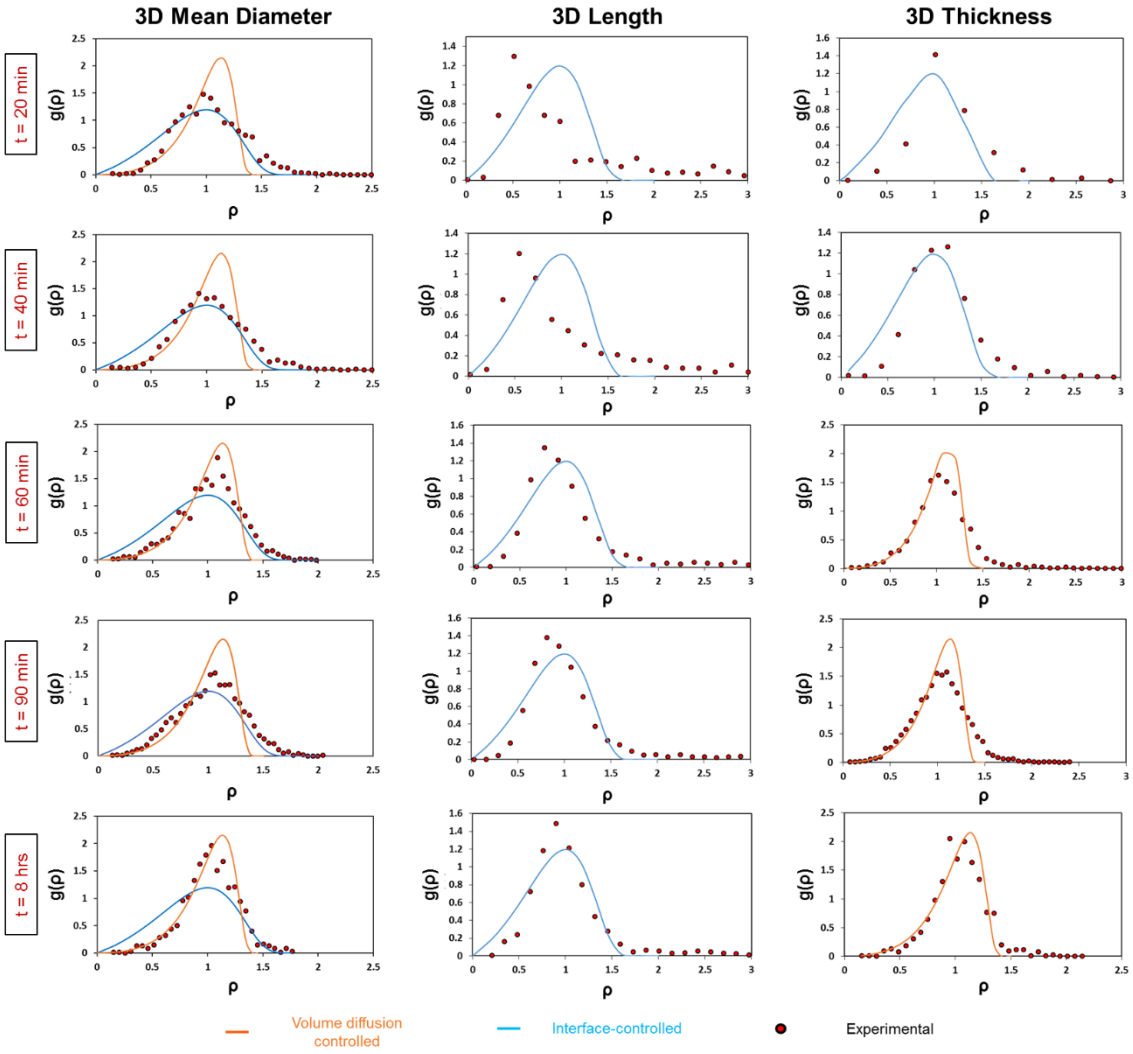

Figure 21: Scaled precipitate size-distribution (PSD) plots showing the rate-controlling diffusion mechanism (T = 400 °C). The vertical axis represents the scaled probability density g(ρ) while ρ represents the scaled particle dimensions. The growth in thickness of θ is initially interfacially driven but later switches to volume diffusion-controlled growth as the interfaces lose coherency. The reduction in length is always controlled by interfacial diffusion.

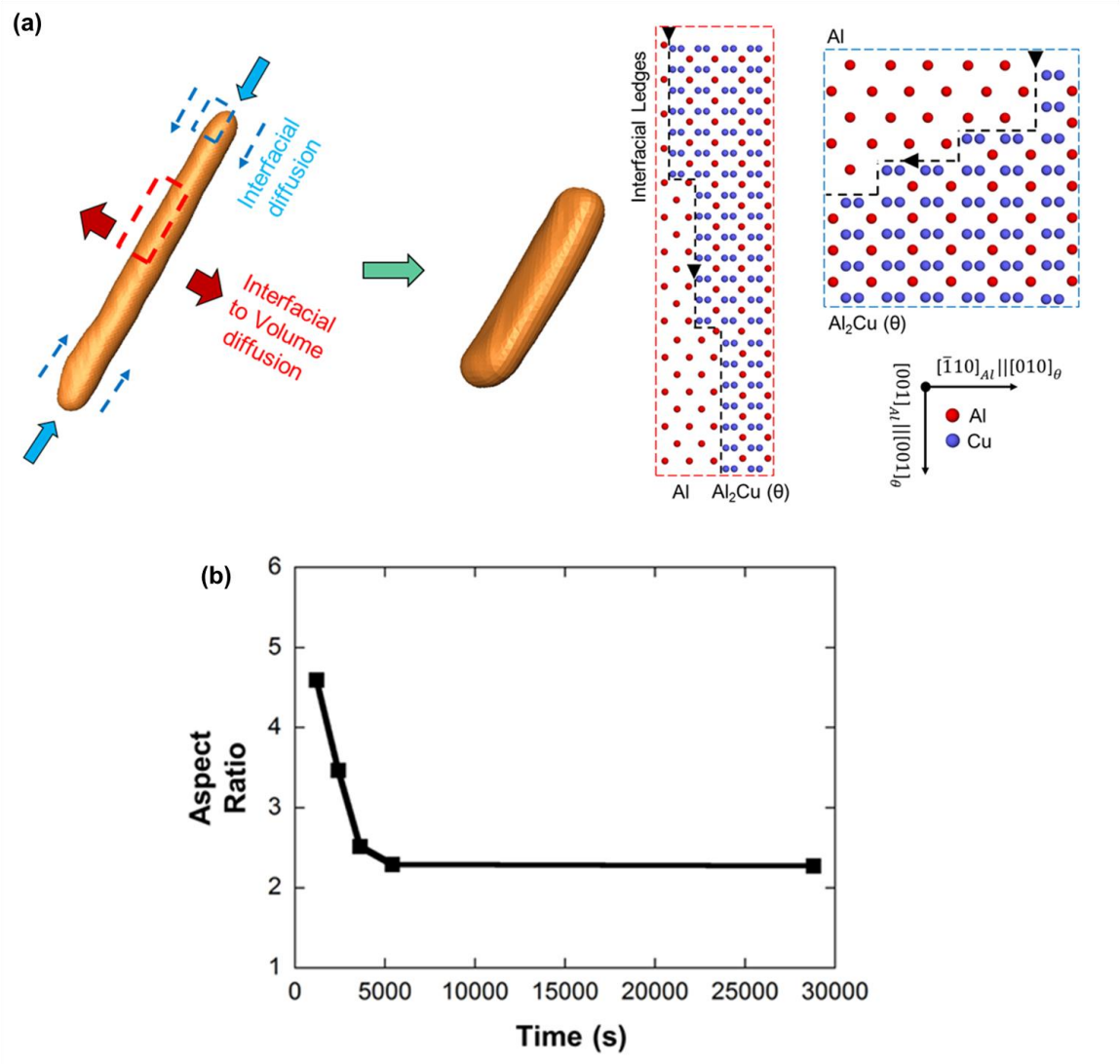

Figure 22: (a) Schematic representing the transformation of θ phase with magnified insets depicting diffusion processes on an atomic scale. (b) Quantification of reduction in aspect ratio of θ during aging.

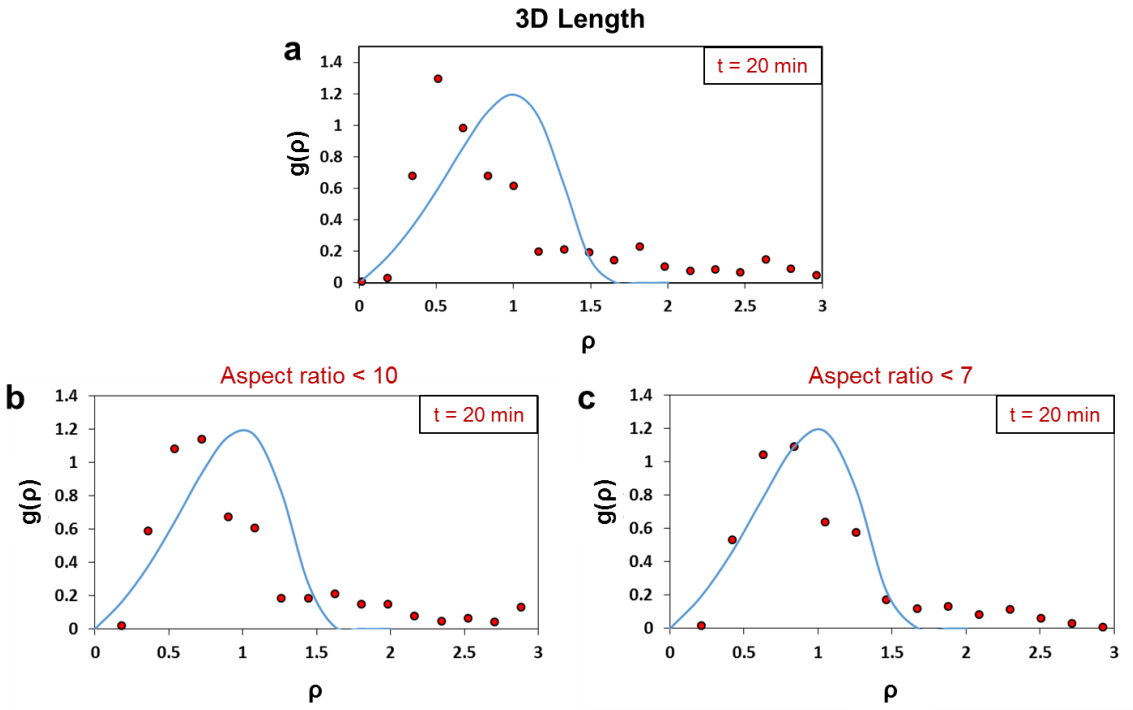

Figure 23: Scaled PSD curves for the 3D length of θ precipitates at the primary aging condition (T = 400 ^{o}C, 20 min). Selectively excluding high aspect ratio θ precipitates is seen to result in better conformity between experiments and theory.

In case of large aspect ratio θ precipitates, this difference is reduced as a result of their elongated morphology and hence, the contribution from interfacial diffusion is relatively lower. The low aspect ratio θ precipitates are more lath-like in morphology and have a higher difference in radius of curvature between their extremities and broad faces. This can be proven by constructing scaled PSD curves from θ precipitates that have aspect ratios lower than a fixed value (as shown in Figure 23). By considering θ precipitates with lower aspect ratios alone, the fit between experimental and theoretical scaled PSD curves is seen to improve drastically.

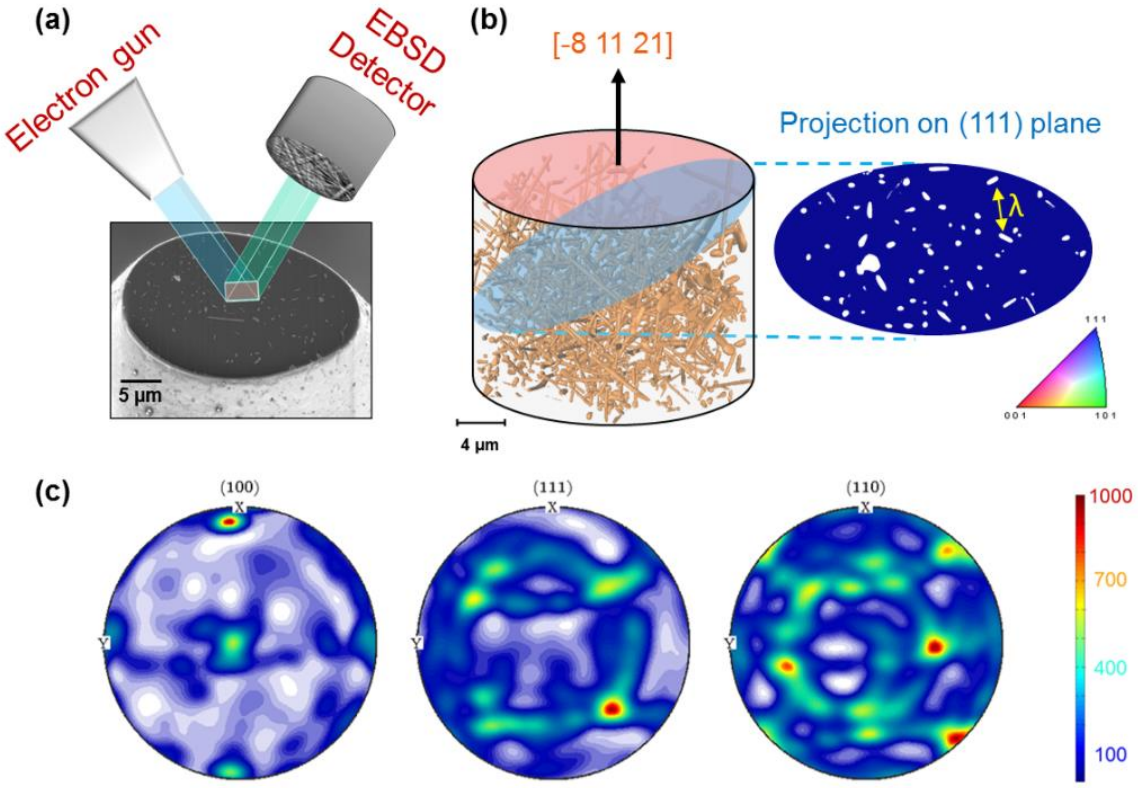

Figure 24: 3D Orientation Information. (a) Acquisition of EBSD data from FIB cross sectioned top surface of the Al-4wt%Cu wire aged to 400 °C. (b) Schematic showing resectioning of the virtual microstructure to obtain interparticle spacing (λ) from the (111) slip plane. (c) Pole figure maps representing the 3D crystallographic orientation of the maximum Feret diameter of the θ precipitates. The legend represents the number of precipitates.

3.3.3 3D Orientation Information

Another important advancement in this work is the correlation of Nanotomography and Electron backscatter diffraction (EBSD) data to obtain 3D crystallographic orientation information (Methods). For the primary aging condition (400 ^{o}C, 20 min), the orientation of the maximum Feret diameter of the precipitates obtained in three-dimensional crystallographic space using Avizo® was utilized to construct stereographic pole figure maps (Figure 24). This novel approach furthered our understanding of the preferred orientation that these elongated θ precipitates possess in 3D. It is evident from Figure 24(c) of the (100) pole figure map that the θ phase primarily tends to be oriented along the <100> cubic axes of the α Al matrix.

After transforming the coordinate axes of the 3D dataset, it was also possible to re-section the virtual microstructure on any particular crystallographic plane using Avizo®. Deformation in metallic systems primarily occurs through slip on specific planes and hence, determining the distribution of precipitates on these planes can play a pivotal role in understanding mechanical properties of the alloy. Due to its highly overaged condition, Orowan looping and formation of dislocation cell structures are the primary modes of mechanical deformation in this alloy. The version of the Orowan equation (Jian Feng Nie, Muddle, and Polmear 1996; Orowan 1948b) which has been used to describe strengthening ($\Delta\tau_p$) caused by shear-resistant particles is given by

$$\Delta\tau_p = \frac{Gb}{2\pi\lambda\sqrt{(1-\nu)}} ln\left(\frac{D_p}{r_o}\right) \quad (2)$$

where G is the shear modulus of the aluminum matrix (25 GPa), v is Poisson's ratio (v=1/3), λ is the planar inter-particle spacing, D_p is mean planar particle diameter, r_o is the outer cut-off radius for matrix dislocations (r_o=b) and b is the magnitude of the burgers vector of these dislocations (b= 0.286 nm). It was possible to determine the wide range of inter-particle spacings on all (111) planes of the segmented microstructure, which has been represented as a frequency distribution in Figure 25(a). This is crucial because up until now, mathematical simplifications were used to compute a single effective value of inter-particle spacing λ_{eff}, for non-spherical distributions (Jian Feng Nie, Muddle, and Polmear 1996) and using this value for strength estimation would be a gross misrepresentation. The version of the Orowan equation that uses λ_{eff} to describe strengthening caused by $<100>_{\alpha}$ rods (J. F. Nie and Muddle 1998), which is applicable in the current case, is given by

$$\Delta\tau_p = \frac{Gb}{2\pi\sqrt{(1-v)}}\left\{\frac{1}{\left(1.075\sqrt{0.433\pi/f}-\sqrt{1.732}\right)d_t}\right\} ln\left(\frac{\sqrt{1.732}\, d_t}{r_o}\right) \quad (3)$$

where f is the volume fraction of the strengthening phase and d_t is the mean diameter of the rods. This equation, however, can be quite misleading, as in the current scenario due to multiple modes of deformation operating. Previous studies on this system have shown Orowan looping to be operative at inter-particle spacings below 0.5 μm, beyond which the self-trapping tendency of dislocations becomes dominant and dislocation cell-structures are formed between precipitates (Calabrese and Laird 1974). However, our ability to measure inter-particle spacings and mean diameter D_p of the precipitates on all glide planes (Figure 24) in 3D has allowed experimental estimation of the increment in the

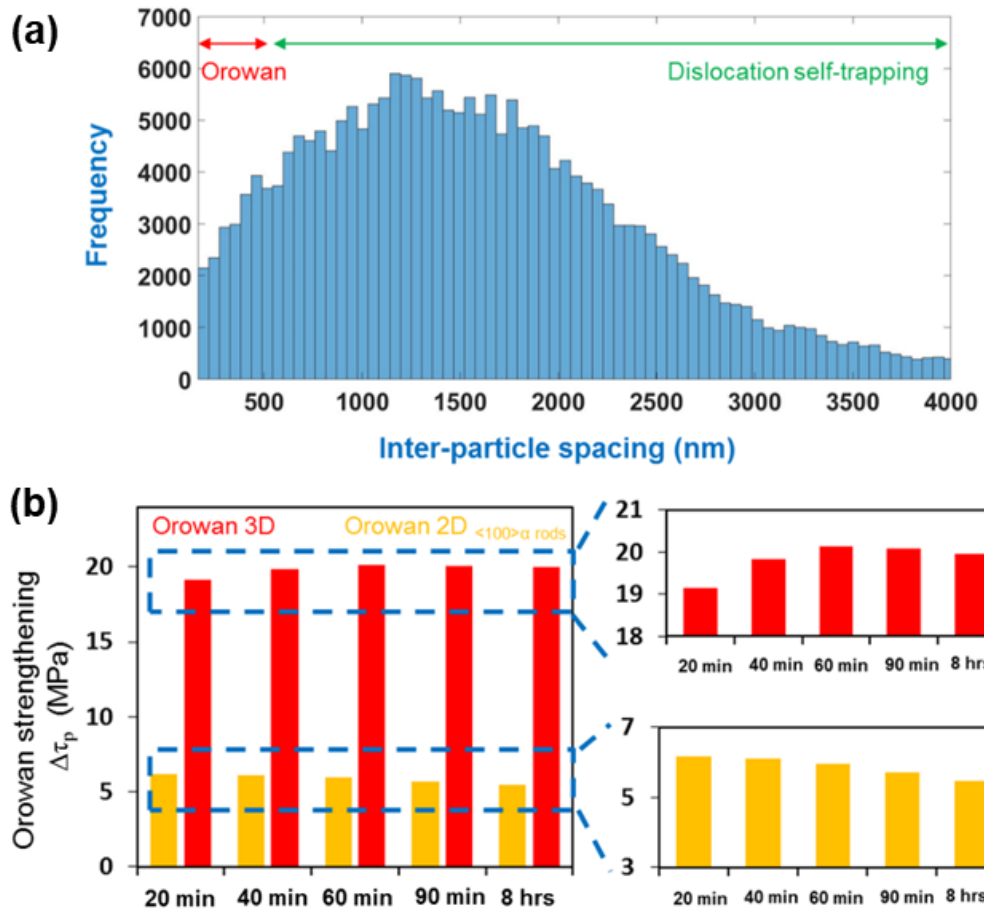

Time	D_p (nm)	λ (nm)	$\Delta\tau_p^{3D}$ (MPa)	f	d_t (nm)	$\Delta\tau_p^{2D<100>\alpha}$ (MPa)
20 min	205.9	478.8	19.15	0.056	500	6.16
40 min	227.2	469.1	19.84	0.064	524	6.12
60 min	219.0	460.0	20.12	0.053	430	5.96
90 min	232.3	465.2	20.07	0.057	438	5.71
8 hrs	223.5	465.0	19.97	0.050	400	5.46

Figure 25: (a) Frequency distribution of interparticle spacings between θ precipitates on all (111) planes of the microstructure. b) Comparison of the increment in CRSS caused by Orowan strengthening ($\Delta\tau_p$) estimated both from 3D data and the 2D analytical model (using Equation (3)), as a function of aging time.

critical resolved shear stress (CRSS) caused by Orowan strengthening ($\Delta\tau_p$), as shown in Figure 25. A comparison has been made with Orowan strengthening values estimated from the 2D analytical model using Equation (3). A stark difference is seen in both the trend as well as the strengthening values.

3.4 Summary

In the present study, synchrotron-based X-ray Nano-CT has been utilized to address and answer some of the most fundamental metallurgical questions pertaining to precipitation-strengthened systems. The morphology, distribution as well as the evolution behavior of θ′ and θ precipitates in an Al-Cu alloy were studied. Aging at 350 ^{o}C revealed complex 3D phase transformation reactions that were occurring in the alloy, most of which are nearly impossible to capture using other characterization techniques. These were coupled with 3D measurements of growth kinetics to gauge a better thermodynamic understanding of the alloy and also measure diffusion co-efficients.

The Nano-CT experiments rendered a more thorough understanding of the coarsening behavior of θ at 400 ^{o}C through 3D measurements. A transition from interface-controlled to volume diffusion controlled growth in thickness was captured from the scaled PSD curves, and a validation of the LSW theory was carried out, for the first time. From these analyses, it can be concluded that broadening in the PSD curves as a result of different factors (such as volume fraction, misfit strain fields, etc.) is often over exemplified. Several rigorous models such as the MLSW theory, the LSEM theory, BW theory, TM theory, MR theory, TK theory, VG theory, etc. (Baldan 2002) have been proposed to

account for shortcomings in the LSW theory. However, none of these models addressed limitations involved in making experimental measurements. This study sets a new paradigm for thermodynamic analysis of precipitate assemblies. Using this approach, new thermodynamic models that incorporate such 3D data at different volume fractions can be formulated to accurately assess the effects of finite volume fraction and quantitatively describe the Ostwald ripening process.

This study also reveals a unique correlative approach that enables bridging tomography data with EBSD, allowing experimental estimation of strengthening modes (such as Orowan strengthening) as well as quantification of the preferred orientation of the θ phase in 3D.

CHAPTER 4

MICROSTRUCTURAL EVOLUTION AND DEFORMATION BEHAVIOR OF AL-CU ALLOYS USING TRANSMISSION X-RAY MICROSCOPY (TXM) AND MICROPILLAR COMPRESSION

4.1 Introduction

The use of precipitation-strengthened aluminum alloys in structural applications is widespread. Thus, a thorough understanding of the microstructure of these materials and its response to mechanical stimuli at the nanoscale is needed. Accurate structure-property linkages are crucial in the development of novel alloy design approaches that aim at improving specific properties such as fracture toughness, fatigue resistance, corrosion resistance, etc. The superb advances in advanced characterization techniques in the past decade have enabled us to explore some of the more fundamental metallurgical concepts with a renewed perspective. It provides a revolutionary means to enhance our microstructural understanding of traditional precipitation-strengthened alloy systems. Bourgeois et al. (Bourgeois et al. 2011) reinstate this point in their recent work, where the authors employ aberration-corrected scanning transmission electron microscopy (STEM) to probe the interfacial atomic structure of θ′ precipitates in an Al-4%Cu alloy and redefine our understanding of its crystal structure. Ma et al. have recently investigated microstructure–property relationships in pre-deformed alloys using TEM studies and also found anomalies in the crystal structure of θ′, where the body-centered position wasn't fully

occupied by Cu atoms (Ma et al. 2016). Similarly, Li et al. conducted *in situ* TEM nano-mechanical testing on miniaturized Al-Cu samples to reveal size-dependent hardening caused by θ′ precipitates (Li et al. 2017). From a modeling viewpoint, Vaithyanathan et al. were successful in simulating the evolution and equilibrium morphology of θ′ precipitates using multiscale modeling (Vaithyanathan, Wolverton, and Chen 2004). These studies also allude to the fact that our understanding of aluminum alloys is far from complete.

Nanoscale precipitates in aluminum alloys tend to exist as rationally oriented particles having complex shapes, depending on the alloy's composition. Their distribution morphology is also known to be strongly dependent on the alloy's thermo-mechanical processing history (Hassan, Bataineh, and Abed 2008; Lumley, Polmear, and Morton 2003). We restrict our discussion here to the classic binary Al-Cu system as it is one of the most thoroughly studied precipitation-strengthened alloys (Boyd and Nicholson 1971; Kang and Laird 1975; Laird and Aaronson 1966; Merle and Fouquet 1981). The sequence of precipitation in these alloys begins with the formation of metastable coherent Guinier-Preston (GP) Zones (Yoshida, Cockayne, and Whelan 2006), which eventually transform into the θ′ phase. θ′ precipitates are plate shaped, semi-coherent second phase intermetallic particles that are the primary strengthening components in these alloys. They possess a fixed stoichiometry (Al_2Cu), coherent broad faces and also have a well-defined orientation relationship with the α matrix ($(001)_{\theta'} \parallel \{001\}_{Al}$) (Laird and Aaronson 1966). Further aging results in the formation of the incoherent equilibrium θ phase. More detailed information on the microstructure of these precipitates can be found elsewhere (Bourgeois et al. 2011; Guinier 1938; Preston 1940).

Conventional understanding of the mechanical behavior in precipitation-strengthened alloys stems from Friedel's seminal study (Friedel 1964) on the transition in deformation response of precipitates as a function of their size. This led to an enhanced understanding of slip behavior (Blankenship, Hornbogen, and Starke 1993) and strain distribution (Hornbogen and Zum Gahr 1975) in aluminum alloys containing spherical particles. Eventually, more sophisticated models using simulations were developed (Zhu, Csontos, and Starke 1999; Zhu and Starke 1999) to overcome the shortcomings of the assumptions in Friedel's model and accordingly, account for factors such as different precipitate morphologies and their finite size. However, an experimentally-driven comprehensive model that accounts for the precipitate's complex 3D morphology is still lacking. The heterogeneity of plastic deformation in such alloys further introduces complications in predicting the alloy's mechanical response. Traditional studies have shown that several interaction mechanisms exist between precipitates and dislocations in such systems (Ardell 1985). In case of aluminum alloys, shearable GP zones show strengthening by means of interfacial and order strengthening (J. F. Nie and Muddle 1998). Whereas, the θ′ phase is largely considered to be shear-resistant on account of its high theoretical shear strength (Pattnaik and Lawley 1971) and hence, contributes to strengthening via the Orowan mechanism (Orowan 1948a), along with the θ phase. Although, Teixeira et al. (Da Costa Teixeira et al. 2008) have been able to show that below a critical thickness of 5.6 nm, θ′ can display shearing. Recent work by Nie and Muddle (J. F. Nie and Muddle 2001) has also helped refine our understanding of deformation in aluminum alloys, by showing that a transition in deformation from precipitate shearing to

Orowan looping need not be invoked to explain its strengthening response. It is also a well-known fact that morphology of the precipitates plays a significant role in impeding dislocation motion and strengthening. Nie et al. (J. F. Nie and Muddle 1998) also made significant progress in this direction by accounting for the size, shape and crystallography of shearable and shear-resistant precipitates in aluminum alloys, to compute respective increments in the critical resolved shear stress (CRSS) and established appropriate versions of precipitation strengthening models for these alloys. However, their studies involved extensive stereological analyses to interpret TEM micrographs and deduce the precipitates' complex morphology, which can be quite convoluted due to the 2D nature of characterization (Da Costa Teixeira et al. 2008; J.F. Nie and Muddle 2008). The use of an effective value of the inter-particle spacing to compute the Orowan stress in their work, can be regarded as an oversimplification of a rather complex problem (C. Shashank Kaira et al. 2017). For these reasons, it becomes very important to visualize and quantify the spatial distribution of precipitates in three-dimensions. With the aid of such accurate 3D morphological data then, these models can be validated and refined accordingly.

Advances in X-ray Microscopy in the last decade (De Andrade et al. 2016; Gorelick et al. 2011) have enabled computed tomography to be performed at the nanoscale. It's an excellent technique to gain insights into phenomena occurring *in situ* at the nanoscale. Several studies have utilized this technique in the recent past to better understand the 3D microstructure of different materials such as metallic alloys (Chandrashekara S Kaira et al. 2016), sodium-ion batteries (Wang et al. 2015), biological materials (Sakdinawat and Attwood 2010), etc. Absorption contrast imaging using synchrotron-based Full-field

Transmission X-ray Microscopy (TXM) allows non-destructive three-dimensional nanoscale characterization of the microstructure, at unprecedented spatial resolutions, as a function of time (4D characterization). The large depth of field associated with the technique allows analysis of huge volumes of material and enables the extraction of a wealth of statistical information. This technique has been recently used by the authors (C. Shashank Kaira et al. 2017) in probing novel 3D microstructural transformation reactions and understanding the coarsening mechanisms in Al-Cu alloys. However, a systematic correlation between 3D microstructural evolution and the alloy's mechanical properties has yet to be conducted. The ability to perform uniaxial compression on micrometer-sized volumes of material has made micropillar compression a widely used technique in the micro-mechanical testing domain (Byer et al. 2010; Greer, Oliver, and Nix 2005; C. Shashank Kaira et al. 2016; A. S. Schneider et al. 2009). The popularity of the focused ion beam (FIB) has made it increasingly possible to routinely carry out such experiments. This study aims to use a novel comprehensive multimodal approach to model the observed micromechanical behavior of Al-Cu alloys (from small-scale testing) by using 3D TXM data, coupled with Electron Backscatter Diffraction (EBSD) and post-deformation TEM analysis. This unique state-of-the-art approach would further our understanding of structure-property correlation in these alloys by linking their *in situ* deformation behavior to their non-destructively characterized nanoscale 3D microstructure.

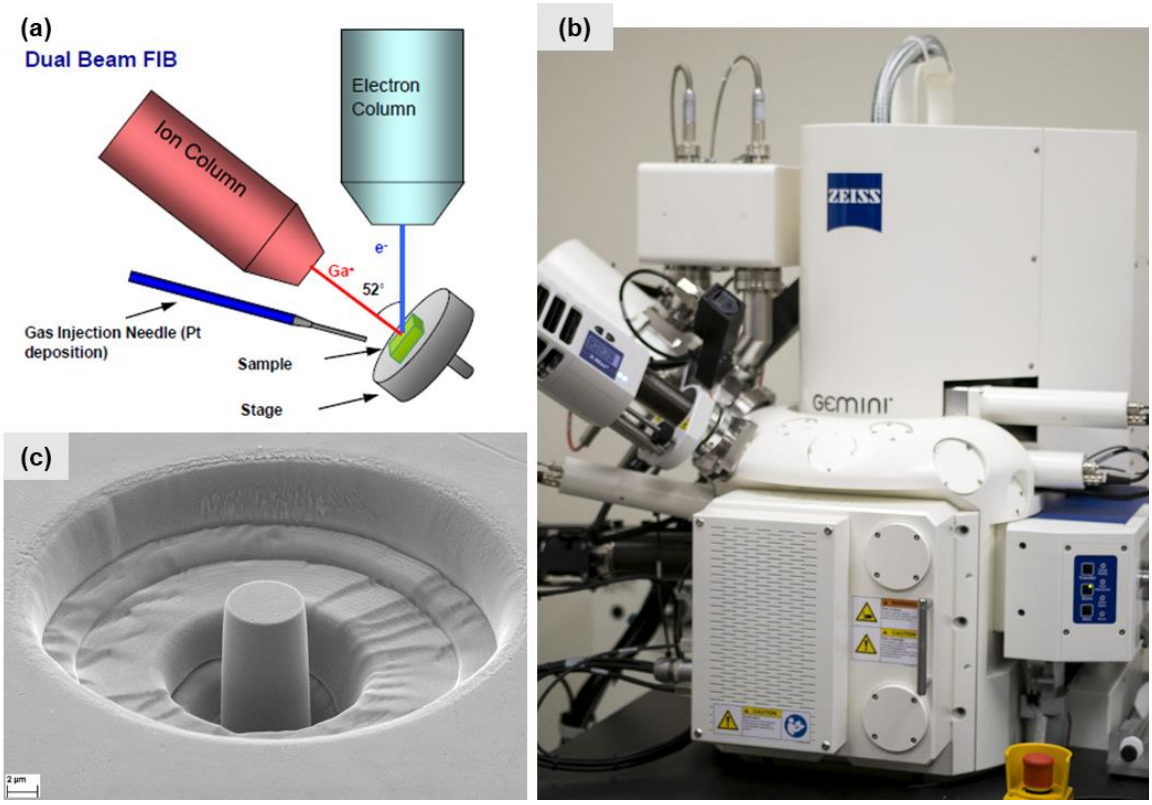

Figure 26: (a) Schematic showing a focused ion beam's principle of operation. (b) Zeiss Auriga FIB Instrument setup. (c) SEM image showing a pure aluminum micropillar fabricated using the FIB.

4.2 Materials and Experimental Procedure

Al-4wt.%Cu wires of 5N purity having a 0.5 mm diameter (Princeton Scientific Corp., Easton, PA, USA) were mechanically sharpened to fine tips. These wires were solution treated at 535 ^{o}C, followed by immediate quenching in ice water and subsequently aged at 350 ^{o}C. A relatively high aging temperature was chosen so as to spatially resolve all the precipitates present in the given volume using Transmission X-ray Microscopy (TXM).

Several authors have also focused on studying the deformation behavior of coarse precipitates (length >500 nm) (Calabrese and Laird 1974; B. A. Chen et al. 2013; Russell and Ashby 1970), so as to better understand the monotonic and cyclic response of aged alloys. Absorption full-field Transmission X-ray Microscopy (TXM) was performed at sector 32-ID-C of the Advanced Photon Source (APS). Due to the instrument's limited depth of field, micropillars roughly 20 μm in diameter and 40 μm in length were fabricated at the tips of sharpened wires using a dual-beam Zeiss® Auriga focused ion beam (FIB) workstation (Figure 26). A Ga^+ ion beam, at an accelerating voltage of 30 keV, was used at a range of currents, starting with 16 nA to mill out a coarse pattern, followed by final milling at 4 nA and 1 nA, respectively, to minimize taper. Imaging was performed at the TXM using a monochromatic beam at 9.1 keV, just above the Cu *K*-edge to maximize the contrast between the Al_2Cu and Al phases. Using an ultra-stable stage design, the amplitude of mechanical vibrations was reduced to about 4 nm (RMS) and it was possible to extract a spatial resolution of sub-60 nm from the TXM (with a voxel width of 16 nm). A more detailed description of the stage design (De Andrade et al. 2016) has been addressed elsewhere. Tomograms were obtained at aging intervals of 45 min (for 6 time steps) and their 3D reconstructions were performed using Tomopy, an open source Python based toolbox used to analyze synchrotron tomography data (De Carlo et al. 2014; Dogˇa Gürsoy et al. 2014). Subsequent 3D segmentation, quantification as well as visualization was carried out in Avizo® Fire. Each analyzed volume was comprised of over a thousand precipitates.

For post-scanning analysis using EBSD, the tips of the samples were cross-sectioned using the FIB at an accelerating voltage of 30 keV and using a current of 1 nA. EBSD was performed on these flat sections, using a step size of 0.5 μm to identify the grain orientation of the α-Al matrix. TSL® OIM data collection and analysis software was used to analyze the acquired EBSD data.

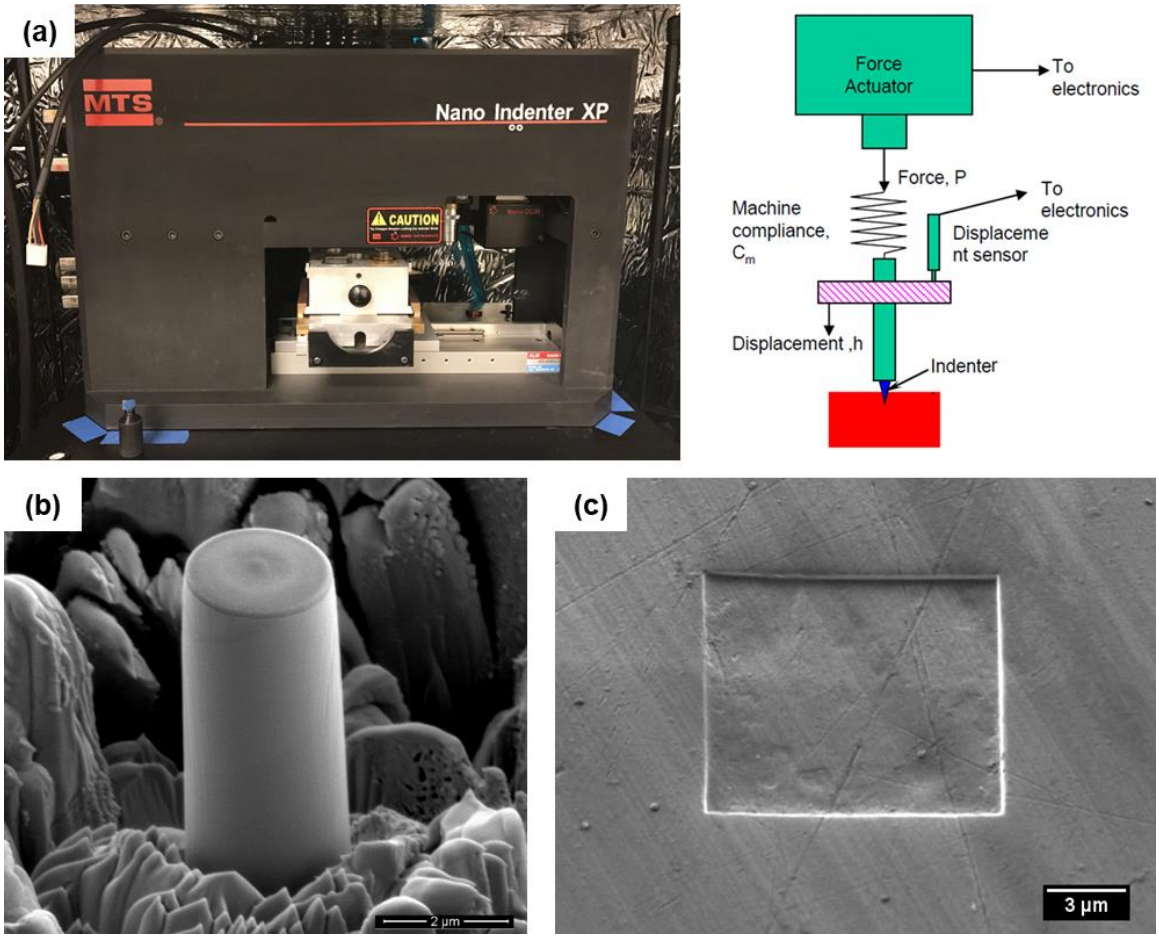

Figure 27: (a) Nanoindenter instrument setup and its principle of operation. Uniaxial compression tests can be performed on (b) Micropillars using a (c) flat punch.

Al-4wt.%Cu wire samples were mounted and polished flat metallographically up to a 0.05 µm colloidal silica finish and subsequently used for microscale testing. These samples were solution treated for long times to ensure large grain sizes, so as to eliminate any heterogeneity arising from crystallographic orientation. The micromechanical testing route included fabrication of micropillars (4 µm x 12 µm) on a particular grain, uniaxial compression of these pillars followed by heating the sample at 350 ^{o}C to resume the aging process and repeat the above procedure for different aging times. This was performed to obtain the variation in stress-strain response for different aging times. A Ga^{+} ion beam, at an accelerating voltage of 30 keV, was used at a range of currents, starting with 16 nA to mill out a trench to provide clearance for the nanoindenter's flat punch tip (Figure 27(c)), leaving behind a coarse pillar of about 10 µm in diameter. The size of the coarse pillar was then reduced using currents of 4 nA and 1 nA. Subsequent final thinning was performed at 0.1 nA. The final milling step using a fine current ensured the minimization of taper ($<2^{o}$) and also minimized the damage that could prevail from the use of the Ga^{+} ion beam. A thin layer of platinum deposited using EBID (Electron beam-induced deposition) prior to milling also ensured minimization of taper and rounding at the micropillar's top surface. The size of the pillars were intentionally chosen to be quite large, so as to avoid any effects of Ga^{+} damage on mechanical properties, caused due to FIB milling. It was also ensured that the size of the pillars chosen were representative of the bulk microstructure. Fabrication using the annular milling technique ensured Ga^{+} ion impact with only grazing incidence. The size of the damage layer on either side was quantified using a TEM specimen of a micropillar's cross-section, as shown in Figure 28(b). This damaged

amorphous layer at the surface was found to be relatively small (~8 nm). Accounting for the size of the micropillars, it can be safely concluded that the damage layer from grazing incidence of the Ga^+ beam will have minimal impact on the mechanical properties measured using micropillar compression (Kiener et al. 2007; Shim et al. 2009). Xiao et al.'s recent study (Xiao et al. 2017) on comparing the effects of FIB milling (using Ga and Xe ions) on the micro-mechanical properties of aluminum also supports this fact, where they observed negligible effects on the yield strength in case of single crystalline aluminum, as compared to significant differences in stress measurements as well as the deformation morphology for ultrafine-grained aluminum samples.

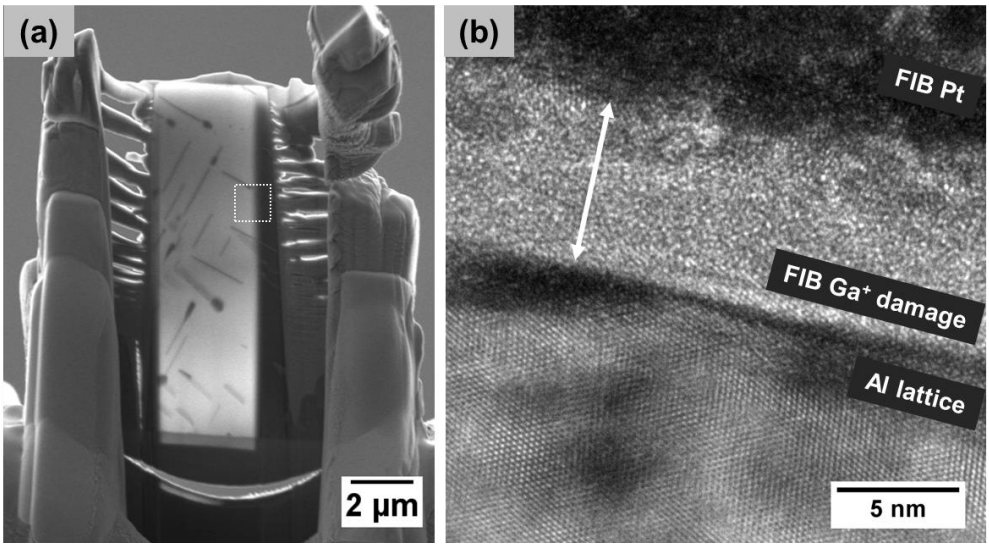

Figure 28: (a) TEM sample showing the cross-section of a representative micropillar at the initial aging condition (t= 45 min), compressed to its yield point. (b) TEM micrograph showing the thickness of the damaged amorphous layer (~8 nm) at the micropillar's surface, due to grazing incidence of the Ga^+ beam.

Micropillar compression was performed using a Nanoindenter (XP, Agilent Technologies, AZ) (Figure 27) using a diamond indenter tip (Micromaterials, Wrexham, UK) with a flat square cross-section (10 µm x10 µm). A cyanoacrylate based adhesive was used to mount the sample onto an aluminum stub. A constant displacement rate of 7 nm/s was used to maintain a nominal strain rate of ~10^{-3} s^{-1}. The experiments were initiated when the thermal drift fluctuations reduced to a value below 0.05 nm/s. The top diameter of the micropillars was used for the calculation of stress. The post-deformed pillars were analyzed at a 35^{o} tilt using scanning electron microscopy (SEM).

To observe the interaction of dislocations with the nanoscale precipitates, a TEM sample was prepared using the standard FIB lift-out technique. Representative micropillars at the initial aging condition (t= 45 min) that were compressed to the yield point as well as completely deformed, were used for this purpose. TEM investigation was performed in an aberration-corrected FEI 80-300 Titan™ operated at 300 kV. NanoFlip, an *in situ* Nanoindenter (Nanomechanics, Inc., Knoxville, Tennessee) was installed in the dual-beam Zeiss® Auriga focused ion beam (FIB) workstation to carry out *in situ* micropillar compression.

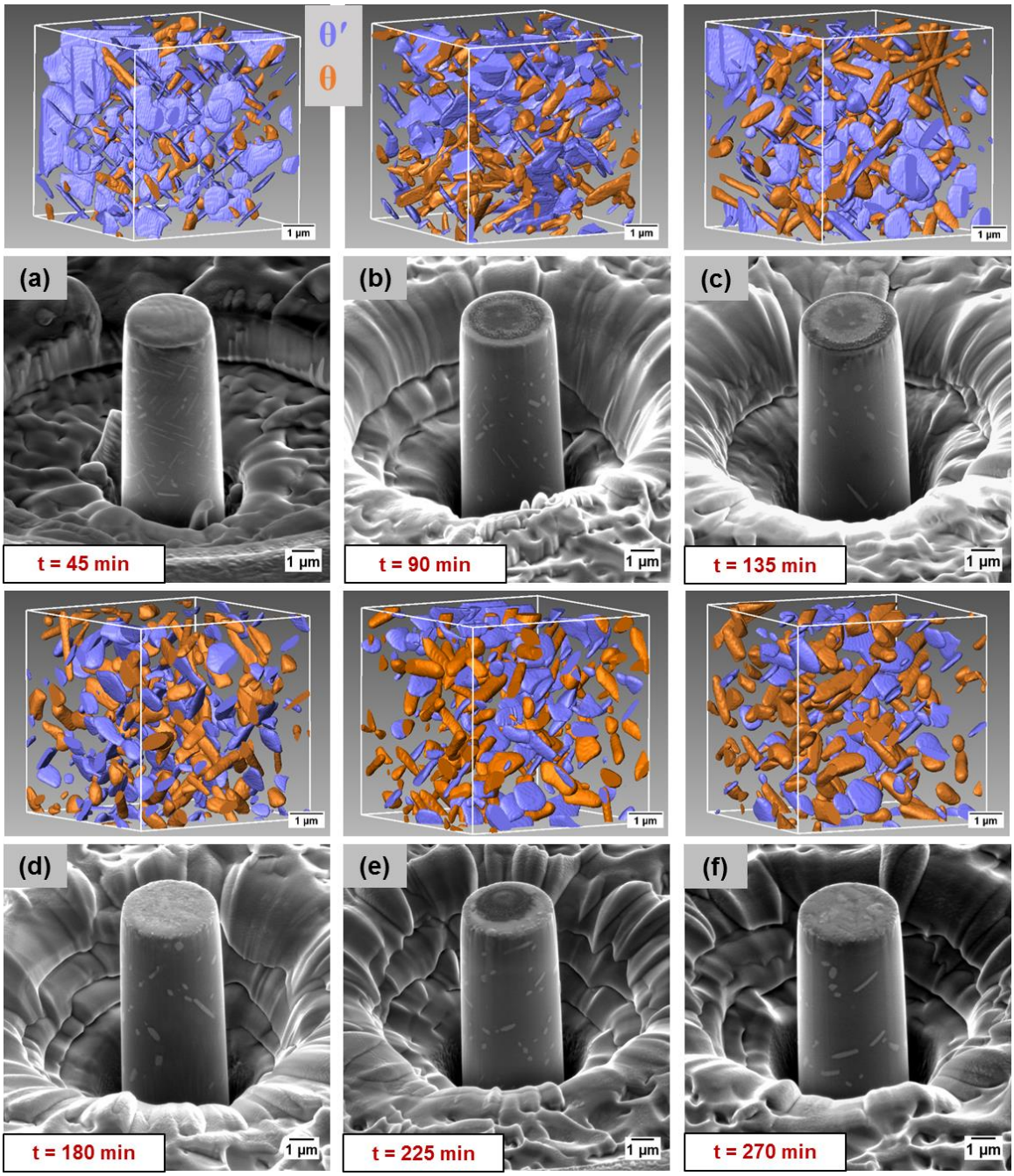

Figure 29: SEM images showing representative micropillars fabricated in a single grain at different aging times (T = 350 ºC). Corresponding 3D rendition of the microstructure from TXM for each aging condition has also been displayed.

4.3 Results and Discussion

4.3.1 4D Nanoscale Microstructural Evolution

Variation in the Al-4%Cu alloy's microstructure is evident from the surface of the micropillars shown in Figure 29. As they were fabricated at different aging times, these single-crystal micropillars share the same crystallographic orientation. Any effects of microstructural variability at each time step can thus be neglected. A different region of the same Al-4%Cu sample (used for micromechanical testing) was probed using transmission X-ray microscopy and the corresponding 3D rendition of a single evolving microstructure has been included adjacent to each micropillar for visualization purposes (Figure 29). From multiple scans performed using the TXM, it can be safely concluded that the microstructure across the sample was quite homogeneous and hence, was indeed representative of the bulk. The change in volume fraction of the individual phases, has been quantified and captured accurately in Figure 30. The 3D visualization of the microstructure highlights how such transformation reactions can affect the mechanical properties of the alloy. Nucleation and growth of the θ phase, at the expense of θ′ precipitates causes the latter to dissolve and break up into sub-structures. This alters the respective precipitate density in the alloy, as well as the total interfacial surface area of each individual phase, which can have important implications on dislocation trapping and failure initiation. The overall 3D morphology of the precipitate distribution is also seen to change significantly.

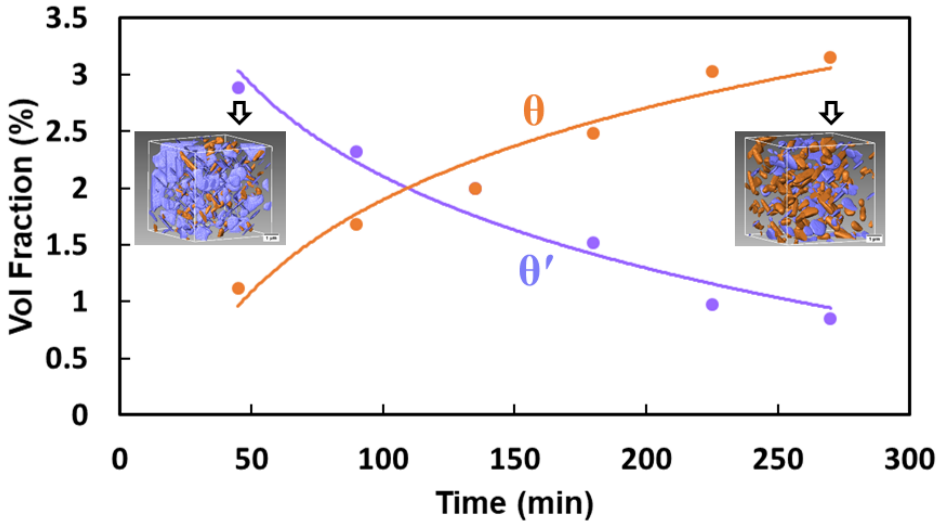

Figure 30: Variation in volume fraction of the individual phases (θ′ & θ) as a function of aging time (T = 350 ºC).

4.3.2 Transition in Deformation Behavior upon Aging using Micropillar Compression

At each aging condition, four micropillars were fabricated and tested (summing up to a total of 24 micropillars), to provide statistically relevant mechanical data. The onset of plasticity in case of micropillars can be quite a stochastic process and hence, a larger number of tests can help reduce uncertainty in determining the yield stress (Figure 31). Compression of these micropillars (shown in Figure 29) yielded stress-strain curves that were marked by numerous strain bursts. A representative stress-strain curve has been shown in Figure 32. Initial plasticity is marked by small such bursts which correspond to either local avalanches of groups of dislocations or shearing of individual θ′ precipitates, while the larger bursts correspond to slip bands propagating through the volume of the

micropillar. These bursts can have different origins in different materials. Although in this study, this was corroborated by *in situ* micropillar compression experiments, which enabled direct correlation of stress-strain data (Figure 35) with live shearing events occurring during deformation of the micropillar. Similar micropillar compression experiments were performed on 99.999% pure Al samples (Princeton Scientific Corp., Easton, PA, USA), to serve as a comparison and to "back out" the effect of the Al matrix on the deformation behavior. The fracture behavior of these single-crystalline micropillars was found to be significantly different, where a few large strain bursts occurred (corresponding to shear bands causing fine slip in the micropillar) with minimal strain hardening (Figure 32(b)).

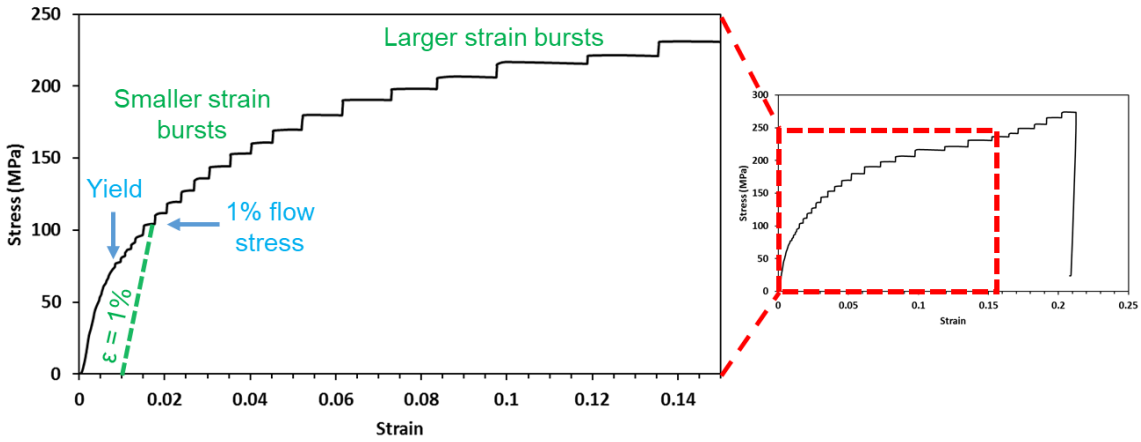

Figure 31: Representative stress-strain curve obtained from uniaxial compression testing of such micro-volumes in an Al-4%Cu alloy (t= 45 min).

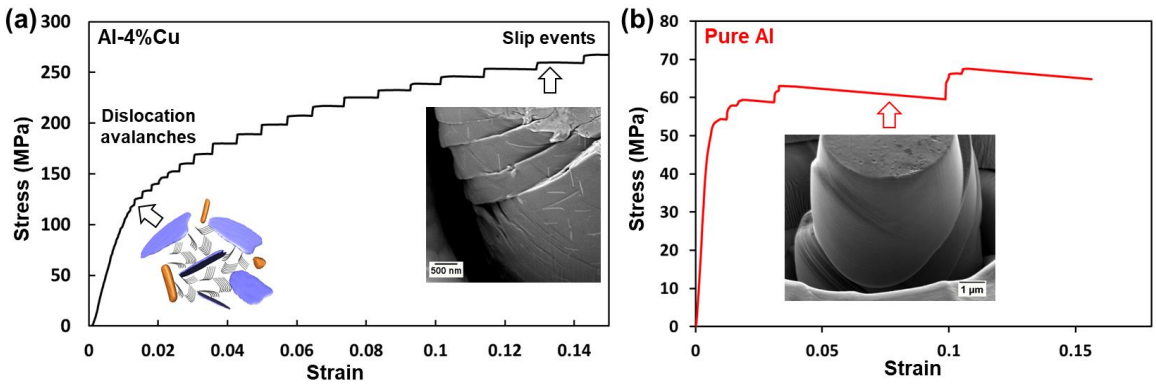

Figure 32: Engineering stress-strain curves obtained from uniaxial compression of micropillars on (a) an Al-4%Cu alloy (aged to T=350 ^{o}C and t= 45 min) and (b) Pure Al.

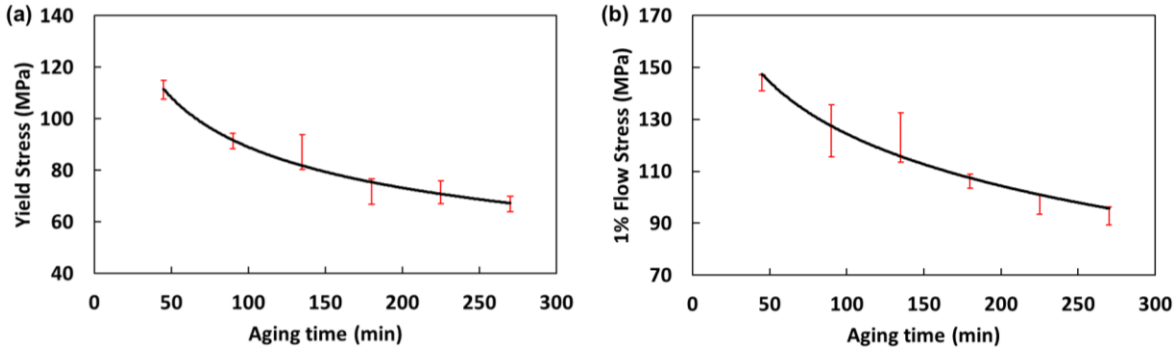

Figure 33: Variation in Yield stress and 1% Flow stress as quantified from micropillar compression for Al-4%Cu (T=350 ^{o}C).

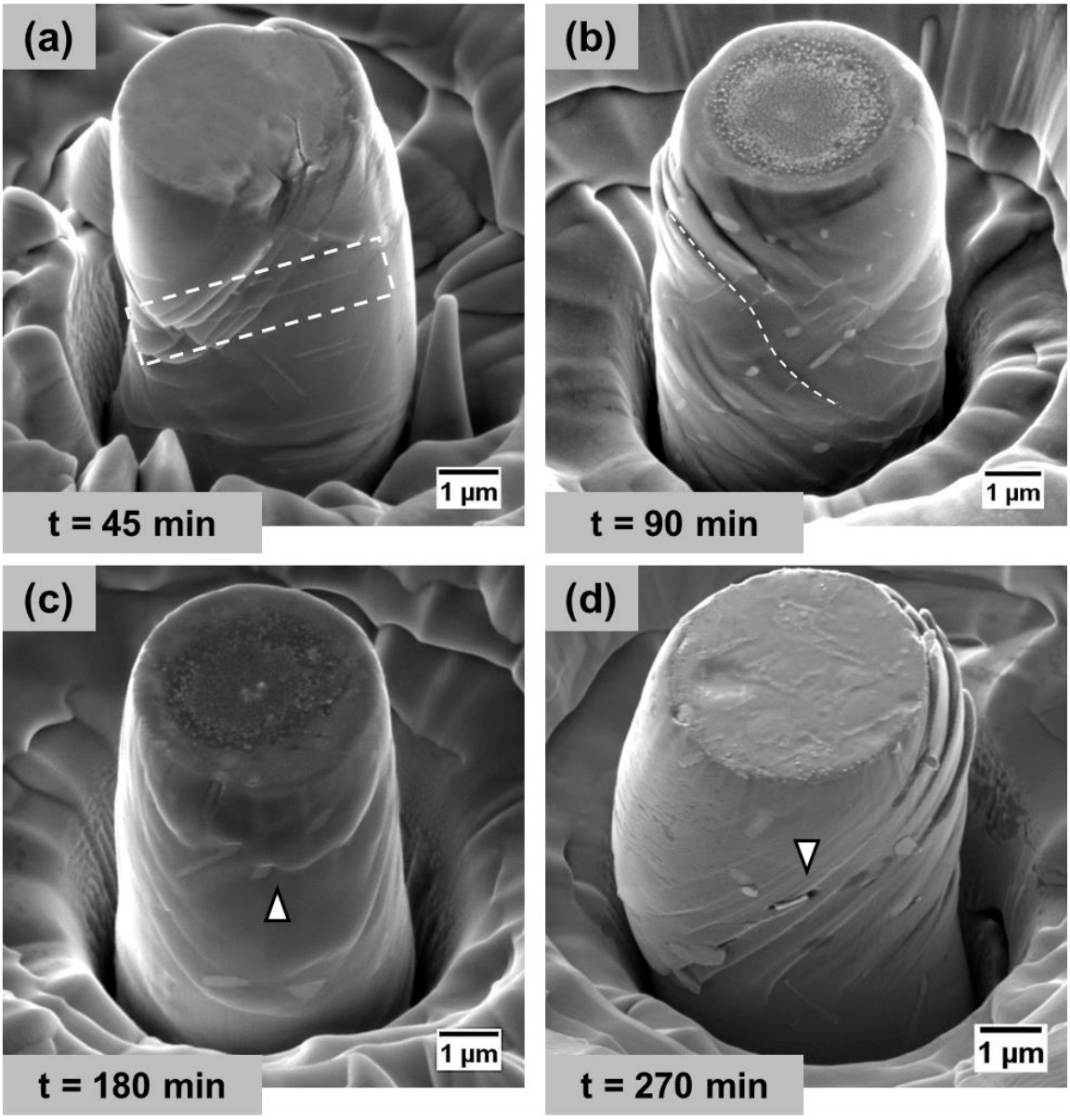

Figure 34: Post-compression SEM micrographs of representative micropillars at aging times (a) t= 45 min, (b) t= 90 min, (c) t= 180 min and (d) t= 270 min.

After the onset of plasticity, the deformation behavior transitions significantly as a function of aging time. Strain bursts in the stress-strain curves correspond to shearing events at initial aging conditions. Upon aging, these bursts correspond mainly to dislocation avalanches between shear-resistant θ precipitates. Figure 34(a) clearly depicts multiple slip bands shearing an individual θ′ precipitate, as seen from the surface of the micropillar. Transition from planar slip to wavy slip is seen at t= 90 min (Figure 34(b)). As the volume fraction of shear-resistant θ gradually increases, the propensity to cross-slip in Al alloys promotes deformation through wavy slip. A stark transition is seen at later aging conditions, where the soft Al matrix plastically flows around the shear-resistant θ precipitates (t= 180 min, Figure 34(c)). At t= 270 min (Figure 34(d)), voids are seen to form at the interfaces of θ precipitates as a result of severe strain incompatibilities resulting in interfacial failure.

This transition in deformation behavior has also been clearly captured using *in situ* micropillar compression. For the *in situ* tests, micropillars were fabricated at the sample's edge (with perpendicular faces polished) (Figure 35(a)) on separate samples for the initial (t= 45 min) and final (t= 270 min) aging conditions, to allow clear viewing of the indentation process. At the initial aging condition, Figure 36(a) shows the sudden initiation and propagation of slip bands through the micropillar, shearing a couple of θ′ precipitates on its path, as visible from the micropillar's surface.

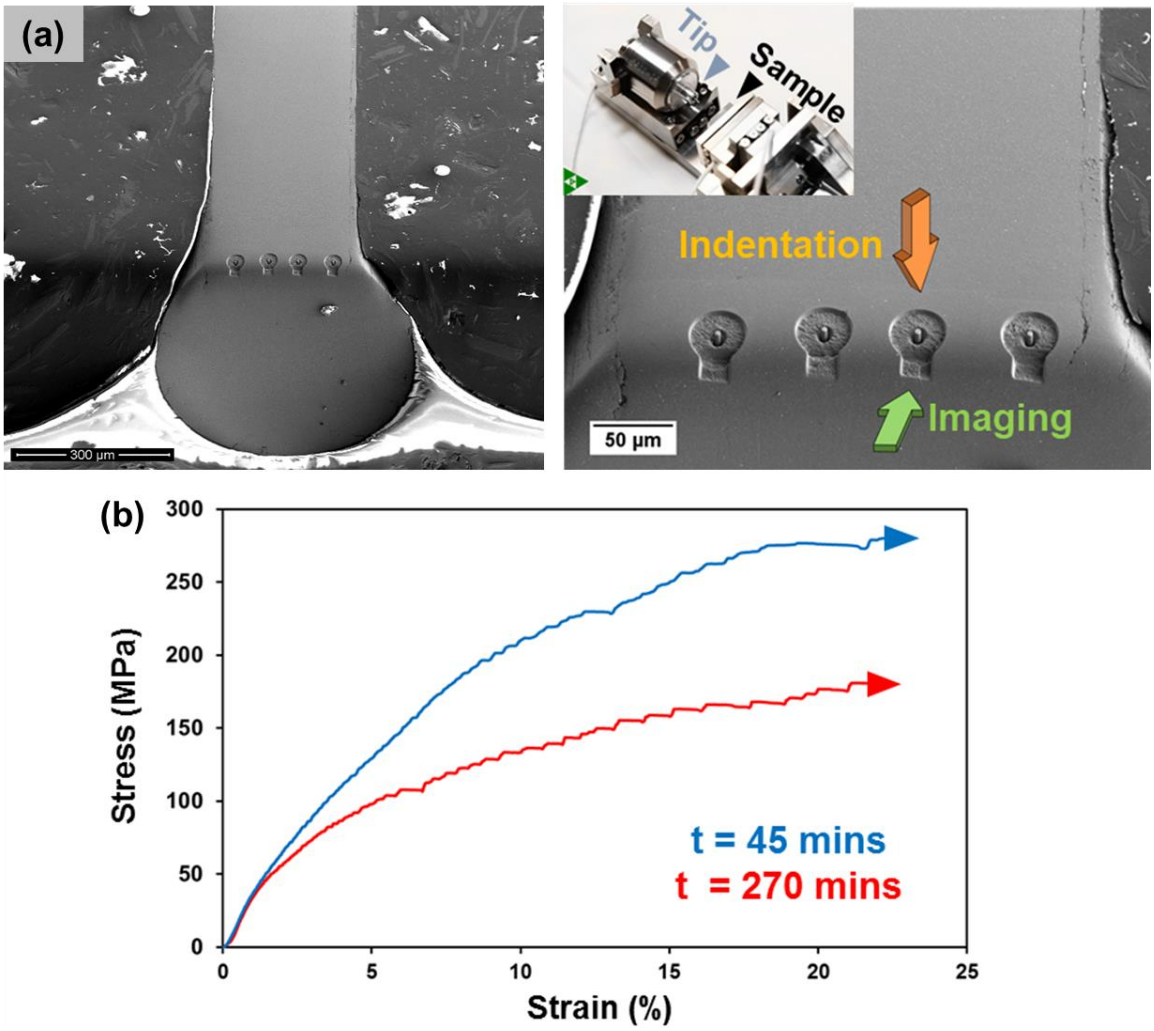

Figure 35: (a) SEM images showing micropillars fabricated at the edge of a sample with polished perpendicular faces. Inset showing the *in situ* indenter NanoFlip's setup. (b) Representative engineering stress-strain curves recorded during *in situ* micropillar compression testing.

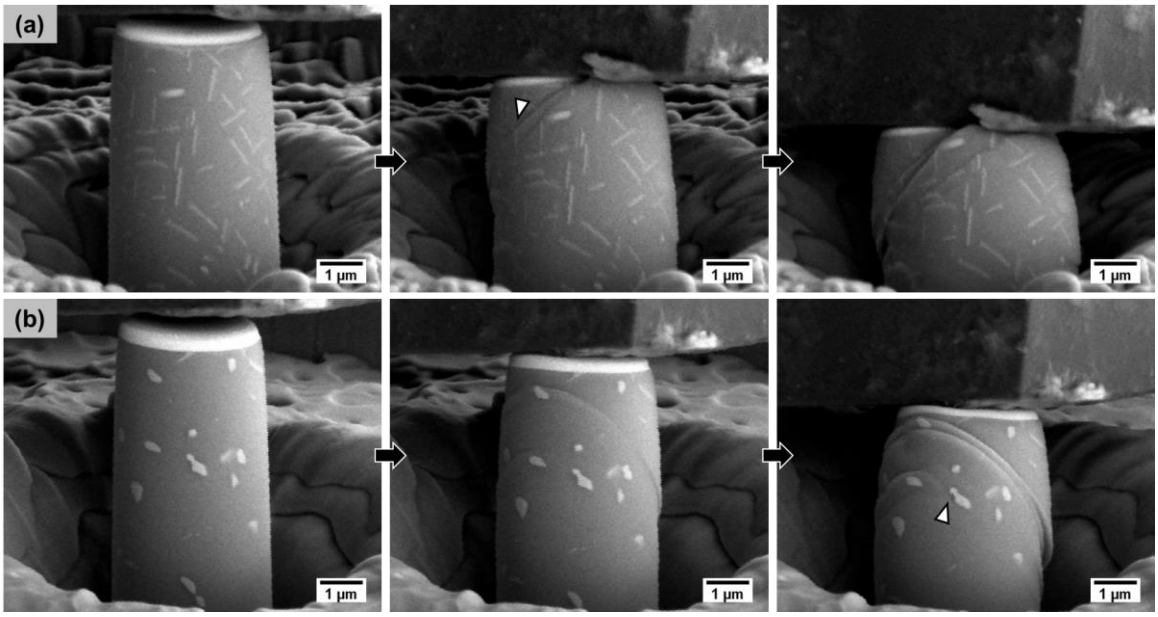

Figure 36: (a) Stills from video showing *in situ* uniaxial compression of a micropillar aged to t= 45 min, where a sheared θ′ precipitate has been indicated. (b) Stills from video showing *in situ* uniaxial compression of a micropillar aged to t= 270 min, where the arrow indicates an arrested slip band at the θ interface.

This suggests that once the internal stresses are high enough, the onset of failure can be instantaneous, causing slip to propagate even through thick θ′ precipitates (thickness >60nm). Whereas for the overaged condition, Figure 36(b) shows much smoother deformation in the micropillar. The primary slip bands can be seen avoiding interaction with the shear-resistant θ precipitates, while a few are also impeded at the interfaces of such particles, leading to interfacial de-bonding. The overall reduction in strain hardening (as a result of aging) has also been clearly captured in the stress-strain curves shown in Figure 35(b) (recorded during in *in situ* micropillar compression testing). A reduction in

isotropic hardening is expected as a result of the decrease in the ability of precipitates to store dislocations, due to the decreasing volume fraction of θ′. We can also expect a decrease in kinematic hardening due to a change in the overall morphology of the precipitates.

It is also very interesting to note that although the θ′ precipitates are significantly thick (>60 nm), they are seen to be sheared during micropillar compression (Figure 34(a)). This is quite unconventional as the θ′ phase (Al_2Cu) is considered to be highly shear-resistant, with very high theoretical shear strength values, on the order of GPa (da Costa Teixeira et al. 2009). This also suggests that locally very stresses can be attained in such microstructures. Another interesting point to note is that it could be potentially possible that the thickness of a θ′ precipitate determines its ability to store a large density of dislocations, irrespective of its size.

4.3.3 Modeling the Variation in Yield Strength using 3D TXM data

Although deformation behavior of Al-Cu alloys has been investigated in detail by several authors in the recent past (Calabrese and Laird 1974; da Costa Teixeira et al. 2009; J. F. Nie and Muddle 1998; Russell and Ashby 1970), a fundamental understanding of the precise deformation mechanisms taking place is still missing. This is mainly because conventional modes of characterizing nanoscale features have been either through transmission electron microscopy (J.F. Nie and Muddle 2008), which offers only a sectional view of the specimen, or more recently, atom probe tomography (Ringer and

Hono 2000), which is capable of sampling statistically insufficient volumes. The main drawback of the aforementioned techniques, however, is their destructive nature. It has been really difficult, to-date, to probe evolution of the same microstructure at the nanoscale, non-destructively over time. This opens up the possibility of drawing conclusions from the mechanical properties of miniaturized volumes from a single grain, to a non-destructively characterized 4D microstructure (a 3D microstructure varying with time). It is important to note that volume fraction changes occurring in the evolving microstructure can strongly affect the morphological distribution of precipitates in the microstructure. As the θ′ phase is primarily plate-shaped and exists as three orthogonal variants, its large total surface area allows it to store dislocations to a much greater extent than the θ phase, which is either globular or rod-shaped. As aging progresses, θ′ plates dissolve and the θ phase nucleates and grows, as a result of which, the alloy's yield strength as well as its strain hardenability reduces. Several authors have previously identified the importance of the precipitate distribution's morphology in determining the mechanical properties of aluminum alloys (Muddle and Nie 2006; J. F. Nie and Muddle 1998). However, the models proposed to account for the plate-shaped nature of precipitates in aluminum alloys are either based on idealized microstructures or a stereological interpretation of TEM images and, hence, do not account for the statistical variability and true morphologies associated with 3D distributions.

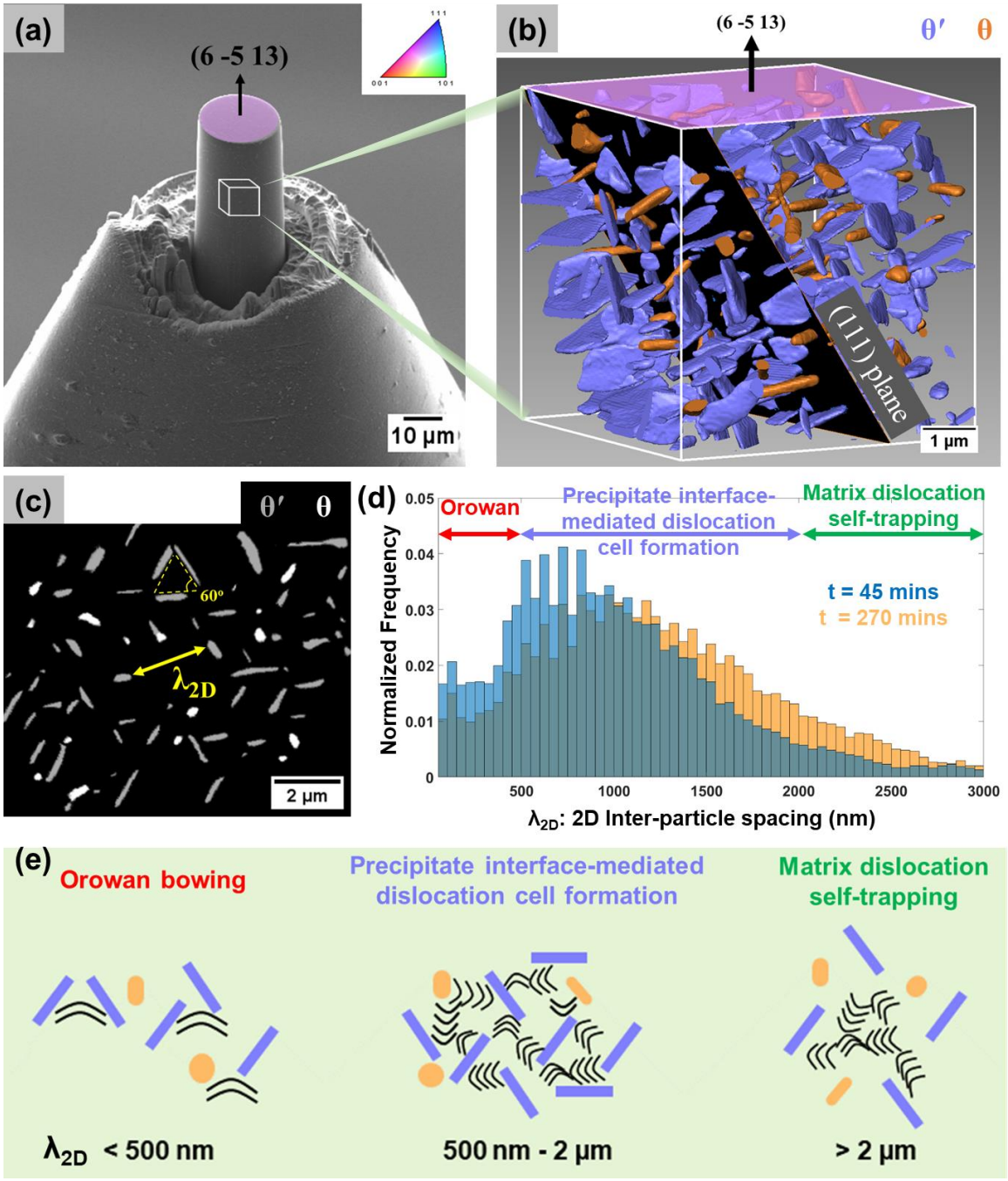

Figure 37: (a) SEM Image of a micropillar fabricated at the tip of an Al-4%Cu alloy needle, for scanning using the TXM. Crystallographic orientation of the α-Al matrix at the pillar's top surface measured using EBSD has been shown. Inset shows the IPF map of Al. (b) Non-destructive 3D visualization of a small volume from within the

micropillar, showing the different phases (θ′ & θ). (c) Virtual re-slicing of the 3D microstructure showing spatial distribution of precipitates on the (111) plane. (d) Normalized histogram showing distribution of 2D inter-particle spacing between adjacent precipitates on all (111) planes and their classification based on dislocation activity. (e) Schematic showing operation of different dislocation-based strengthening modes as a function of λ_{2D}.

Figure 37(b) shows the 3D rendering of a volume from the micropillar shown in Figure 37(a). By determining the crystallographic orientation of the single-crystalline micropillar's Al matrix using EBSD, it was possible to re-section this virtual microstructure along the (111) plane to determine the precipitate distribution on the aforementioned plane using Avizo® Fire. This corresponded to a single crystal as the grain sizes of the sample under study were made intentionally quite large (~400 μm). A representative slice from this re-sliced microstructure has been shown in Figure 37(c). Scripts in commercial MATLAB® software (MathWorks Inc.) were used to compute the minimum planar inter-particle spacing between adjacent precipitates (λ_{2D}), for each slice of the microstructure, by 2D finite body tessellation using Euclidean distance maps. Using the watershed algorithm, the tessellation ensured that each individual precipitate was bounded by a 2D cell (Yazzie et al. 2012), as shown in Figure 38. For a pair of precipitates on a 2D slice, the minimum planar inter-particle spacing was calculated between their respective perimeters. Figure 37(d) shows the histogram of 2D inter-particle spacing between all adjacent precipitates (λ_{2D}) for the initial (t= 45 min) and final aging times (t= 270 min). This

distribution alludes to the complexity of the microstructure and suggests the operation of more than one deformation mechanism. It is also quite important to note that this 2D distribution data for specific planes can only be obtained by virtually re-slicing a 3D microstructure (C. Shashank Kaira et al. 2017).

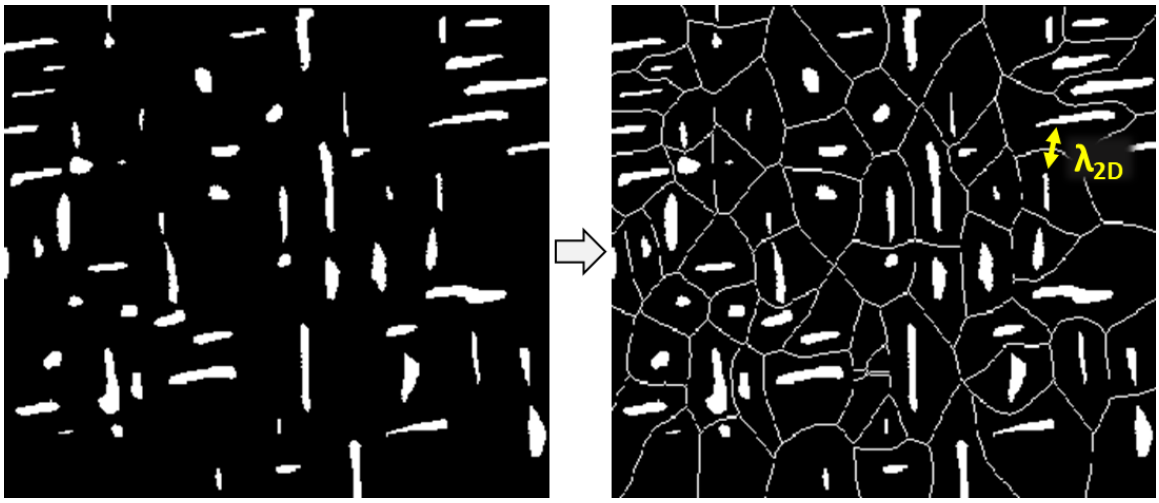

Figure 38: 2D finite body tessellation on binarized 2D TXM slices to compute the inter-particle spacing (λ_{2D}).

The larger size of precipitates present in these aluminum alloys suggest a combination of the following deformation mechanisms: Orowan strengthening, solid solution strengthening, and dislocation cell strengthening. It's also possible to use the 3D microstructural dataset to quantify the relative proportions of each. In regard to this, several important conclusions can be drawn from this histogram of 2D inter-particle spacing between all adjacent precipitates. The Orowan strengthening mechanism is mainly operative only at inter-particle spacings below 500 nm. TEM observations in Calabrese and Laird's study (Calabrese and Laird 1974) on the deformation behavior of coarse θ′ plates (similar to those encountered in this study), support this proposition. Once the inter-particle spacing between precipitates exceeds a certain value (referred to as the self-trapping distance), dislocations tend to interact with one another and form dislocation cells, rather than interact with second-phase precipitates. In a fatigue study conducted by Park et al. (Park et al. 1970), similar observations were made from precipitates spaced apart greater than 500 nm. However, it must be noted that this transition is not very definite and the assumed value is qualitative. Furthermore, it is also important to note that the contributions arising from Orowan strengthening are quite low at inter-particle spacings greater than 500 nm and hence, do not greatly influence the average computed value of the Orowan stress. For inter-particle spacings between 500 nm and 2 μm, precipitate interface-mediated dislocation cell formation plays a dominant role in controlling deformation. Numerous dislocation cells are formed within the matrix and the walls of these cells are defined by the precipitate interfaces (Figure 41). Hence, the precipitates play a pivotal role in determining the dislocation cell size, as also observed in Calabrese & Laird's study

(Calabrese and Laird 1974). However, at larger inter-particle spacings (> 2 μm), mutual interactions between dislocations in the matrix (referred to as matrix dislocation self-trapping) tend to supersede all other interactions and the dislocation cell size is no longer a function of the precipitate morphology. In this fashion, the inter-precipitate spacing histogram (Figure 37(d)) can thus be classified into three domains based on the dominant mode of deformation. The operation of different dislocation-based strengthening modes as a function of λ_{2D} has been depicted in the schematic shown in Figure 37(e).

As the majority of this histogram lies within the second domain, precipitate interface-mediated dislocation cell formation plays the most important role. This is directly influenced by the size, distribution and morphology of the precipitates present. It can also be conjectured that the Orowan mechanism operates only later in the deformation process, when the internal back stresses generated from dislocation pile-up on precipitate interfaces rise significantly (after the onset of plasticity).

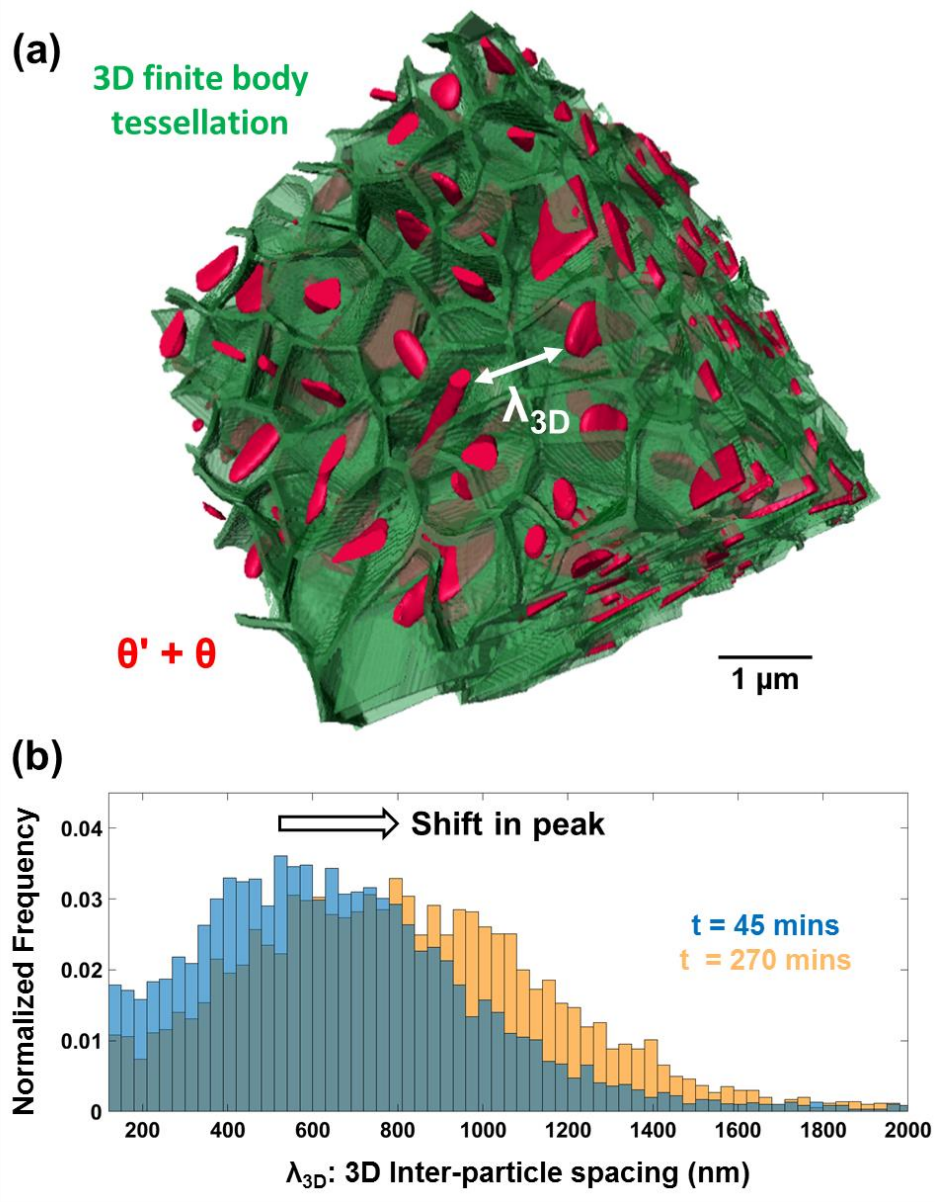

Figure 39: (a) 3D finite body tessellation using Euclidean distance maps on the 3D microstructure (t= 45 min) to compute the inter-particle spacing between adjacent precipitates. (b) Normalized histogram showing distribution of these 3D inter-particle spacing between adjacent precipitates for the initial and final aging conditions.

Using parameters acquired by virtually re-slicing the 3D datasets, an upper bound value for the increase in CRSS from Orowan strengthening can be calculated from (C. Shashank Kaira et al. 2017; Jian Feng Nie, Muddle, and Polmear 1996; Orowan 1948b):

$$\Delta\tau_p = \frac{Gb}{2\pi\lambda_{Mean2D}\sqrt{(1-v)}} ln\left(\frac{D_p}{b}\right) \quad (4)$$

where G is the shear modulus of the aluminum matrix, v is Poisson's ratio, λ_{Mean2D} is the average planar inter-particle spacing obtained from re-slicing the 3D data set (<500 nm), D_p is mean planar particle diameter and b is the magnitude of the burgers vector of dislocations in the matrix. As only contributions from the first domain of the histogram are considered, the upper bound value for increment in CRSS from Orowan strengthening does not vary significantly with aging time and is found to be ~20 MPa. Similarly, it is also possible to quantify the contribution from solid solution strengthening using the Fleischer equation (Fleischer 1993). As the copper dissolved in solution is only 0.6 wt. %, this value is negligible and hence, the effects from solid solution strengthening can be safely ignored. Variation in yield strength is hence primarily dictated by the density of geometrically necessary dislocations (GNDs) and the size dislocation cells formed between precipitates. It is well known that these dislocations can tend to form complex three-dimensional networks intertwined with the precipitates (Calabrese and Laird 1974; Russell and Ashby 1970). Hence, understanding the three-dimensional spatial distribution of θ′ and θ precipitates is crucial in estimating the size of these dislocation cell structures. To accomplish this, similar scripts in MATLAB® (MathWorks Inc.) were used to compute the minimum 3D inter-particle spacing between adjacent precipitates (λ_{3D}), by 3D finite

body tessellation using Euclidean distance maps, as shown in Figure 39(a). Figure 39(b) shows the histogram of 3D inter-particle spacing between all adjacent precipitates (λ_{3D}) for the initial (t= 45 min) and final aging times (t= 270 min). These are evidently quite different from those in Figure 37(d), hence highlighting the need to probe the 3D spatial distribution of precipitates.

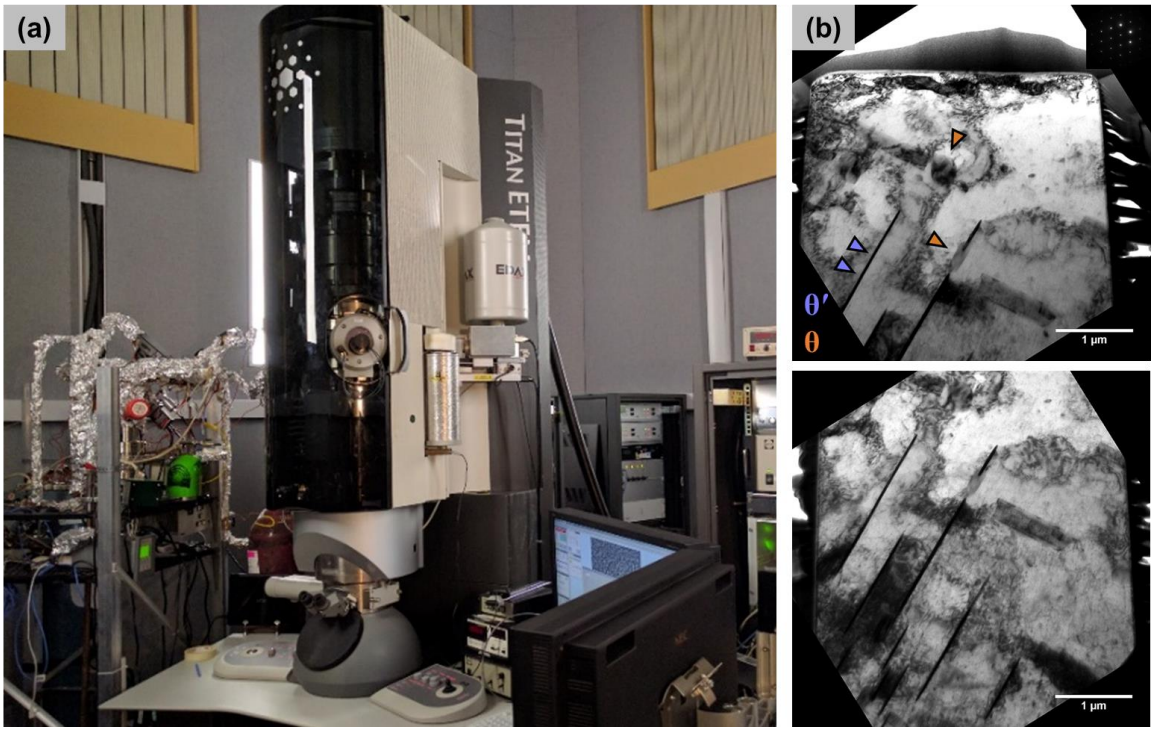

Figure 40: (a) Aberration-corrected TEM (FEI Titan). (b) TEM micrographs showing dislocation storage in a representative micropillar at the initial aging condition (t= 45 min), compressed to its yield point.

Evidence of dislocation storage on the broad faces of plate-like θ′ precipitates can be seen from TEM Images shown in Figure 40(b) and Figure 41. This TEM specimen corresponds to a section of a micropillar (initial aging condition, t= 45 min) compressed to its yield point. Strain contrast from accumulation of dislocations at the interface of θ′ (edge-on view) is visible in Figure 41(c). Russel and Ashby (Russell and Ashby 1970) also found large gradients in shear strain in the vicinity of similar coarse θ′ precipitates by measuring asterism in Laue patterns and using transmission electron microscopy. From their work, it is clear that the local shear strain (γ) at the particle-matrix interface caused by interaction of a slip system from the matrix, is a function of the density of GNDs stored at these interfaces.

This also leads to local lattice rotation in the matrix. Figure 41(d) shows an array of dislocations stored at a θ′ precipitate (face-on view). The dislocation spacing on θ′ precipitates from these TEM micrographs was used to compute the shear strain ($\gamma \sim 0.012$) using the relation $nb = \gamma h$ (Russell and Ashby 1970), where h is the plate height normal to the slip plane. The density of GNDs (ρ^G) trapped by the globular/rod-shaped θ phase can be neglected (for purposes of γ calculation) as it is considerably low and Ashby's work (Ashby 1970) has been able to quantify this. This can also be concluded qualitatively from Brown and Stobbs' work (Brown and Stobbs 1971), relating the plastic strain to the number of dislocation loops stored by such particles. Assuming that there exists a minimum spacing between loops (da Costa Teixeira et al. 2009), the θ phase stores a considerably lower density of GNDs, as a result of their morphology.

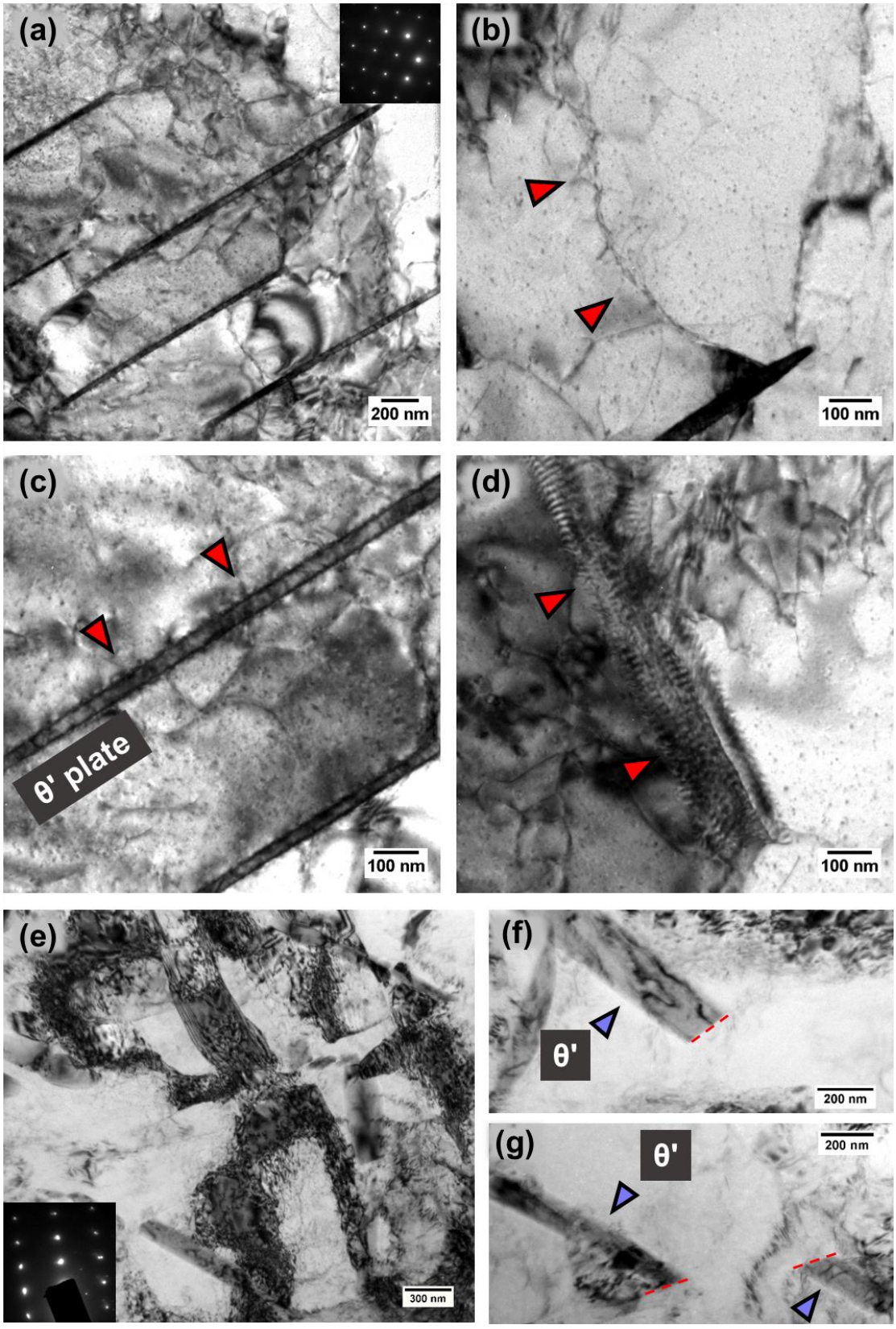
(a)
200 nm
(b)
100 nm
(c)
θ' plate
100 nm
(d)
100 nm
(e)
300 nm
(f)
θ'
200 nm
(g)
θ'
200 nm

Figure 41: (a)-(d) TEM micrographs showing dislocation activity in a representative micropillar at the initial aging condition (t= 45 min), compressed to its yield point. Formation of dislocation cell structures between precipitates is seen in (a) and (b). Edge-on view of dislocation accumulation on the interfaces of θ′ precipitates is seen in (c). Face-on view of similar dislocation storage on the interface of a θ′ plate is shown in (d). (e)-(g) TEM micrographs in a deformed micropillar (t= 45 min) showing (e) extensive dislocation storage and (f),(g) shearing of θ′ precipitates.

Ease of cross-slip in aluminum alloys also reduces the probability of dislocations interacting with elongated rod-like θ precipitates. Accounting for these factors, the local shear strain (γ) can also be directly related to the total 3D surface area of θ′ precipitates ($A_{\theta'}$) owing to their ability to store a high density of dislocations: $\gamma \, \alpha \, A_{\theta'}$. Using our 3D datasets, the total 3D surface area of θ′ precipitates ($A_{\theta'}$) can be accurately computed from Avizo®. It is also important to highlight the unique capability of the TXM in making such 3D measurements at the nanoscale possible. Quantitative estimation of the shear strain γ (as mentioned above, using TEM micrographs of the sample at t= 45 min) can be coupled with the aforementioned proportionality relationship to compute the shear strain (γ) for the remaining aging conditions.

These parameters can then be related to the yield strength (σ_y) using a variant of the relation used in Ref. (Russell and Ashby 1970),

$$\sigma_y = \sigma_{\alpha-Al} + \frac{0.35G}{m}\sqrt{b\gamma/\lambda_{Mean3D}} \quad (5)$$

where γ is the local shear strain, b is the magnitude of the burgers vector of dislocations in the matrix, λ_{Mean3D} is the mean three-dimensional inter-particle spacing of the precipitate ensemble, G is the shear modulus of the Al matrix, m is the corresponding Schmid factor. As the crystallographic orientation of the Al matrix was measured using EBSD, Schmid factor analysis was used to compute m (=0.41) and determine the active slip system: $(1\bar{1}1)$ $[\bar{1}01]$. Although previous studies have roughly approximated "λ_{Mean3D}" using stereological deductions, its accurate value can only be estimated using three-dimensional characterization of the bulk microstructure, as in the current case (Figure 39(b)).

$\sigma_{\alpha\text{-Al}}$ represents the base strength of the Al matrix caused by statistically stored dislocations (shown in red, Figure 42). This was measured by testing pure Al micropillars of similar size, to avoid inclusion of any effects arising from image stresses or size of the micropillars. The yield strength (σ_y) estimated from the above model (shown in green, Figure 42) was seen to be in excellent agreement with the values measured experimentally using micropillar compression (shown in black, Figure 42). The minor deviations from the trend that are seen can be attributed to the stochastic nature of plasticity onset in micropillars, which can affect the precise determination of yield stresses during uniaxial compression of such micrometer-sized volumes of material. In summary, by coupling 3D TXM data with

TEM images, yield stresses were estimated for different aging times of a single evolving microstructure and this was corroborated through micro-mechanical testing.

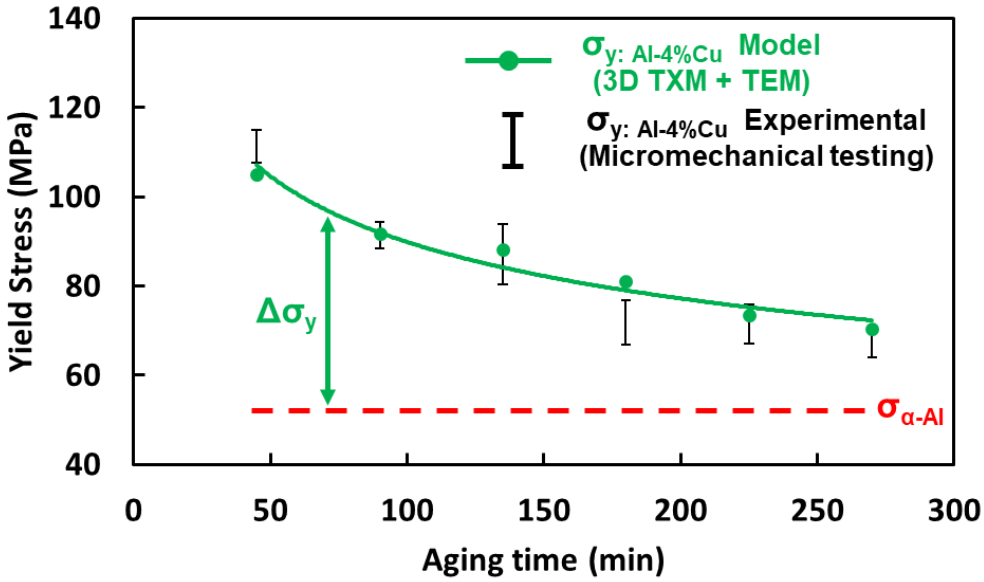

Figure 42: Variation in yield stress estimated with the proposed model using the 3D microstructure compared with experimentally measured values.

4.4 Summary

A comprehensive analysis of the deformation behavior in an Al-Cu alloy using a combination of 3D Microstructural characterization (using TXM) and micro-scale mechanical testing, in conjunction with TEM and EBSD, has been carried out. Three-dimensional morphological parameters and TEM images were used to accurately experimentally quantify and model the variation in yield stress as a function of aging time. It was also possible to quantify contributions from the Orowan and solid-solution strengthening processes, using the 3D microstructure. Histograms of 2D and 3D inter-particle spacings provided novel insights into understanding the deformation mechanisms in such alloys.

In situ uniaxial micro-compression experiments allowed vivid visualization of the deformation processes. The strain bursts observed in stress-strain curves were directly correlated to live shearing events. For the first time, shearing of coarse θ′ precipitates (> 60 nm in thickness) was observed, which have conventionally been assumed to be shear-resistant. The deformation behavior was also seen to transition from planar to wavy slip and eventually result in the soft Al matrix flowing around the shear-resistant θ phase. These 3D TXM data sets of nanoscale precipitates can be also used as input to finite element models and eventually compared with the experimentally observed mechanical behavior.

CHAPTER 5

IN SITU 4D NANOMECHANICAL TESTING USING TRANSMISSION X-RAY MICROSCOPY (TXM)

5.1 Introduction

Emergence of advanced characterization techniques has enabled us to better understand a wide spectrum of nanoscale processes occurring in a multitude of materials. Understanding such phenomena in metallic systems can be key to nano-engineering their microstructure and hence, aid in designing next-generation structural materials with enhanced mechanical properties. After the origin of age-hardening in aluminum alloys was traced back to its microstructure (Guinier 1938; Preston 1940), a global impetus in using microstructural design to develop a better class of aluminum alloys was seen. To date, aluminum alloys are the primary choice for lightweight structural applications owing to their high strength-to-weight ratio and economic feasibility of extraction. Complex three-dimensional dispersions of brittle intermetallic precipitate particles are primarily responsible for strengthening in these alloys. Probing the structure and morphology of such nanoscale precipitates as well as characterization of other nanoscale processes have been routinely carried out using transmission electron microscopy (TEM), ever since its advent. More recently, techniques like atom probe tomography (APT) (Miller and Kenik 2004) have served to understand 3D compositional and structural information at the atomic scale. However, using such destructive post-mortem analyses alone, a thorough understanding of

a material's response to mechanical stimuli and its evolution over time cannot be obtained. Deformation mechanisms responsible for strengthening in these alloys have been a topic of debate for several decades (Blankenship, Hornbogen, and Starke 1993; Hornbogen 2001; Hornbogen and Zum Gahr 1975; J. F. Nie and Muddle 2001). For instance, although θ′ precipitates have conventionally been termed "shear-resistant", recent evidence shows delayed shearing in these precipitates below a critical thickness value (da Costa Teixeira et al. 2009). Furthermore, observations of even thicker θ′ precipitates cleaving in the current study indicate the need to redefine this critical value. These findings suggest that our understanding of such precipitation-strengthened alloys is far from complete. More recently, in situ straining experiments in the TEM (B. A. Chen et al. 2013; Liu 2011) have attempted to characterize dislocation interaction with these nanoscale precipitates. However, the 2D nature of the foil restricts our understanding of these complex 3D particles. Independent *ex situ* tests coupled with destructive characterization also introduce a factor of uncertainty in interpreting results. Whereas, monitoring real-time nanoscale structural changes in 3D non-destructively to understand the alloy's deformation behavior can provide crucial insights into dynamics of the nanomechanical processes that are operating and can also have colossal implications in refining alloy design approaches. Recent advances in hard X-ray microscopy have broadened the reach of non-destructive characterization into the nanoscale domain. Its applications can be revolutionary, as has been shown in the present case as well as in a recent study in unearthing novel phase transformation reactions occurring in aluminum alloys (C. Shashank Kaira et al. 2017).

Uniform distribution of nanoscale intermetallic precipitates in a softer aluminum matrix makes such alloys naturally occurring resilient composite materials with exceptional interfacial properties. Although such precipitate distributions impart increased strength to the material, the accompanied loss in ductility and increased probability of catastrophic failure is often a cause for safety concerns. In the present study, circumventing the conventional trade-off between strength and ductility has been discussed, by inclusion of high strength second phase precipitates that exhibit the ability to withstand severe plastic deformation. Contrary to conventionally reported brittle behavior of the Al_2Cu phase, these thicker precipitate particles display kinking and buckling accompanied with nanocrystalline grain formation in the adjacent aluminum matrix under large stresses at room temperature. A precipitate size-dependent transition in deformation mode is observed for a fixed alloy composition. To that effect, a unique state of the art compact nanoindentation system was designed to carry out *in situ* micro-compression at one of the world's leading synchrotron-based hard x-ray microscopes, to capture the initiation and evolution of damage at the nanoscale in 3D. Several other characterization techniques were used in conjunction with 4D nanomechanical testing, to elucidate on the superplastic behavior exhibited by these nanoscale precipitates and present a mechanistic understanding of deformation in such alloys. Additionally, an alloy design strategy in aluminum-copper alloys is proposed based on our novel observations of anomalous ductility demonstrated by coarse θ′ precipitates.

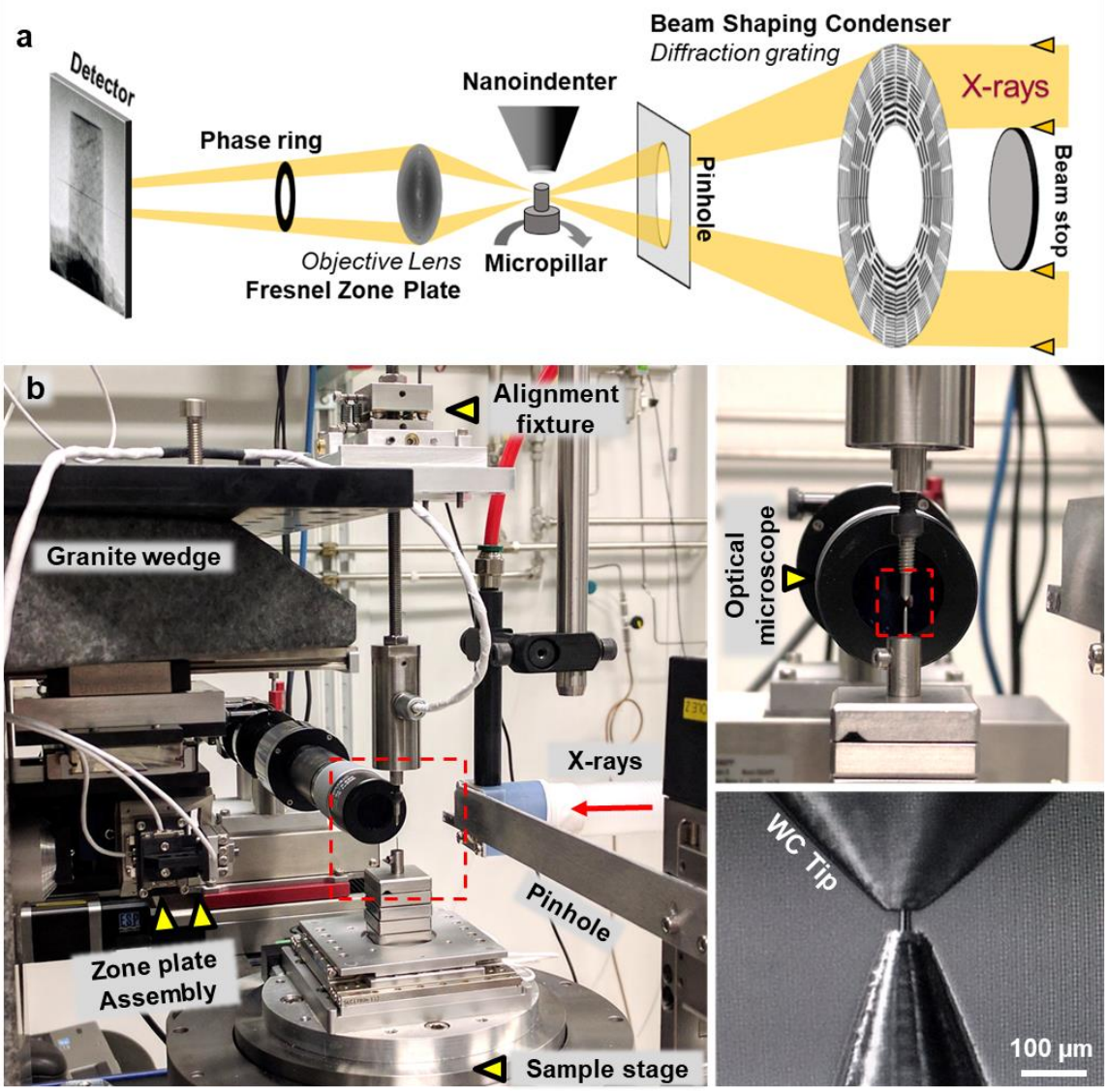

Figure 43: (a) Schematic showing *in situ* 4D nanomechanical testing setup.

(b) Instrument setup of the TXM as well as the *in situ* nanoindenter, with magnified views of the WC flat tip and Al-4%Cu micropillar at needle tip.

5.2 Materials and Experimental Procedure

Al-4wt.%Cu wires of 5N purity having a 0.5 mm diameter (Princeton Scientific Corp., Easton, PA, USA) were mechanically sharpened to fine tips. These wires were solution treated at 535 ^{o}C, followed by immediate quenching in ice water and aging at 350 ^{o}C. Absorption full-field Transmission X-ray Microscopy (TXM) was performed at sector 32-ID-C of the Advanced Photon Source (APS). Due to the instrument's limited depth of field, micropillars roughly 20 µm in diameter and 40 µm in length (Figure 44(c)) were fabricated at the tips of sharpened wires using a dual-beam Zeiss® Auriga focused ion beam (FIB) workstation. A Ga^{+} ion beam, at an accelerating voltage of 30 keV, was used at a range of currents, starting with 16 nA to mill out a coarse pattern, followed by final milling at 4 nA, 1 nA and 240 pA, respectively, to minimize taper. Imaging was performed at the TXM using a monochromatic beam at 9.1 keV, just above the Cu *K*-edge to maximize the contrast between the Al_2Cu and Al phases. Using an ultra-stable stage design, the amplitude of mechanical vibrations was reduced to about 4 nm (RMS) and it was possible to extract a spatial resolution of sub-60 nm from the TXM (with a voxel width of 16 nm). A more detailed description of the stage design has been addressed elsewhere (De Andrade et al. 2016). Tomograms were obtained at incremental strains to study the evolution of damage as the micropillar was compressed. 3D reconstructions were performed using Tomopy, an open source Python based toolbox used to analyze synchrotron tomography data (De Carlo et al. 2014; Dogˇa Gürsoy et al. 2014). Subsequent 3D segmentation, quantification as well as visualization were carried out in Avizo® Fire.

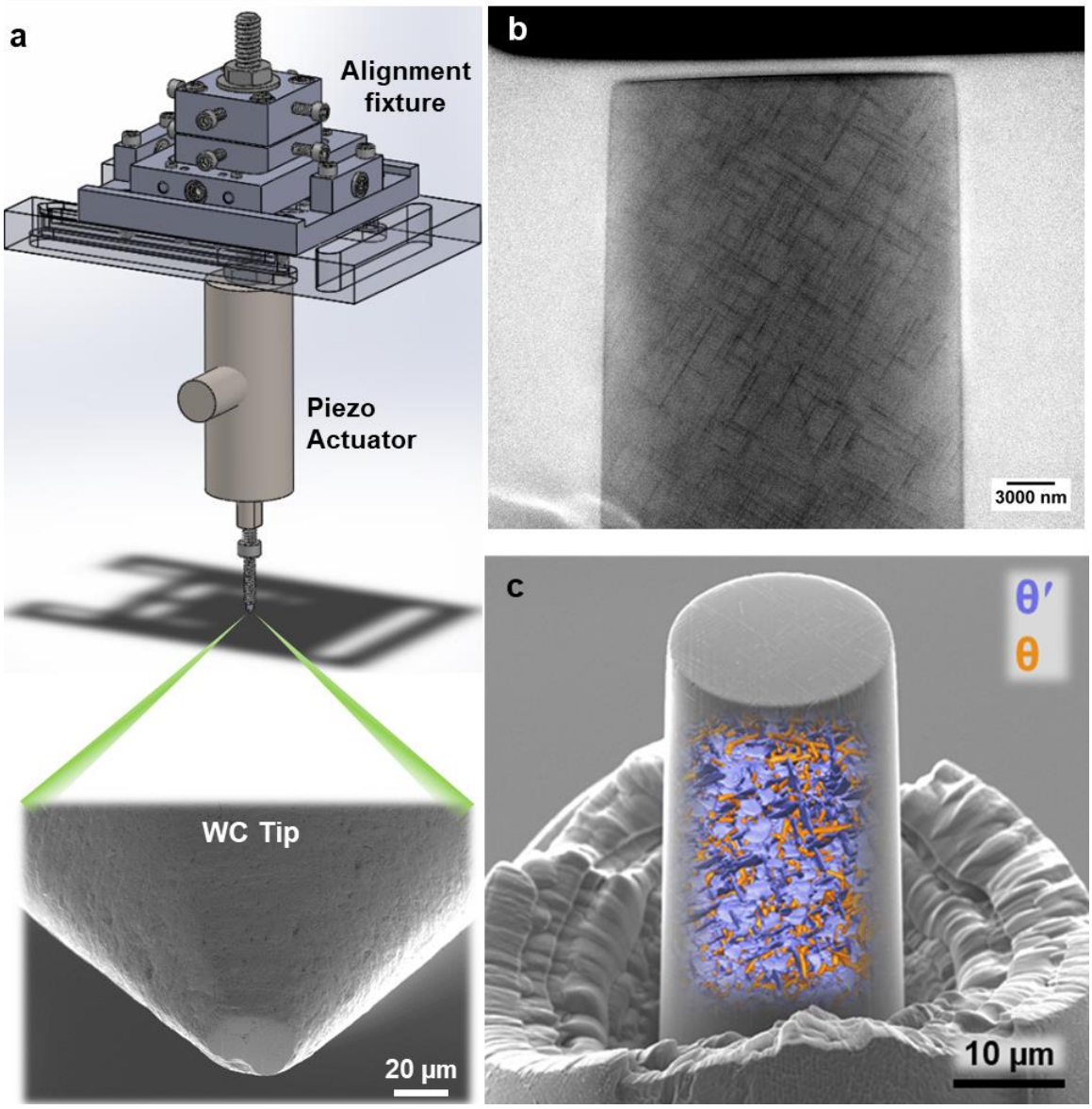

Figure 44: (a) Schematic showing the *in situ* nanoindenter, with (b) a magnified view of the WC flat tip, fabricated using the FIB. (c) SEM image of the Al-4%Cu micropillar fabricated at a needle tip. 3D rendition of the bulk microstructure characterized using the TXM has been superimposed for visualization.

A specialized nanoindentation system was designed for the *in situ* tests (Figure 44(a)). A high precision, electronically controlled piezo-ceramic motor (Kinetic Ceramics, Hayward, CA, USA) with sub-nanometer precision and 100 μm travel was used to drive the indenter head into the sample. The indenter head was fabricated by tightly pressing a WC ceramic rod into a slot that was machined in the end of a screw, which was tightly threaded into the motor head. The ceramic indenter tip was sharpened using sandpaper, and the end was precision-flattened to 60 μm diameter using focused-ion beam milling. High precision rails with micro adjustment set screws and locking capability were fixed to a large granite block atop the tomography positioning stage. The precision set screws were used to position the motor head above the sample with 3 μm accuracy. Displacement of the indenter head into the sample was driven using a high precision voltage control from National Instruments MyDAQ (Austin, TX, USA), with the displacement measured *in situ* using the 2D nanotomography projections. After an acceptable displacement was reached, the indenter head was raised and a tomography scan was performed to examine each selected level of sample deformation.

For post-TXM analysis using EBSD, the deformed micropillar was cross-sectioned using the FIB at an accelerating voltage of 30 keV and using a current of 1 nA and EBSD was performed on these flat sections, using a step size of 0.5 μm to characterize the deformation-induced texture in the α-Al matrix. TSL® OIM data collection and analysis software was used to analyze the acquired EBSD data. Post-EBSD, a TEM lamella was lifted-out using a nano-manipulator and subsequent TEM investigation was performed in an aberration-corrected FEI 80-300 Titan™ operated at 300 kV.

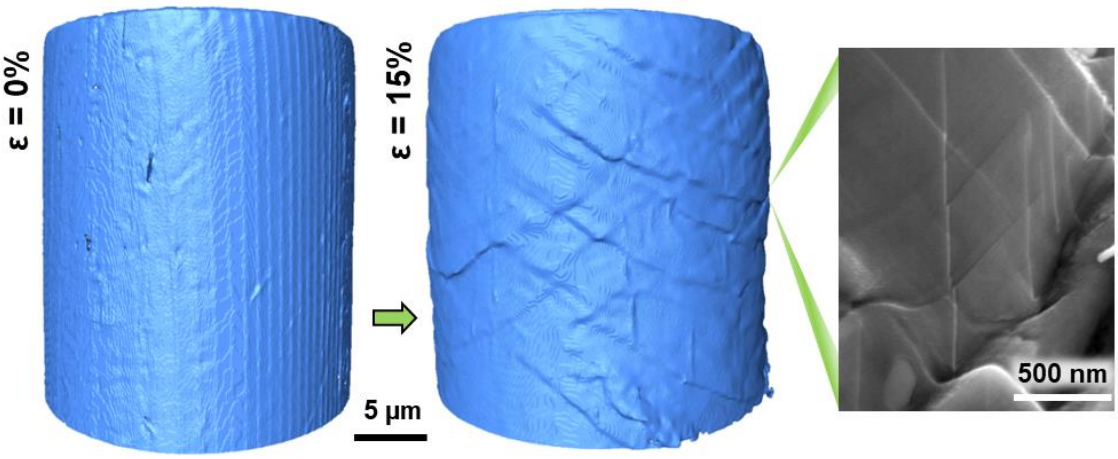

Figure 45: 3D rendition of the micropillar's surface with increasing strain, characterized using the TXM. Multiple slip traces are evident from the micropillar's surface relief.

5.3 Results and Discussion

5.3.1 *In situ* 4D Nanomechanical testing

A pure Al-4wt.%Cu alloy was investigated in this study. Probing specimens of metallic materials using the TXM necessitates a special fabrication procedure, due to its limited depth of field (Chandrashekara S Kaira et al. 2016) and to ensure sufficient X-ray transmission. To this end, a single-crystalline micropillar (20 µm x 40 µm) was fabricated using a focused ion beam (FIB) on a mechanically sharpened Al-4%Cu wire tip having very large grains (~300 µm). This specimen geometry also aided in investigating the alloy's micro-mechanical properties, as micropillar compression has become an increasingly popular technique to monitor the deformation response of a material at the micro and nano length scales. This specialized technique also enables us to probe a polycrystalline

material's intragranular mechanical behavior. A similar aging temperature (350 ^{o}C) was utilized in this study to better understand damage evolution on application of loads in similar Al-Cu alloys. Difference in their individual attenuation co-efficients aided in discerning the two different phases (θ' & θ) present. 3D tomographic imaging at such high spatial resolutions (sub-60 nm) requires design of a specialized stable sample stack devoid of any mechanical vibrations or thermal drift and precise alignment of all the optics. The sophisticated stage design at sector 32-ID-C allows imaging without the use of any digital drift correction procedures which are conventionally used for aligning 3D tomographic stacks. To also render *in situ* mechanical testing of such miniaturized volumes possible without compromising the quality of 3D imaging, it was necessary to custom design a compact nanoindentation system that would be suspended mid-air atop the sample. This system was hooked onto a large granite wedge that serves to hold the zone plate objective lens assembly in place, as shown in Figure 43. The alignment fixture (Figure 44) aided in precise axial and angular positioning of the tungsten carbide (WC) micro-flat punch over the micropillar top. 2D projections from the TXM were used in conjunction with a perpendicularly placed optical microscope to aid in precise positioning. As the micropillar was compressed at a constant displacement rate, we performed 3D nanoscale tomography at incremental strains to probe the evolution of damage in the precipitation-strengthened Al-Cu alloy (Figure 45). Onset of plasticity in such materials is marked by propagation of slip along planes with the highest Schmid factor. Multiple slip traces are visible in the 3D rendition (using TXM) of the micropillar's surface relief shown in Figure 45. To date,

however, only scanning electron microscopy (SEM) has been extensively used to perform surface analyses and understand the mechanical response of such micro-volumes.

Ordered brittle θ′ (Al_2Cu) precipitates have commonly been reported to contribute to alloy strengthening through numerous dislocation interaction mechanisms: chemical strengthening, order strengthening (Ardell 1985), and more recently, through buildup of Orowan loops (da Costa Teixeira et al. 2009). SEM investigation of the micropillar surface in our current study also visually suggests shearing of such ordered precipitates to be the dominant deformation mechanism (Figure 45). However, it is important to highlight that this observation can be quite elusive owing to the difference in stress states in the interior and at the surface of these micro-volumes. The increased driving force to form steps at micropillar surfaces (Hurtado and Ortiz 2012) and the presence of image stresses at the surface (Weinberger and Cai 2008) can influence the stress field around dislocations and accelerate their escape in the vicinity of free surfaces. Further inspection in the bulk of the micropillar using 3D non-destructive imaging reveals buckling and kinking of thicker θ′ precipitates dispersed in the path of these slip bands, unveiling their extraordinary ability to undergo unprecedented plastic deformation. We characterized the engineering stress-strain response from such micro-volumes *ex situ* using a commercial nanoindenter. The plastic domain reveals the alloy's strain hardenability and is vividly marked by several intermittent "strain bursts". The minor bursts at the onset of plasticity correspond to localized dislocation avalanches within the micropillar whereas the relatively larger bursts are likely to be caused from kinking events at precipitates, which eventually pave way to

several slip bands shearing the micropillar, causing massive bursts at higher strains. The extensive ductility exhibited by the alloy can be attributed to this new deformation mode.

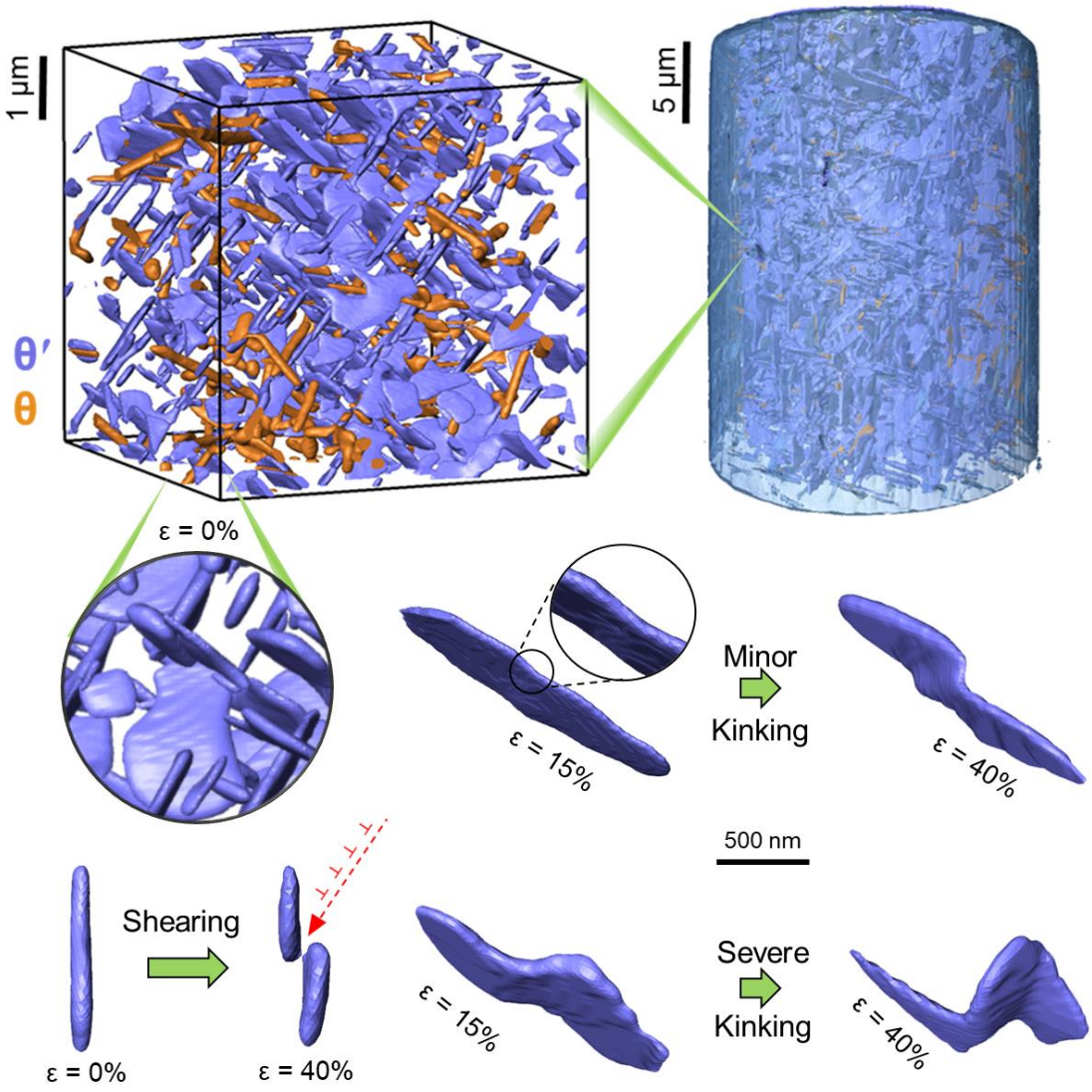

Figure 46: 4D Nanoscale characterization of deformation in θ′ precipitates in an Al-4%Cu alloy, upon mechanical loading.

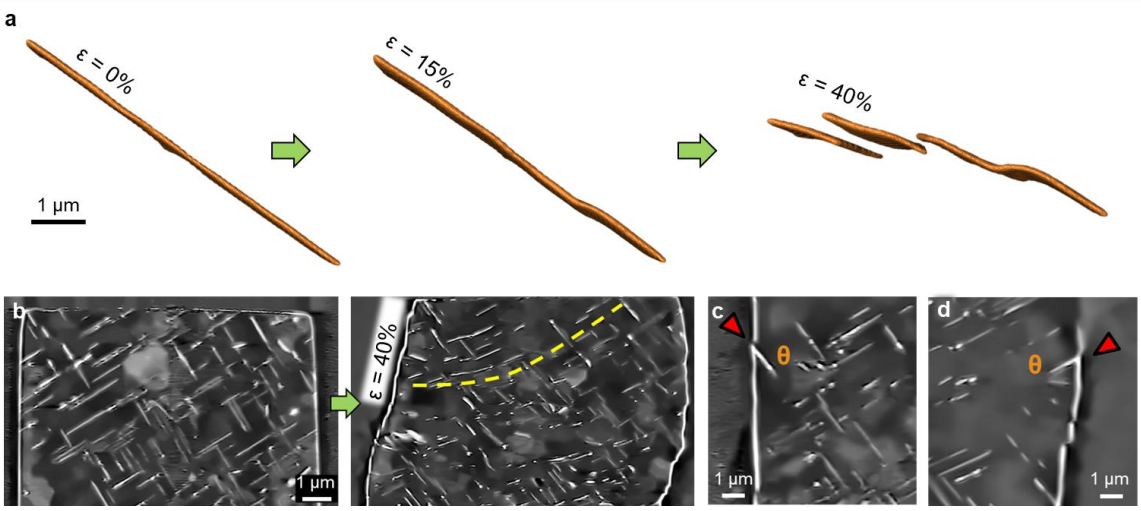

Figure 47: (a) 4D Nanoscale characterization of deformation in a θ precipitate. (b) 3D rotation and reorientation of θ′ precipitates (upon deformation), as indicated by the dotted trace line. (c), (d) Initiation of slip at the α-θ interface.

5.3.2 Damage evolution during *in situ* testing

Non-destructive 3D characterization enables us to precisely and vividly visualize structural changes to the morphology of precipitates as they undergo kinking and study its evolution. Figures 46 and 47 depict progression of kinking within precipitate structures. Distribution of strain in such micro-volumes is inhomogeneous and as a result of such shear localization, a larger degree of kinking is observed in case of precipitates intersecting major shear bands with pronounced slip traces and more localized plasticity. This classification has been depicted in Figure 46. The degree of kinking can also be quantified by the enclosed angle. This is seen to evolve with strain and the large kinking angles indicate their ability to effectively accommodate enormous plastic strains. Their impermeability to slip also results

in an increase in the density of geometrically necessary dislocations, eventually leading to pronounced strain hardening in such alloys. In the absence of 4D testing, such a kinked structure could easily be mistaken for precipitate segments shearing and re-orienting. The relative orientation of precipitates w.r.t. the slip plane (3D spatial distribution) also plays an important role in determining the nature of interaction between the two. As we already know, θ′ exists as three orthogonal variants and only those variants whose habit planes oppose the direction of slip exhibit kinking. θ′ precipitates whose habit planes subtend acute angles with the active slip plane only experience 3D reorientation as shown in Figure 47(b).

The ductile behavior of these precipitates, however, is a size-dependent phenomena. It was seen that precipitates with thicknesses on the order of 80-100 nm and greater displayed kinking whereas those on the lower end of the spectrum (~60 nm) were seen to be sheared, as captured in Figure 46. Reasoning behind this switch in deformation mode from shearing to kinking as thickness increases can be attributed to the unreasonably large shear stresses that would otherwise be needed to cleave the thicker precipitates.

The nature of interfaces of different precipitates (θ′ & θ) can also play a significant role in determining the alloy's mechanical response. The semi-coherent nature of interfaces in the θ′ phase ensures its compatibility with the α-Al matrix on deformation, without the generation of voids or cracks. Whereas, the relatively incoherent nature of the α-θ interface can initiate interface failure. Evidence for this is seen from 2D slices of the 3D re-constructed dataset in Figure 47(c), where initiation of slip traces on the micropillar surface is associated with θ-α interface failure. However, if the broad faces of θ are oriented to

impede propagation of slip, it can display kinking behavior similar to that observed with θ′ precipitates. Figure 47(a) shows localized formation of a kink in a lath-shaped θ particle, which is eventually sheared off at multiple locations at higher strains, accompanied by significant 3D rotation.

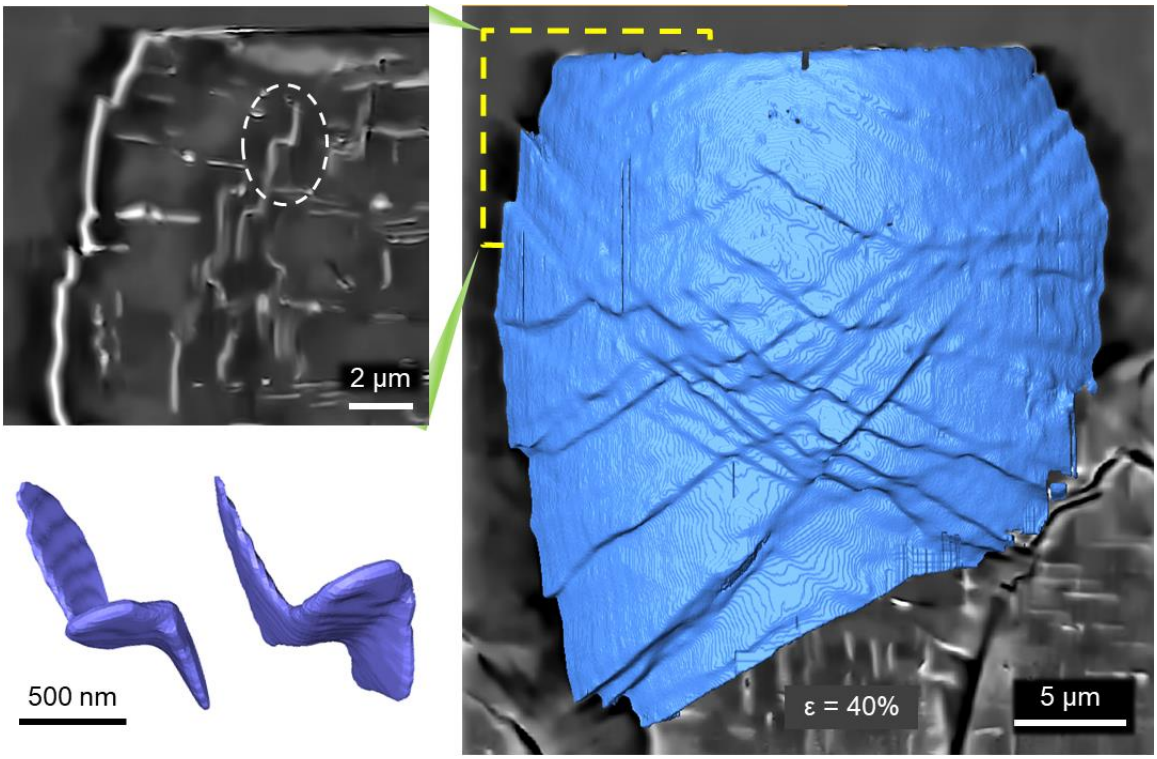

Figure 48: (a) 3D rendition of the micropillar's surface at 40% strain, characterized using the TXM. Segment of a 2D slice from the 3D dataset shows a kinked θ′ precipitate (encircled) which has also been depicted in 3D.

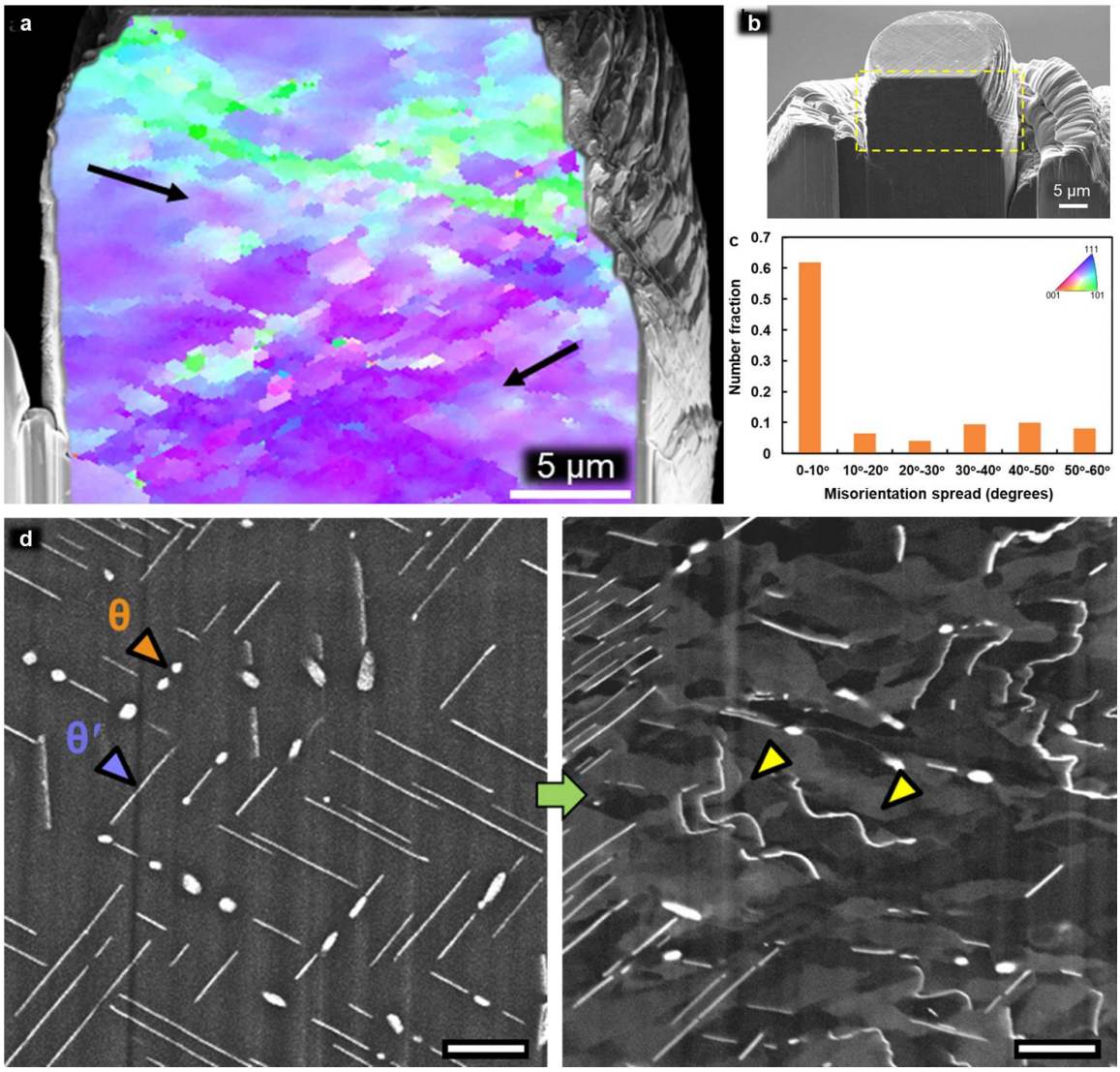

Figure 49: (a) EBSD map of the FIB cross-section of the deformed micropillar in (b) showing significant deformation-induced texture. (c) Histogram of misorientation angles from the EBSD map. (d) SEM images showing kinking and nanocrystalline texture in the deformed microstructure as compared to the un-deformed microstructure, obtained from beneath the base of the micropillar.

5.3.3 Comprehensive correlative analysis

By employing a unique correlative approach, various complementary characterization techniques can be used to render a thorough understanding of the deformation process. The deformed micropillar was cross-sectioned using a focused ion beam (FIB) to map its crystallographic orientation using electron backscatter diffraction (EBSD). This revealed a considerable degree of microstructural refinement occurring as a result of deformation. The initially single-crystalline micropillar developed a deformation-induced nanocrystalline texture (Figure 49(d)). Its initial crystallographic orientation was mapped from beneath the base of the micropillar, due to the absence of any grain boundaries. Aluminum's high stacking fault energy facilitates dislocation cross-slip, leading to polygonization and eventually, grain rotation to accommodate the large strains. This form of continuous dynamic recrystallization (CDRX) (Huang and Logé 2016) occurred as a result of extensive dislocation storage caused by the large surface area of coarse θ′ precipitates. A larger degree of grain refinement was observed in the vicinity of precipitates, as corroborated using high resolution SEM to reveal the substructure through electron channeling contrast. For such coarse microstructural distributions, the inter-particle spacing exceeds the self-trapping distance of dislocations (Russell and Ashby 1970), causing mutual interaction of dislocations to play an active role, thereby leading to polygonization. EBSD maps also reveal extensive lattice rotation along the primary and secondary slip planes, leading to larger misorientation angles in these directions as a result of localized grain-boundary mediated plasticity. These regions also corresponded to larger degrees of kinking, proving the existence of a symbiotic relationship between onset of

kinking and grain-boundary mediated plasticity. The aforementioned grain refinement is also expected to contribute to some extent of strengthening via strain hardening as reasonably large stresses are needed to trigger grain rotation and grain boundary migration (T. Hu et al. 2015). We can also quantify the overall degree of lattice rotation, as shown in the graph in Figure 49(c), representing the histogram of misorientation angles.

Conventional understanding of shearing in ordered precipitates invokes antiphase boundary (APB) formation and migration as it penetrates through the particle causing it to shear (Ardell 1985). Unreasonably large stresses necessary for shear prevent its occurrence in thicker precipitates. The nanostructure of these kinked regions in θ′ was investigated using transmission electron microscopy (TEM) to reveal the governing mechanisms. A tilted view of a section of its habit plane reveals a considerable amount of APB activity (Figure 50(c)), indicating significant disorder in these second phase particles. The edge-on view of these precipitates (Figure 51), however, revealed the most interesting aspects of the kinking phenomena. The entire thickness of the precipitate is divided into individual layers, which slide over each other in order to accommodate the total shear strain. Localized diffraction contrast in the curved region indicates a severely strained lattice to accommodate deformation. These precipitates aren't fully ordered to begin with, as the origin of a small fraction of these APBs can be traced back to their nucleation at impingement sites during coalescence of coarse θ′ precipitates (Weatherly 1970). Application of large stresses causes rapid multiplication of such APBs, rather than their nucleation, and their mobilization on discrete (001) planes, eventually leading to partitioning of θ′ into layers.

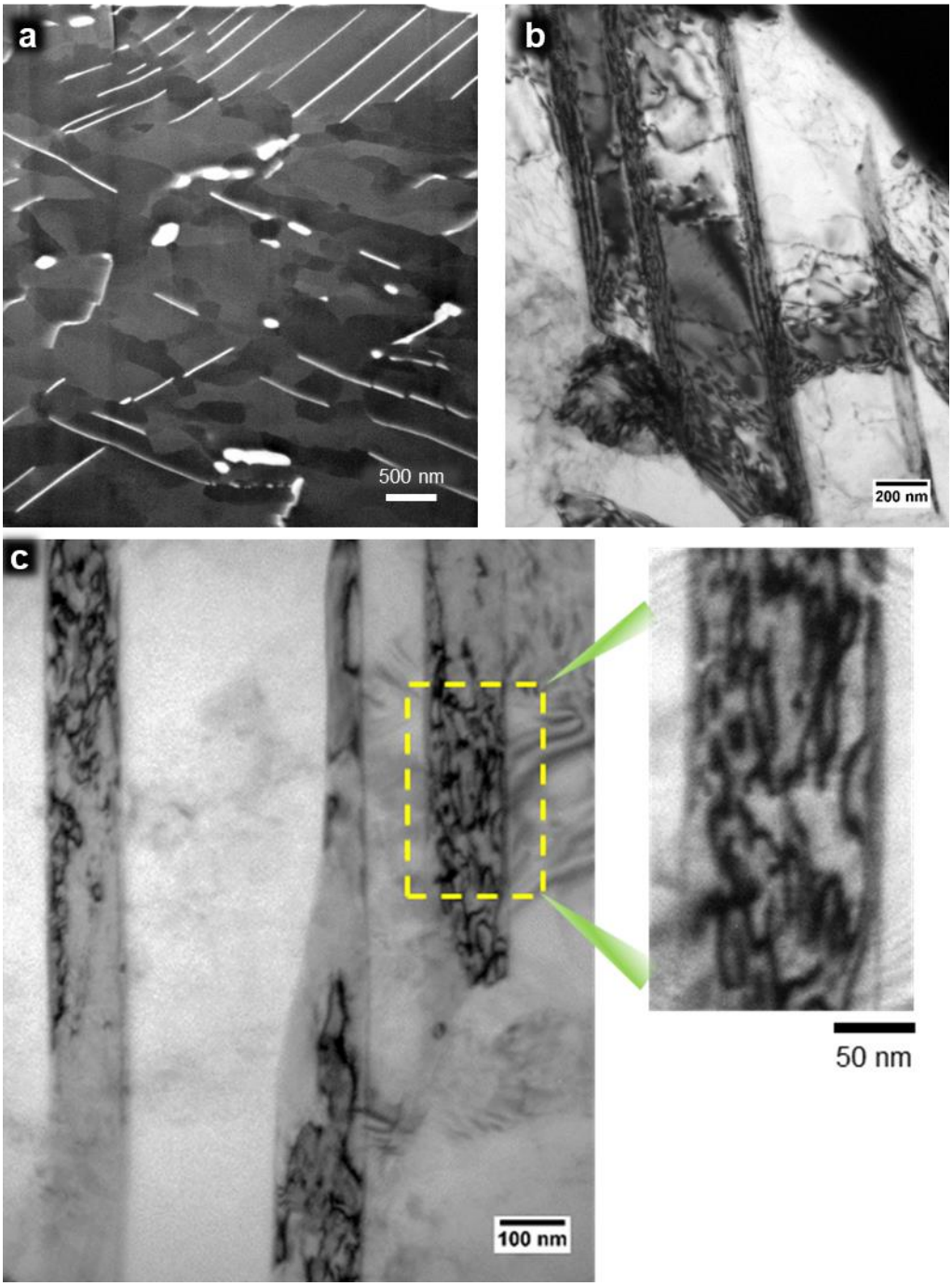

Figure 50: (a) SEM image of TEM Lamella showing deformation-induced nanocrystalline texture. (b) Diffraction contrast in TEM image showing lattice rotation between θ′ precipitates. (c) Antiphase boundaries (APBs) in θ′ precipitates.

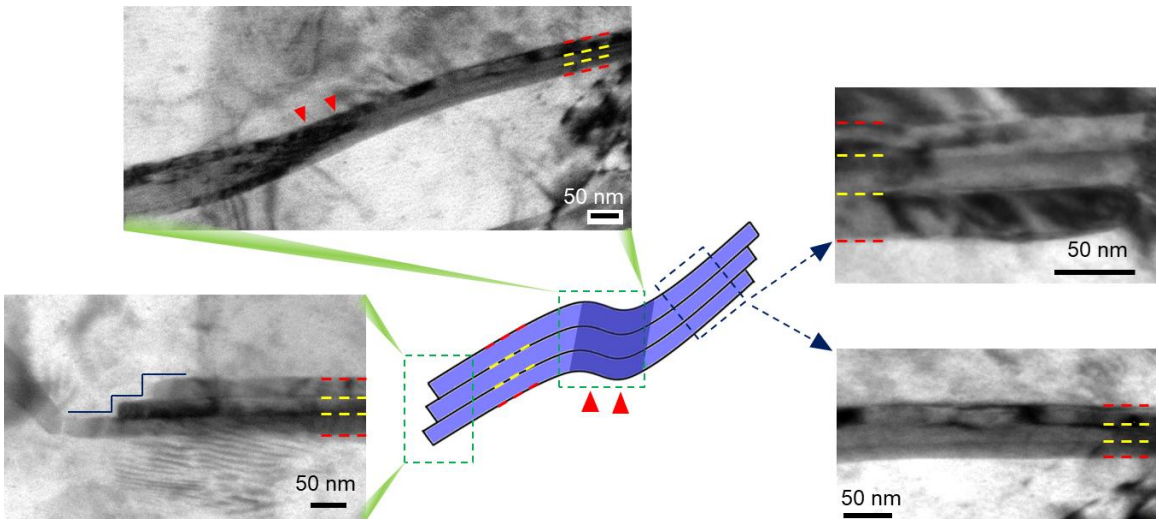

Figure 51: TEM images illustrating the mechanism behind kinking phenomena in θ′ precipitates of Al-Cu alloys.

5.4 Summary and Conclusion

A comprehensive mechanistic understanding of precipitate deformation in Al-Cu alloys can be obtained by integrating all this information, as summarized in the schematic shown in Figure 52(a). Incoming arrays of dislocations cause pile-up at precipitate fronts. When the number of dislocations rises substantially, the shear stress exerted by this array causes the finer precipitates to cleave. While for thicker precipitates, the stresses exerted by the dislocation pile-up are insufficient to shear precipitates and instead cause localized lattice rotation which is accompanied by 3D rotation of the precipitate. Prolonged loading, however, can cause kinking in thick precipitates due to an increased density of APBs and their mobilization on discrete (001) planes causing the precipitate to accommodate deformation in layers. The ability of dislocations in α-Al to cross-slip facilitates their

rearrangement causing polygonization. The findings of this study inspired a novel alloy design with an intragranular bimodal θ′ distribution as shown in Figure 52(b). The potency of a high density of fine θ′ precipitates in contributing to large yield strengths is already well established. Combining this with interspersed coarse θ′ precipitates can greatly improve the ductility of the alloy, owing to their ability to withstand large plastic strains without failing. The relative proportion of each can also be altered to engineer the alloy's toughness accordingly. Consequently, the deformation-induced localized grain refinement in the vicinity of these coarse θ′ precipitates also contributes through grain boundary-mediated plasticity (Shan et al. 2004). It's already known that alloying trace addition of elements such as Sn promotes early nucleation of θ′ phase and lead to a coarser precipitate distribution (J.F. Nie and Muddle 2008). By confining such elemental additions to the form of isolated islands, such bimodal distributions of θ′ precipitate sizes can be achieved. However, it is also important to suppress nucleation of the θ phase, to mitigate interfaced-related failures.

In summary, tracking evolution of damage using synchrotron-based *in situ* 4D nanomechanical testing has unearthed a new deformation mode and the cause for anomalous ductility in Al-Cu alloys. It was also possible to clearly visualize complex 3D morphological changes occurring in individual precipitates with increasing strain. By using complementary correlative techniques like transmission electron microscopy, scanning electron microscopy and electron backscatter diffraction to gain atomic and crystallographic perspectives of the deformation processes involved, a more fundamental and comprehensive understanding of Al-Cu alloys was achieved. The efficacy of 4D

nanomechanical testing as a promising technique for probing a variety of material systems has been effectively illustrated. A novel damage-tolerant alloy design has also been proposed based on the findings from this study.

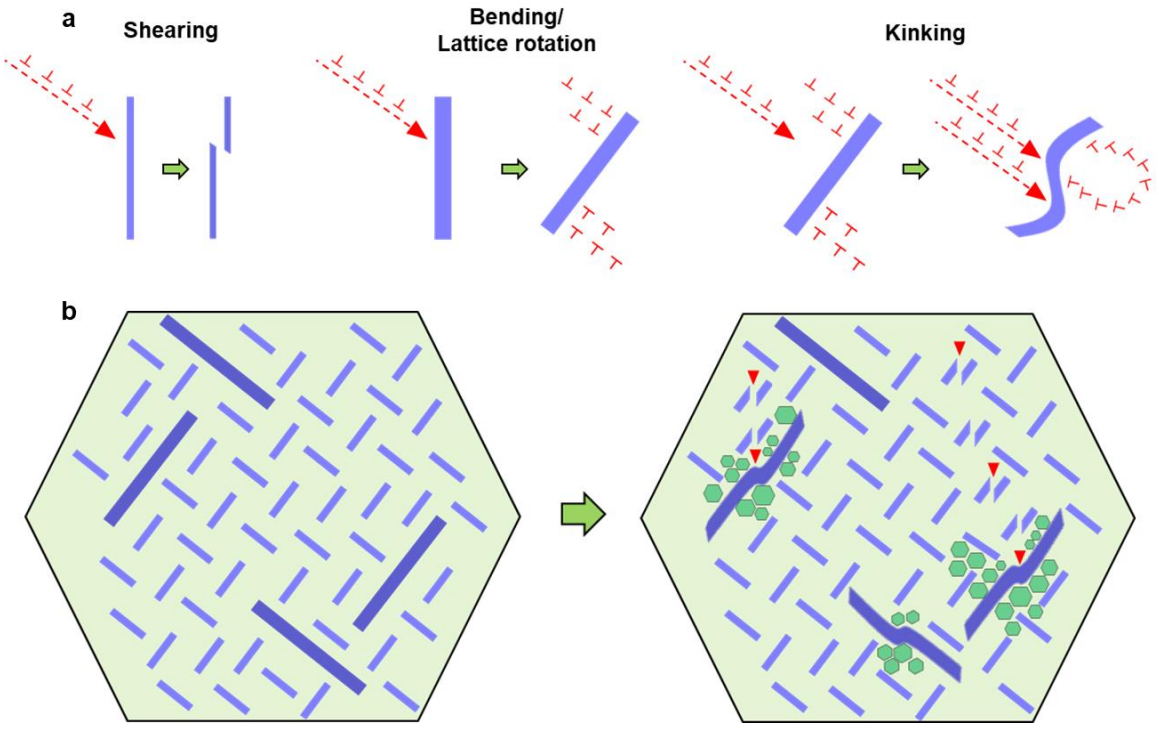

Figure 52: (a) Schematic of size-dependent deformation modes in θ′ precipitates of Al-Cu alloys. (b) Novel alloy design depicting intragranular bimodal θ′ precipitate distribution to enhance toughness.

CHAPTER 6

AUTOMATED SEGMENTATION USING CONVOLUTIONAL NEURAL NETWORK (CNN) APPROACH

With the rapid pace of advancement in the use of X-ray computed tomography for quantitative 3D imaging (Maire and Withers 2013), both at synchrotron sources and in lab-scale systems, there is an ever increasing need to simplify analysis of the large volumes of acquired data. Depending on whether absorption contrast or phase contrast imaging is implemented, subsequent analysis of the images can vary significantly. The latter results in an increased edge contrast and is primarily used for imaging features with comparable attenuation. For accurate quantification and 3D visualization of the microstructure, the different features/phases present in the scanned volume need to be classified/segmented accordingly. Post-processing the acquired 3D image stacks is generally performed to ease the process of segmentation. Depending on the variety of features present and their homogeneity, the wide distribution of grayscale values in these images need to discretized accordingly. In most cases, these grayscale images cannot be segmented using simple thresholding strategies. This is quite challenging as the complexity of features can require manual intervention, making it an extremely time intensive task. Recently, introduction of semi-automated techniques (Mortensen and Barrett 1998) has rendered segmentation a relatively less laborious process. However, it still remains impractical to manually segment complete datasets, especially with the advent of 4D characterization and continually improving temporal resolution of data acquisition. As a result of this, segmentation and

analysis is often restricted to small sub-volumes which can result in statistically insufficient data.

With advances in X-ray optics, Transmission X-ray Microscopy (TXM) has made tomography possible at unprecedented spatial resolutions (20 and 60 nm) (De Andrade et al. 2016). As features of interest approach spatial resolution limits of the technique, substantial noise can populate in these images. Complexity of these nanoscale features as well as presence of multiple phases in such images, demands careful segmentation of these image stacks. Fortunately, with the recent advent of deep learning (LeCun et al. 2015) and its use in image classification (Lawrence et al. 1997), its application in tomography data analysis can be quite promising. Its implementation in this field can make segmentation almost an entirely automated process and its implications can be revolutionary.

A deep neural network approach is utilized in this study to learn the mapping between the original images and manually segmented images. The trained network is then used to perform automated segmentation for large datasets (Courtesy of Dr. Xiaogang Yang, Advanced Photon Source, Argonne National Laboratory). This technique can emulate the manual segmentation approach to segment X-ray images with reliable quality and it can speed up the process by several orders of magnitude. Convolutional Neural Networks (CNN) is the main branch of deep learning that was originally developed for pattern recognition (LeCun et al. 1998). Recently, it has also been used in X-ray image analysis (Cernazanu-Glavan and Holban 2013). The CNN configuration used in this study is similar to that used by Yang et al. in calibrating the rotation axis for X-ray CT (Yang et al. 2017). However, the objective here is to implement the supervised learning approach

(Yang et al. 2017) to the segmentation process by using an acquired 2D TXM slice and a corresponding manually segmented (single) image, as training input for the CNN model. The trained network is then used to segment the entire 3D image stack. A schematic of this workflow has been depicted in Figure 53. A Python toolbox named Xlearn (https://github.com/tomography/xlearn) was used to implement the aforementioned CNN model. The toolbox is based on the Keras and the Theano packages.

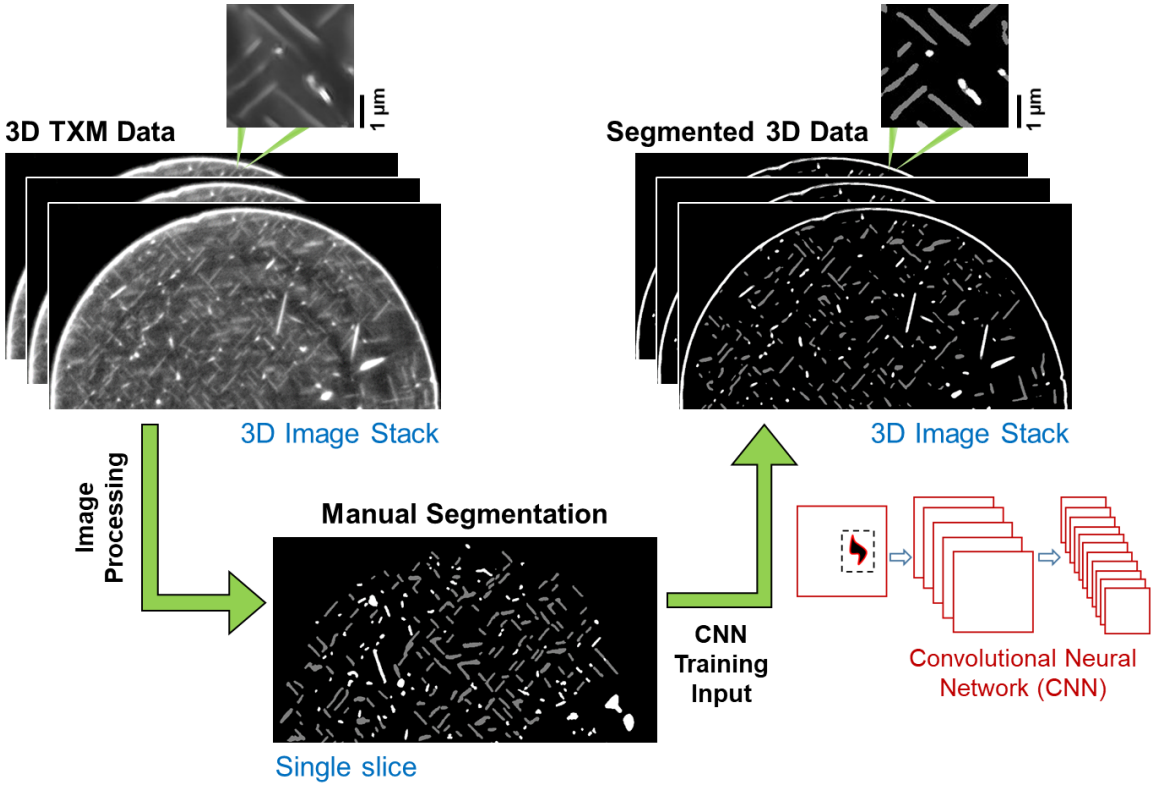

Figure 53: Schematic showing sequence of steps in using Convolutional Neural Network (CNN) approach to perform automated segmentation.

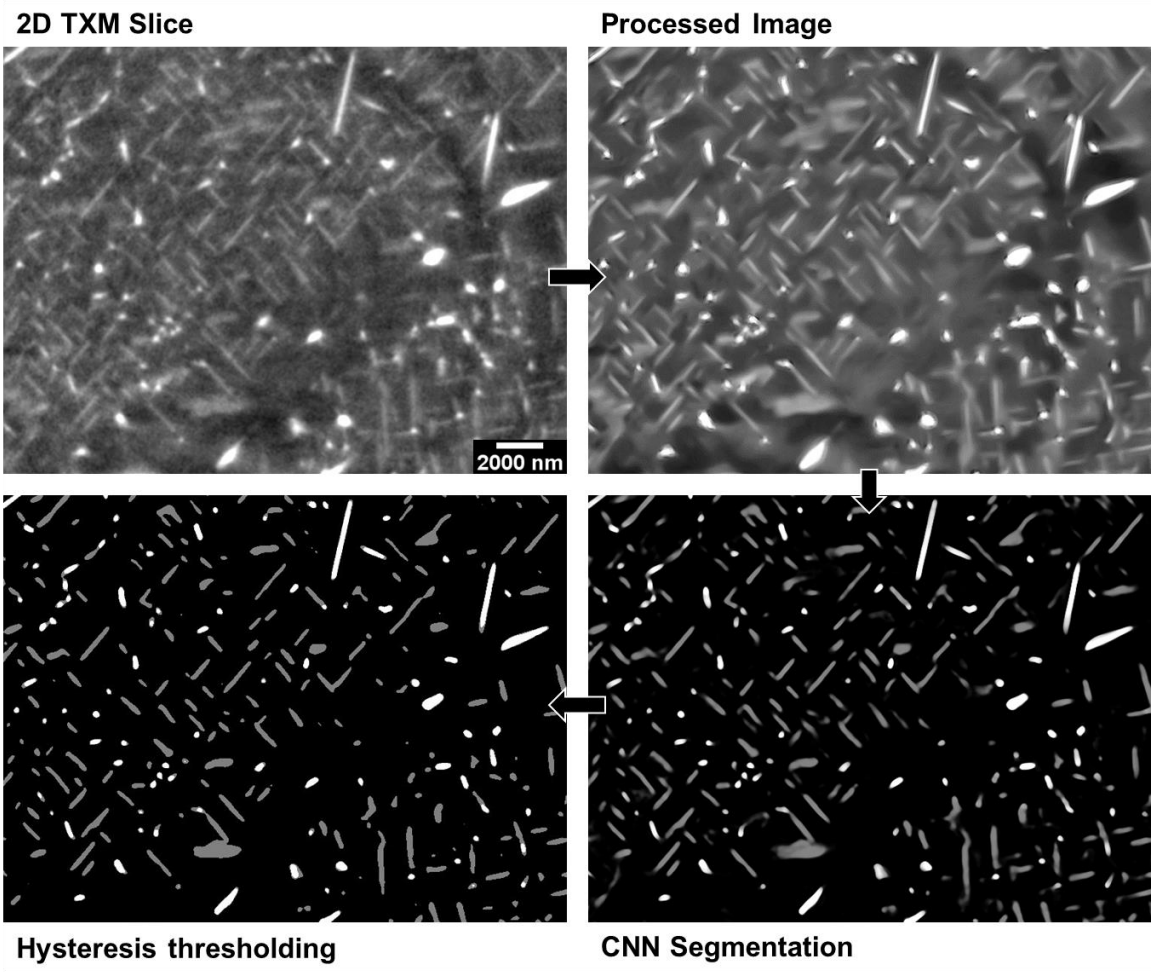

Figure 54: Sequence of steps involved in automated segmentation using the Convolutional Neural Network (CNN) approach, on a single 2D TXM slice.

Application of this technique is crucial in the current scenario as the complex particle shapes of both the θ′ & θ phases and the marginal difference in grayscale values between the α, θ′ & θ phases make it almost impossible to accomplish the task of segmentation on large datasets using any other technique. Figure 54 shows the sequence of steps applied to the X-ray images in order to segment them. The X-ray image is initially processed using a combination of Mean 3D, Bandpass and Non-local means denoise filters in ImageJ (C. A. Schneider, Rasband, and Eliceiri 2012). The most important of these being the Non-local means filter (Buades, Coll, and Morel 2005) which is an edge-preserving filter. The trained CNN is then used on the processed dataset to obtain a partially segmented image. Hysteresis thresholding, an adaptive thresholding procedure (Canny 1986), was applied to this data to separate the θ′ & θ phases based on grayscale values and connectivity, resulting in a completely segmented image stack where each phase corresponds to a single pixel value.

The results of this technique were remarkable. Figure 55 compares a manually segmented volume with one that was segmented using the CNN approach (Al-4%Cu, T= 350 ^{o}C, t= 45 min). The volume of the latter was nearly 32 times that of the former. Manual segmentation was performed using a semi-automatic 3D region growth based technique. It makes use of the local contrast gradient to select a feature in 3D. It took approximately 36 hours to manually segment the sub-volume, while the larger volume was segmented automatically through the CNN, with the only bottleneck being the time taken to manually segment the 2D training slice (~2 hours). The time taken for automated segmentation is a function of the hardware used to implement the algorithm. Using the

processing hardware mentioned in (Yang et al. 2017), it took the CNN just nearly 20 hours to segment the entire dataset. However, this can be reduced to about 10 minutes by executing the CNN code on a GPU cluster.

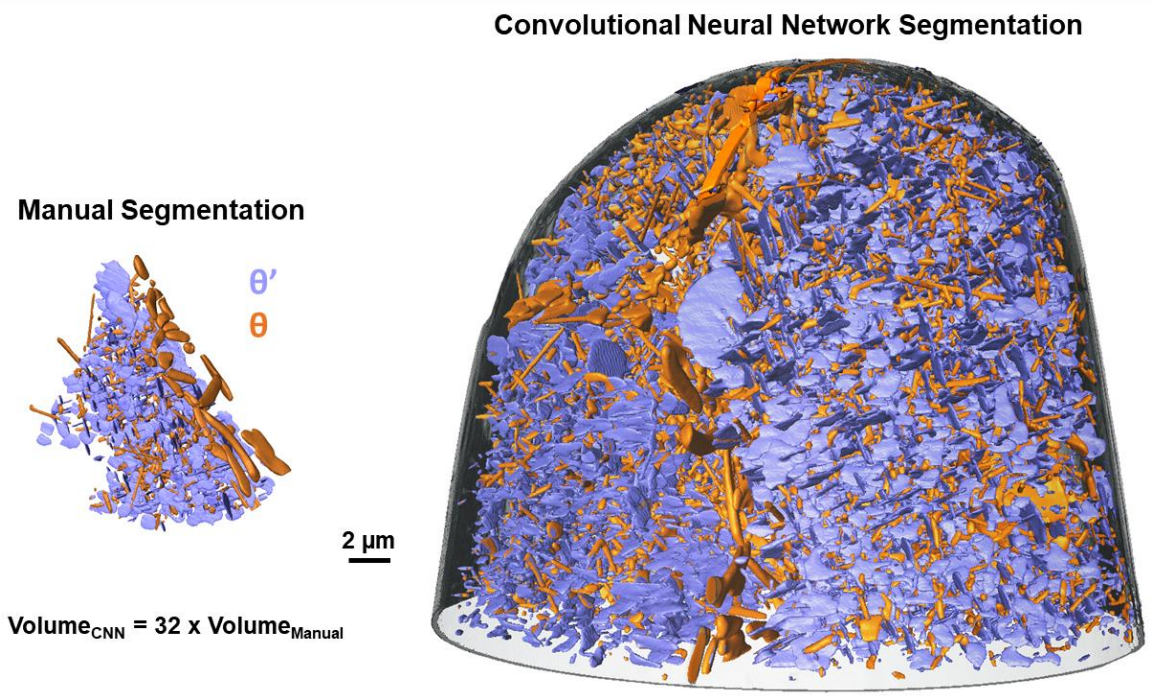

Figure 55: Comparison of manually segmented sub-volume with the entire 3D TXM image stack segmented using Convolutional Neural Network (CNN) approach.

CHAPTER 7

CONCLUSIONS

7.1 Summary of Research Findings

- Synchrotron-based hard X-ray Nano-CT (Transmission X-ray Microscopy) enabled 4D characterization of the evolution of the microstructure present in Aluminum alloys. The morphology and spatial distribution of nanoscale θ′ and θ precipitates an Al-Cu alloy were accurately quantified and visualized in 3D.
- Aging at 350 ºC revealed complex 3D transformation reactions (θ′ to θ) that were occurring in the alloy, most of which are nearly impossible to capture using other characterization techniques. The ability to measure kinetics of different nanoscale phases in 3D also allowed accurate estimation of diffusion co-efficients.
- 3D measurements of precipitate dimensions rendered a thorough understanding of the coarsening behavior of θ at 400 ºC. A transition from interface-controlled to volume diffusion controlled growth in thickness of θ was captured from the scaled PSD curves. Excellent agreement was observed on comparison with theoretical size-distribution curves obtained from the LSW theory.
- Correlation of 3D nano-tomography data with EBSD allowed experimental estimation of the Orowan strengthening, for the first time, as well as quantification of the preferred orientation of the θ phase in 3D. Orowan strengthening estimated

from the 3D model was seen to vary significantly when compared to that calculated using pre-existing analytical models.

- Micropillar compression enabled determination of local mechanical properties and in conjunction with 3D Microstructural characterization (using TXM), transmission electron microscopy (TEM) and electron backscatter diffraction (EBSD), a comprehensive understanding of the deformation behavior in Al-Cu alloys was obtained.
- Experimental measurements from micro-mechanical testing were successfully reconciled with predictions from 3D TXM data using a newly proposed approach. This correlative approach also allowed quantification of contributions from different strengthening mechanisms.
- *In situ* uniaxial micro-compression experiments in the SEM allowed surface visualization of transition in deformation behavior, from shearing of θ′ precipitates at initial aging conditions to shear bands bypassing the shear-resistant θ phase. The strain bursts observed in stress-strain curves were directly correlated to live shearing events.
- A compact nanoindentation system was designed to carry out synchrotron-based *in situ* 4D nanomechanical testing using Transmission X-ray Microscopy (TXM). Using this technique, 4D evolution of damage was characterized in Al-Cu alloys, for the first time at the nanoscale. This technique allowed clear visualization of kinking of thicker precipitates dispersed in the bulk, with increasing strain. Anomalous ductility observed in these alloys was attributed to this phenomenon.

Using a correlative approach rendered a mechanistic understanding of this size-dependent transition in deformation behavior.

- Automated segmentation on 3D Transmission X-ray Microscopy (TXM) data was performed using a Convolutional Neural Network (CNN) approach and its efficacy has been discussed.

7.2 Future Work

- Transmission X-ray Microscopy using 20 nm objective ZP lens assembly will enable sub-20 nm spatial resolution for 3D Imaging, allowing visualization as well as characterization of evolution behavior of much thinner θ′ precipitates. *In situ* 4D nanomechanical monotonic as well as cyclic testing on alloys containing such precipitates will render a thorough understanding of their deformation behavior.
- With the advent of 4D characterization and related 4D experiments, segmentation using deep learning has the potential to revolutionize this field by enabling swift analysis of ultra-large volumes of data.
- Spectroscopic capabilities of Transmission X-ray Microscopy can be leveraged to thoroughly investigate phenomena such as corrosion in other complex multi-component alloys systems.

REFERENCES

Aaronson, H.I., and C Laird. 1968. “Structure and Migration Kinetics of Alpha: Theta Prime Boundaries in Al-4%Cu: Part II - Kinetics of Growth.” *Transations of the Metallurgical Society of AIME* 242(7): 1437–48.

Aaronson, H I. 1977. “Discussion of ‘on the Growth Kinetics of Plate-Shaped Precipitates in Aluminum-Copper and Aluminum-Gold Alloys’ by YH Chen and RD Doherty.” *Scripta Metallurgica* 11(9): 731–32.

De Andrade, Vincent et al. 2016. “Nanoscale 3D Imaging at the Advanced Photon Source V. De Andrade, A. Deriy, M. J. Wojcik, D. Gürsoy, D. Shu, K. Fezzaa, F. De Carlo, SPIE Newsroom 2016, DOI 10.1117/2.1201604.006461.” *SPIE Newsroom*.

Ardell, A. J. 1985. “Precipitation Hardening.” *Metallurgical Transactions A* 16(12): 2131–65.

Ardell, A.J. 1972. “The Effect of Volume Fraction on Particle Coarsening: Theoretical Considerations.” *Acta Metallurgica* 20(1): 61–71.

Ashby, M. F. 1970. “The Deformation of Plastically Non-Homogeneous Materials.” *Philosophical Magazine* 21(170): 399–424.

Baldan, A. 2002. “Progress in Ostwald Ripening Theories and Their Applications to Nickel-Base Superalloys. Part I: Ostwald Ripening Theories.” *Journal of Materials Science* 37(11): 2171–2202.

Bale, Hrishikesh A. et al. 2012. “Real-Time Quantitative Imaging of Failure Events in Materials under Load at Temperatures above 1,600 °C.” *Nature Materials* 12(1): 40–46.

Blankenship, C.P., E. Hornbogen, and E.A. Starke. 1993. “Predicting Slip Behavior in Alloys Containing Shearable and Strong Particles.” *Materials Science and Engineering: A* 169(1–2): 33–41.

Bourgeois, Laure et al. 2011. “Structure and Energetics of the Coherent Interface between the Θ′ Precipitate Phase and Aluminium in Al–Cu.” *Acta Materialia* 59(18): 7043–50.

Boyd, J.D., and R.B. Nicholson. 1971. “The Coarsening Behaviour of Θ″ and Θ′ Precipitates in Two Al-Cu Alloys.” *Acta Metallurgica* 19(12): 1379–91.

Brown, L. M., and W. M. Stobbs. 1971. “The Work-Hardening of Copper-Silica.” *Philosophical Magazine* 23(185): 1201–33.

Buades, Antoni, Bartomeu Coll, and Jean-Michel J.-M. Morel. 2005. “A Non-Local Algorithm for Image Denoising.” *Computer Vision and Pattern Recognition, 2005. CVPR 2005. IEEE Computer Society Conference on* 2(0): 60–65 vol. 2.

Byer, Cynthia M., Bin Li, Buyang Cao, and K.T. Ramesh. 2010. “Microcompression of Single-Crystal Magnesium.” *Scripta Materialia* 62(8): 536–39.

Calabrese, C., and C. Laird. 1974. “Cyclic Stress—strain Response of Two-Phase Alloys Part II. Particles Not Penetrated by Dislocations.” *Materials Science and Engineering* 13(2): 159–74.

Canny, J. 1986. “A Computational Approach to Edge Detection.” *IEEE Trans. PAMI* 8(6): 679–98.

Cantor, Brian, Hazel Assender, and Patrick Grant. 2001. “Aerospace Materials.” *Series in Materials Science and Engineering*: 556.

De Carlo, Francesco et al. 2014. “Scientific Data Exchange: A Schema for HDF5-Based Storage of Raw and Analyzed Data.” *Journal of Synchrotron Radiation* 21(6): 1224–30.

Cernazanu-Glavan, Cosmin, and Stefan Holban. 2013. “Segmentation of Bone Structure in X-Ray Images Using Convolutional Neural Network.” *Advances in Electrical and Computer Engineering* 13(1): 87–94.

Chao, Weilun et al. 2005. “Soft X-Ray Microscopy at a Spatial Resolution Better than 15 Nm.” *Nature* 435(June): 1210–13.

Chen, B.A. et al. 2013. “Effect of Interfacial Solute Segregation on Ductile Fracture of Al–Cu–Sc Alloys.” *Acta Materialia* 61(5): 1676–90.

Chen, Y H, and R D Doherty. 1977. “On the Growth Kinetics of Plate-Shaped Precipitates in Aluminium-Copper and Aluminium-Gold Alloys.” *Scripta Metallurgica* 11(9): 725–29.

Da Costa Teixeira, J. et al. 2008. “On the Strengthening Response of Aluminum Alloys Containing Shear-Resistant Plate-Shaped Precipitates.” *Acta Materialia* 56(20): 6109–22.

Da Costa Teixeira, J., L. Bourgeois, C. W. Sinclair, and C. R. Hutchinson. 2009. “The Effect of Shear-Resistant, Plate-Shaped Precipitates on the Work Hardening of Al Alloys: Towards a Prediction of the Strength-Elongation Correlation.” *Acta Materialia* 57(20): 6075–89.

Davies, C.K.L., P. Nash, and R.N. Stevens. 1980. “The Effect of Volume Fraction of Precipitate on Ostwald Ripening.” *Acta Metallurgica* 28(2): 179–89.

Enomoto, Y., M. Tokuyama, and K. Kawasaki. 1986. “Finite Volume Fraction Effects on Ostwald Ripening.” *Acta Metallurgica* 34(11): 2119–28.

Di Fabrizio, E. et al. 1999. “High-Efficiency Multilevel Zone Plates for keV X-Rays.” *Nature* 401(6756): 895–98. http://dx.doi.org/10.1038/44791.

Fleischer, R.L. 1993. “Substitutional Solutes in AlRu—I. Effects of Solute on Moduli, Lattice Parameters and Vacancy Production.” *Acta Metallurgica et Materialia* 41(3): 863–69. Friedel, J. 1964. “Dislocations.” *Oxford* 70: 15–24.

Gorelick, Sergey et al. 2011. “High-Efficiency Fresnel Zone Plates for Hard X-Rays by 100 keV E-Beam Lithography and Electroplating.” *Journal of Synchrotron Radiation* 18(3): 442–46.

Greer, Julia R., Warren C. Oliver, and William D. Nix. 2005. “Size Dependence of Mechanical Properties of Gold at the Micron Scale in the Absence of Strain Gradients.” *Acta Materialia* 53(6): 1821–30.

Guinier, Andre. 1938. “Structure of Age-Hardened Aluminium-Copper Alloys.” *Nature* 142(3595): 569–70.

Gürsoy, D, F Carlo, X Xiao, and C Jacobsen. 2014. “TomoPy: A Framework for the Analysis of Synchrotron Tomographic Data.” *J. Synchrotron Radiat.* 21.

Gürsoy, Dogˇa, Francesco De Carlo, Xianghui Xiao, and Chris Jacobsen. 2014. “TomoPy: A Framework for the Analysis of Synchrotron Tomographic Data.” *Journal of synchrotron radiation* 21(Pt 5): 1188–93.

Hassan, Adel Mahmood, Omar M. Bataineh, and Khalil M. Abed. 2008. “The Effect of Time and Temperature on the Precipitation Behavior and Hardness of Al-4 wt%Cu Alloy Using Design of Experiments.” *Journal of Materials Processing Technology* 204: 343–49.

Hielscher, Ralf, and Gert Nolze. 2016. *IPF Coloring of Crystal Orientation Data*. Technische Universität Chemnitz, Fakultät für Mathematik.

Hillert, MATS. 1957. “Pressure Induced Diffusion and Deformation During Precipitation, Especially Graphitization.” *Jernkont. Ann* 141: 157–81.

Hornbogen, Erhard. 2001. “Hundred Years of Precipitation Hardening.” *Journal of Light Metals* 1(2): 127–32.

Hornbogen, Erhard, and Karl-Heinz Zum Gahr. 1975. “Distribution of Plastic Strain in Alloys Containing Small Particles.” *Metallography* 8(3): 181–202.

Hruby, Peter et al. 2014. “Fatigue Crack Growth in SiC Particle Reinforced Al Alloy Matrix Composites at High and Low R-Ratios by in Situ X-Ray Synchrotron Tomography.” *International Journal of Fatigue* 68: 136–43.

Hu, S. Y., M. I. Baskes, M. Stan, and L. Q. Chen. 2006. “Atomistic Calculations of Interfacial Energies, Nucleus Shape and Size of Θ′ Precipitates in Al-Cu Alloys.” *Acta Materialia* 54(18): 4699–4707.

Hu, Tao et al. 2015. “Stabilized Plasticity in Ultrahigh Strength, Submicron Al Crystals.” *Acta Materialia* 94: 46–58.

Huang, K., and R. E. Logé. 2016. “A Review of Dynamic Recrystallization Phenomena in Metallic Materials.” *Materials and Design* 111: 548–74.

Hurtado, Daniel E., and Michael Ortiz. 2012. “Surface Effects and the Size-Dependent Hardening and Strengthening of Nickel Micropillars.” *Journal of the Mechanics and Physics of Solids* 60(8): 1432–46.

Jacobsen, C, S Wirick, G Flynn, and C Zimba. 2000. “Soft X-Ray Spectroscopy from Image Sequences with Sub-100 Nm Spatial Resolution.” *Journal of microscopy* 197(July 1999): 173–84.

Kaira, C. Shashank et al. 2017. “Probing Novel Microstructural Evolution Mechanisms in Aluminum Alloys Using 4D Nanoscale Characterization.” *Advanced Materials*: 1703482.

Kaira, C. Shashank, Sudhanshu S. Singh, Antony Kirubanandham, and Nikhilesh Chawla. 2016. “Microscale Deformation Behavior of Bicrystal Boundaries in Pure Tin (Sn) Using Micropillar Compression.” *Acta Materialia* 120: 56–67.

Kaira, Chandrashekara S et al. 2016. “Nanoscale Three-Dimensional Microstructural Characterization of an Sn-Rich Solder Alloy Using High-Resolution Transmission X-Ray Microscopy (TXM).” *Microscopy and Microanalysis* 22(4): 808–13.

Kang, S.K, and C Laird. 1974. “Precipitation in Thin Foils of Al-4 WT.% Cu alloy—I. Morphology, Crystallography and Interfacial Structure of θ Precipitates.” *Acta Metallurgica* 22(12): 1481–95.

Kang, S.K, and C Laird. 1975. “Precipitation in Thin Foils of Al-4 Wt.% Cu alloy—II. Growth Kinetics of θ Precipitates.” *Acta Metallurgica* 23(1): 35–49.

Karlík, M et al. 2004. “HREM, FIM and Tomographic Atom Probe Investigation of Guinier–Preston Zones in an Al–1.54at% Cu Alloy.” *Ultramicroscopy* 98(2): 219–30.

Kelly, A, and R B Nicholson. 1963. “Progress in Materials Science.” *edited by Bruce Chalmers* 10.

Kiener, D. et al. 2007. “FIB Damage of Cu and Possible Consequences for Miniaturized Mechanical Tests.” *Materials Science and Engineering: A* 459(1–2): 262–72.

King, A. et al. 2010. “Non-Destructive Analysis of Micro Texture and Grain Boundary Character from X-Ray Diffraction Contrast Tomography.” *Nuclear Instruments and Methods in Physics Research Section B: Beam Interactions with Materials and Atoms* 268(3–4): 291–96.

Kunz, Allison, Siddhartha Pathak, and Julia R. Greer. 2011. “Size Effects in Al Nanopillars: Single Crystalline vs. Bicrystalline.” *Acta Materialia* 59(11): 4416–24.

Laird, C, and H.I Aaronson. 1966. “Mechanisms of Formation of [Theta] and Dissolution of [Theta]’ Precipitates in an Al-4% Cu Alloy.” *Acta Metallurgica* 14(2): 171–85.

Lawrence, S., C.L. Giles, Ah Chung Tsoi, and A.D. Back. 1997. “Face Recognition: A Convolutional Neural-Network Approach.” *IEEE Transactions on Neural Networks* 8(1): 98–113.

LeCun, Yann et al. 2015. “Deep Learning.” *Nature* 521(7553): 436–44.

LeCun, Yann, Léon Bottou, Yoshua Bengio, and Patrick Haffner. 1998. “Gradient-Based Learning Applied to Document Recognition.” *Proceedings of the IEEE* 86(11): 2278–2323.

Lee, Seok-Woo, and William D. Nix. 2012. “Size Dependence of the Yield Strength of Fcc and Bcc Metallic Micropillars with Diameters of a Few Micrometers.”

Li, Shi Hao et al. 2017. “Small-Volume Aluminum Alloys with Native Oxide Shell Deliver Unprecedented Strength and Toughness.” *Acta Materialia* 126: 202–9.

Lifshitz, I.M., and V.V. Slyozov. 1961. “The Kinetics of Precipitation from Supersaturated Solid Solutions.” *Journal of Physics and Chemistry of Solids* 19(1–2): 35–50.

Limodin, N. et al. 2009. “In Situ and Real-Time 3-D Microtomography Investigation of Dendritic Solidification in an Al–10wt.% Cu Alloy.” *Acta Materialia* 57(7): 2300–2310.

Liu, Grace. 2011. ProQuest Dissertations and Theses "Time-Resolved and Three-Dimensional Study of Dislocation-Particle Interactions in Aluminum and Copper Alloys." University of Illinois at Urbana-Champaign.

Lumley, R. N., I. J. Polmear, and A. J Morton. 2003. "Interrupted Aging and Secondary Precipitation in Aluminium Alloys." *Materials Science and Technology* 19(11): 1483–90.

Ma, P.P. et al. 2016. "Mechanical Properties Enhanced by Deformation-Modified Precipitation of Θ′-Phase Approximants in an Al-Cu Alloy." *Materials Science and Engineering: A* 676: 138–45.

Maire, E., and P. J. Withers. 2013. "Quantitative X-Ray Tomography." *International Materials Reviews* 59(1): 1–43.

Mantina, M. et al. 2009. "First Principles Impurity Diffusion Coefficients." *Acta Materialia* 57(14): 4102–8.

Merle, P., and F. Fouquet. 1981. "Coarsening of Θ′ Plates in Al-Cu alloys—I. Experimental Determination of Mechanisms." *Acta Metallurgica* 29(12): 1919–27.

Merle, P., and J. Merlin. 1981. "Coarsening of Θ′ Plates in Al-Cu alloys—II. Influence of Ledge Mechanism." *Acta Metallurgica* 29(12): 1929–38.

Midgley, Paul a, and Rafal E Dunin-Borkowski. 2009. "Electron Tomography and Holography in Materials Science." *Nature materials* 8(4): 271–80.

Miller, M K, and E a Kenik. 2004. "Atom Probe Tomography: A Technique for Nanoscale Characterization." *Microscopy and microanalysis : the official journal of Microscopy Society of America, Microbeam Analysis Society, Microscopical Society of Canada* 10(3): 336–41.

Mortensen, Eric N., and William A. Barrett. 1998. "Interactive Segmentation with Intelligent Scissors." *Graphical Models and Image Processing* 60(5): 349–84.

Muddle, B C, and J F Nie. 2006. "Nucleation-Mediated Structural Refinement and Aluminium Alloy Design." *Materials Science Forum* 519/521: 191–96.

Nie, J. F., and B. C. Muddle. 1998. "Microstructural Design of High-Strength Aluminum Alloys." *Journal of Phase Equilibria* 19(6): 543–51.

Nie, J. F., and B. C. Muddle. 2001. "On the Form of the Age-Hardening Response in High Strength Aluminium Alloys." *Materials Science and Engineering A* 319–321: 448–51.

Nie, J.F., and B.C. Muddle. 2008. “Strengthening of an Al–Cu–Sn Alloy by Deformation-Resistant Precipitate Plates.” *Acta Materialia* 56(14): 3490–3501.

Nie, Jian Feng, Barry C. Muddle, and Ian J. Polmear. 1996. “The Effect of Precipitate Shape and Orientation on Dispersion Strengthening in High Strength Aluminium Alloys.” *Materials Science Forum* 217–222: 1257–62.

Nix, William D., Julia R. Greer, Gang Feng, and Erica T. Lilleodden. 2007. “Deformation at the Nanometer and Micrometer Length Scales: Effects of Strain Gradients and Dislocation Starvation.” *Thin Solid Films* 515(6): 3152–57.

Orowan, E. 1948. “Discussion in The Symposium on Internal Stresses in Metals and Alloys, Inst.” *Metals, London* 451.

Park, B. K., V. Greenhut, G. Luetjering, and S. Weissman. 1970. “Dependence of Fatigue Life and Flow Stress on the Microstructure of Precipitation-Hardened Al-Cu Alloys.”

Pattnaik, A., and A. Lawley. 1971. “Deformation and Fracture in Al-CuAl2 Eutectic Composites.” *Metallurgical Transactions* 2(6): 1529–36.

Pelt, D M et al. 2016. “Integration of TomoPy and the ASTRA Toolbox for Advanced Processing and Reconstruction of Tomographic Synchrotron Data.” *J. Synchrotron Radiat.* 23.

Pelt, Daniel M., and Kees Joost Batenburg. 2015. “Accurately Approximating Algebraic Tomographic Reconstruction by Filtered Backprojection.” In *International Meeting on Fully Three-Dimensional Image Reconstruction in Radiology and Nuclear Medicine.*, 158–61.

Preston, G D. 1940. “Age-Hardening of Copper-Aluminium Alloys.” *Proceedings of the Physical Society* 52(1): 77–79.

Requena, G. et al. 2009. “Sub-Micrometer Synchrotron Tomography of Multiphase Metals Using Kirkpatrick-Baez Optics.” *Scripta Materialia* 61: 760–63.

Ringer, S.P., and K. Hono. 2000. “Microstructural Evolution and Age Hardening in Aluminium Alloys.” *Materials Characterization* 44(1–2): 101–31.

Russell, Kathryn G, and M.F Ashby. 1970. “Slip in Aluminum Crystals Containing Strong, Plate-like Particles.” *Acta Metallurgica* 18(8): 891–901.

Sakdinawat, Anne, and David Attwood. 2010. “Nanoscale X-Ray Imaging.” *Nature Photonics* 4(December): 840–48.

Sankaran, R, and C Laird. 1974. “Kinetics of Growth of Platelike Precipitates.” *Acta Metallurgica* 22(8): 957–69.

Schneider, A. S. et al. 2009. “Correlation between Critical Temperature and Strength of Small-Scale Bcc Pillars.” *Physical Review Letters* 103(10): 105501.

Schneider, Caroline A, Wayne S Rasband, and Kevin W Eliceiri. 2012. “NIH Image to ImageJ: 25 Years of Image Analysis.” *Nature Methods* 9(7): 671–75.

Schroer, Christian G. 2006. “Focusing Hard X Rays to Nanometer Dimensions Using Fresnel Zone Plates.” *Physical Review B - Condensed Matter and Materials Physics* 74(3): 1–4.

Shan, Z W et al. 2004. “Grain Boundary Mediated Plasticity in Nanocrystalline Nickel.” *Science (New York, N.Y.)* 305(July): 654–57.

Shim, S. et al. 2009. “Effects of Focused Ion Beam Milling on the Compressive Behavior of Directionally Solidified Micropillars and the Nanoindentation Response of an Electropolished Surface.” *Acta Materialia* 57(2): 503–10.

Singh, Sudhanshu S et al. 2014. “In Situ Experimental Techniques to Study the Mechanical Behavior of Materials Using X-Ray Synchrotron Tomography.” *Integrating Materials and Manufacturing Innovation* 3(1): 9.

Thomas, G, and M J Whelan. 1961. “Observations of Precipitation in Thin Foils of Aluminium+ 4% Copper Alloy.” *Philosophical Magazine* 6(69): 1103–14.

Uchic, Michael D., Paul A. Shade, and Dennis M. Dimiduk. 2009. “Plasticity of Micrometer-Scale Single Crystals in Compression.” *Annual Review of Materials Research* 39(1): 361–86.

Vaithyanathan, V., C. Wolverton, and L. Q. Chen. 2004. “Multiscale Modeling of Θ′ Precipitation in Al-Cu Binary Alloys.” *Acta Materialia* 52(10): 2973–87.

Vila-comamala, Joan et al. 2011. “Ultra-High Resolution Zone-Doubled Diffractive X-Ray Optics for the Multi-keV Regime.” 19(1): 80–84.

Vogt, Ulrich et al. 2006. “Condenser for Koehler-like Illumination in Transmission X-Ray Microscopes at Undulator Sources.” *Optics letters* 31(10): 1465–67.

Voorhees, P.W., and M.E. Glicksman. 1984. “Solution to the Multi-Particle Diffusion Problem with Applications to Ostwald ripening—II. Computer Simulations.” *Acta Metallurgica* 32(11): 2013–30.

Wagner, Carl. 1961. “Theorie Der Alterung von Niederschlägen Durch Umlösen (Ostwald-Reifung).” *Zeitschrift für Elektrochemie, Berichte der Bunsengesellschaft für physikalische Chemie* 65(7-8): 581–91.

Wang, Jiajun, Christopher Eng, Yu-chen Karen Chen-Wiegart, and Jun Wang. 2015. “Probing Three-Dimensional Sodiation–desodiation Equilibrium in Sodium-Ion Batteries by in Situ Hard X-Ray Nanotomography.” *Nature Communications* 6(May): 7496.

Weatherly, G. C. 1970. “Antiphase Domain Boundaries in Ordered Θ’ (CuAl2) Precipitates in an Al-4% Cu Alloy.” *Acta Metallurgica* 18(1): 15–22.

Weinberger, Christopher R, and Wei Cai. 2008. “Surface-Controlled Dislocation Multiplication in Metal Micropillars.” *Proceedings of the National Academy of Sciences of the United States of America* 105(38): 14304–7.

Xiao, Y. et al. 2017. “Investigation of the Deformation Behavior of Aluminum Micropillars Produced by Focused Ion Beam Machining Using Ga and Xe Ions.” *Scripta Materialia* 127: 191–94.

Yang, X, F De Carlo, C Phatak, and D Gürsoy. 2017. “A Convolutional Neural Network Approach to Calibrating the Rotation Axis for X-Ray Computed Tomography.” *Journal of Synchrotron Radiation* 24(2): 469–75.

Yazzie, K.E. et al. 2012. “Multiscale Microstructural Characterization of Sn-Rich Alloys by Three Dimensional (3D) X-Ray Synchrotron Tomography and Focused Ion Beam (FIB) Tomography.” *Materials Characterization* 70: 33–41.

Yoshida, H., D. J. H. Cockayne, and M. J. Whelan. 2006. “A Study of Guinier-Preston Zones in Aluminium-Copper Alloys Using the Weak-Beam Technique of Electron Microscopy.”

Zener, Clarence. 1946. “Kinetics of the Decomposition of Austenite.” *Trans. Aime* 167(550): e591.

Zhu, A. W., and E. A. Starke. 1999. “Strengthening Effect of Unshearable Particles of Finite Size: A Computer Experimental Study.” *Acta Materialia* 47(11): 3263–69.

Zhu, A.W., A. Csontos, and E.A. Starke. 1999. “Computer Experiment on Superposition of Strengthening Effects of Different Particles.” *Acta Materialia* 47(6): 1713–21.